Systèmes électromécaniques nanométriques a base de nano-fils de silicium et nanotubes de carbone

Ervin Mile

▶ To cite this version:

HAL Id: pastel-00551920

https://pastel.hal.science/pastel-00551920

Submitted on 4 Jan 2011

THÈSE DE DOCTORAT DE L'ÉCOLE POLYTECHNIQUE

Spécialité

Physique

Présentée par

Ervin Mile

Pour obtenir le grade de DOCTEUR DE L'ÉCOLE POLYTECHNIQUE

Sujet de la thèse

Systèmes électromécaniques nanométriques à base de nanofils de silicium et nanotubes de carbone

Rapporteur :	Prof. Joël Chevrier,	Universite' Joseph Fourier Grenoble
	Prof. Stephen Purcell,	Universite' Lyon 1
Examinateur :	Prof. Moustapha Hafez,	CEA/Laboratoire Interfaces Sensorielles
	Dr. Alistair Rowe,	LPMC - Ecole Polytechnique
Directeur de these :	Dr. Robert Baptist,	Directeur de Recherche, CEA-LETI
Co-encadrant :	Dr. Laurent Duraffourg,	CEA-LETI/LCMS

Laboratoire Composants Microsystèmes - CEA/Leti - Grenoble

Laboratoire d'Électronique Moléculaire - CEA/LEM - Saclay

Nanowire and carbon nanotube based NEMS resonators

Speciality

Physics

Presented by

Ervin Mile

Thesis submitted to Ecole Polytechnique
for the degree of Doctor of Philosophy

Ecole Polytechnique
Palaiseau, France

2010
(Defended June 3, 2010)

Dedicated to my parents

Acknowledgements

I would like to thank all the people who have given their contribution in different ways helping me to accomplish this work successfully. This research project would not have been possible without their precious continuous support.

Chemtronics : "Marie Curie Early Stage Training". The opportunity for you to study for your PhD in France (Grenoble and Paris). This poster was hanged one morning in front of the Nanomaterials and Electronics Laboratory (NMELAB) at MIT. I became curious and got closer to it, honestly the Grenoble picture with the "Eggs" attracted my attention more than the Eiffel tower. I had been living 6 months under the Bastille watching these spheres going up and down over my head everyday. When I knew my candidature was accepted, I felt extraordinary happy. A great "Thank You" for choosing me.

I want to thank the "Marie Curie" program for financing and making possible the realization of the Chemtronics project. I would like to thank the people responsable for the Chemtronics project, in particular Dr. Robert Baptist, Dr. Isabelle Schuster and Nathalie Colombel which have been present for all the PhD students from the very first moment in CEA. You have done a great job. Thank you Dr. Robert Baptist for accepting to be my thesis director, for the availability and your precious advises. I want to express you my full admiration.

I'm very thankful to Prof. Jean-Philippe Bourgoin and Dr. Marcelo F. Goffman for proposing the work in the CNT-NEMS domain and welcoming me in their group in Saclay (CEA/LEM - Laboratoire d'Electronique Moléculaire). I thank all my colleagues PhD students and the staff for transmitting part of their experience with advises and trainings.

I want to thank Dr. Miguel Monteverde a very special person which has been always close to me during these years. I want to thank you Miguel for your great

support, priceless help and for being always available.

I thank Dr. Arianna Filoramo, Dr. Vincent Derycke and Pascal Lavie for their training and help with equipments. I would like to thank Dr. Chia-ling Chung, Dr. Gael Robert, Dr. Khoa Nguyen, Dr. Gregory Schmidt, Dr. Sébastien Lyonnais, Dr. Nicolas Izard, Dr. Nicolas Chimot, Dr. Sampo Tuukkanen, Dr. Pascale Chenevier and Dr. Stéphane Campidelli who made it an enjoyable stay for me in Saclay.

The main part of this thesis was performed at CEA/LETI - Laboratoire Composants Microsystèmes (LCMS) in Grenoble. A particular thank to Philippe Andreucci and Dr. Laurent Duraffourg for giving me the opportunity to work in the "Nanosystems VLSI" project.

Thank you Laurent for accepting to be my thesis director. I really appreciated your discussions and invaluable assistance in the field. If I'm able to write this acknowledgment page today, I owe it mostly to you who took me by the hand and guided to the finish. I want to express my sincerest gratitude for your help and patience. I consider my self very lucky to have worked together. I highly recommend you to all future PhD students and post docs who would like to continue their research in the MEMS or NEMS domain.

I wish to thank my good colleague and friend Dr. Guillaume Jourdan for the great assistance with the measurements, discussions, suggestions, the help with the writing ; your hand is also everywhere. Many thanks are addressed also to Dr. Igor Bargatin for sharing his experience in the domain and helping to achieve remarkable results. It would be almost impossible performing my experiments without Dr. Carine Marcoux the expert in nanofabrication which continuously provided the samples for my research, thank you Carine. Thank you Sébastien Labarthe for allowing me to make measurements on your samples.

My immense appreciations go to Dr. Najib Kacem a good friend and collegue. Thank you Najib for helping with mechanical analysis and simulations. Thank you for the time spent inside and outside the CEA. Many thanks to Henri Blanc for his technical help and interesting discussions. I will miss the time spent with you and Najib and the lunch chat at the restaurant. A huge gratitude to Dr. Eric Colinet, Dr. Chady Kharrat for making possible the PLL measurements.

Thanks to Dr. Philippe Robert and all the LCMS team for the warm hospitality. I enjoyed the time spent with you on the lab and in my office. I want to thank Dr. Bruno

Table des matières

Table des figures

Chapitre 1

Introduction

Nano-electro-mechanical systems (NEMS) are nano-scale devices composed by mechanical moving parts and the electronic circuitry. They integrate electrical and mechanical functionality on the nanoscale. Their purpose is to sense a specific physical quantity and convert it into a measurable electrical signal. The technological progress in the design and fabrication of nano-electromechanical systems (NEMS) has enabled the device sizes reduction from micro to nanometers. NEMS come as a result of micro-electro-mechanical systems (MEMS) size reduction, following the trend of miniaturization and very large scale integration (VLSI). NEMS are commonly distinguished from MEMS by their smaller size, as devices with mechanical structures having at least two dimensions on the nano-scale. The main building blocks constituting the mechanical moving parts of a NEMS are silicon nano-beams, nano-cantilevers, carbon nanotubes and nanowires (figure 1.1).

These structures are in continuous interaction with the surrounding environment and constitute the sensing unit. A change in the environment will cause a change in their mechanical and electrical properties (motion amplitude, resonance frequency, quality factor etc). This variation is converted by appropriate transducers into a processable electrical signal. The purpose of the electronic circuitry is related to the actuation and detection of motion of the mechanical structures. These devices allow to collect environmental information such as changes of temperature, pressure, mass and forces. NEMS are mainly fabricated using conventional microelectronics processes combined with micro-machining technology or bottom-up techniques. They can be processed in parallel and in large quantities making them cost-effective for many
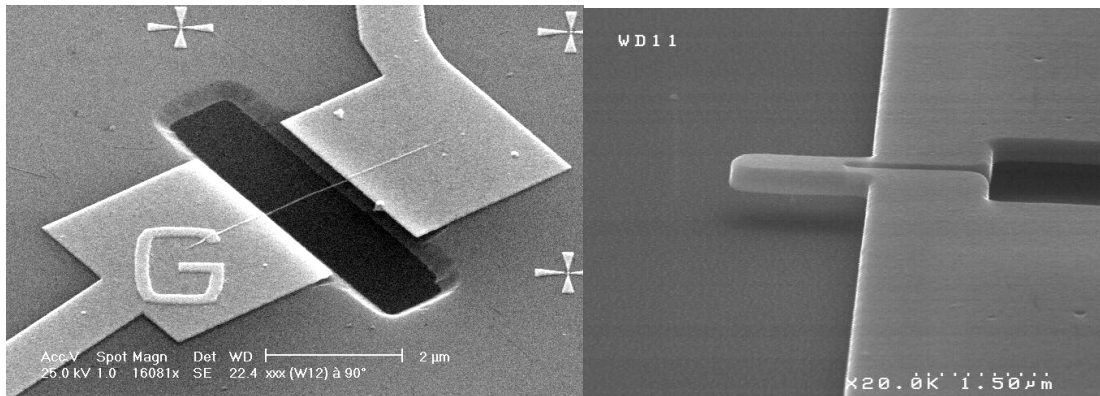
(a) Doubly clamped carbon nanotube NEMS re-(b) Piezoresistive nanocantilever beam fabri-
sonator fabricated at CEA-LEM   cated at CEA-LETI

Fig. 1.1: Typical nano electromechanical devices

uses. NEMS are expected to impact many areas of technology. Their small masses,
high mechanical resonance frequencies(10Mhz-1Ghz), large quality factors (10^3-10^4),
increased sensitivity and low power consumption allows for better performing sensors.
NEMS offer a wide range of potential applications. They are envisaged to be used
in ultra-small mass [1] and force sensing applications for biological[2] or chemical
sensors[3]. Higher frequencies NEMS scanning probes enable higher AFM operation
frequencies and faster image processing [3, 4]. Carbon nanotubes with nanometer
diameters used as AFM tips offer an increased image resolution and the list goes on.
Nevertheless the great advantages offered by NEMS, in this domain it doesn't exist
yet a well established technique for detecting efficiently the electrical signal generated
by the mechanical displacement of these nanostructures.

This explains why laboratories and industrial centers still continue their research
exploring different detection techniques. Motion transduction at the micrometer scale
has been successfully realized using optical[5], magnetic[6], electrostatic[7], piezoelectric[8]
and piezoresistive[9] transducers through electronic coupling.

However some of these detection techniques such as optic, capacitive and piezoelec-
tric become inefficient at the submicron scales. While others such as magnetomotive
detection remain difficult to integrate, in spite of the efforts and advances made in
this direction [10].

The most important technological challenge in nano-electromechanical systems
operation is the efficient detection of sub-nanometer displacements at high frequen-

cies. The transduction efficiency will determine the devices performances and will set its limits. The objective of this thesis is focused on solving this major problem. The research is specially focused on developing a nanowire-based detection technique for transducing the nano-mechanical displacement into an electrical signal. The research has been organized around three principal axes :

The first part aims to evaluate and compare theoretically different actuation/detection schemes for nanowire-based NEMS in order to choose the one which presents the highest transduction gain and signal to background ratio (SBR). This approach is crucial since the results of this study will decide the continuation of our research and the techniques to be implemented. This work is the starting basis before moving to development.

The second part is dedicated to the fabrication of NEMS devices and to the implementation of an actuation/detection scheme for mechanical motion detection at frequencies up to 100MHz. Completing successfully this step will allow us to continue with the experimental evaluation of the transduction technique efficiency.

The third part is centred on the experimental characterization of the transduction efficiency. The central parameters that are going to be explored are the transduction gain, the signal to background ratio, the signal to noise ratio (SNR), the resonance frequency of the devices, the quality factor, the ultimate displacement and mass resolution. The experimental results are of high importance since they are used to confirm the expectations and to validate the theoretical analysis. Finally the results have been compared with the state of the art results, in order to highlight the advances and contribution in the field.

Chapitre 2

Theoretical evaluation of actuation/detection schemes for nano electromechanical systems

One of the most important technological challenges in the nano-electro-mechanical system (NEMS) operation is the detection of nanometer displacement at high frequencies and room temperature. In this chapter we will analyze and evaluate theoretically different methods for actuation and detection of motion in nano-electromechanical systems in order to choose the most efficient in terms of signal to background ratio (SBR). The SBR is a figure of merit of a detection scheme characterizing the contrast in magnitude between the effective signal to be measured and the surrounding background. This study will start with an introduction to the most common NEMS structures such as doubly clamped nano-beams, nano-tubes and nano-cantilevers. The discussion will proceed with the operating principle of these devices and their mechanical behavior (resonance frequency, amplitude and quality factor). The work will follow by defining the main criteria necessary for the choice of an efficient electromechanical transducer (actuator/detector). Low power consumption, a broad operation bandwidth and sensitive on chip electronic read-out of motion are crucial constraint parameters that will be considered for the integration and application of portable nanoelectromechanical devices. We will focus on comparing the signal to background ratio of various electronic measurement configurations such as the reflection/transmission of the electric signal and bridge techniques. Finally in accordance with the performed

analysis we will propose the most promising actuation/detection method, and the highest SBR measurement technique for portable NEMS motion detection.

2.1 Mechanical behavior of a typical NEMS resonator

We mentioned previously that the mechanical part constitutes the sensing unit. How does this unit sense the environmental changes ? How does it operate, what is its functioning principle ? NEMS are usually oscillating doubly clamped beams or cantilevers operated at their modal frequencies. The mechanical moving parts interact and exchange energy continuously with physical and chemical stimuli. This interactions can alter the mechanical and electrical properties of the mechanical structures. The main parameters characterizing the mechanical behavior of a NEMS resonator are the resonance frequency, the amplitude of displacement, the mass and the quality factor. By monitoring eventual changes of these parameters one can measure specific agents and sense the environment. Sensing with NEMS is mainly based on frequency shift analysis related to a specific event. If an additional mass ΔM is deposited on a vibrating beam it will cause a resonance frequency shift $\Delta \omega$ proportional to it. We can design thus a mass sensor based on frequency shift analysis[11, 12]. How can one measure the resonance frequency of a mechanical resonator ? The resonance frequency measurement is mainly based on the detection of mechanical displacement of beams as a function of the actuation frequency. The mechanical response of a beam resonator has a Lorentzian shape with maximum displacement amplitude corresponding to its resonance frequency. The displacement is transduced into an electrical signal through appropriate transducers. We are interested in evaluating the mechanical displacement because the transduced electrical signal is dependent and proportional to it. The beam displacement is going to be simplified to a lumped mass/spring damping model which is useful for making electromechanical analogies and describin its behaviour with an RLC circuit. In this part we are going to analyze the dynamical mechanical behavior of the two most common NEMS geometries, a doubly clamped beam (rectangular or circular cross sectional area) and a cantilever. The resonance frequency, beam stiffness, effective mass and vibrating amplitude and their scaling with dimensions are
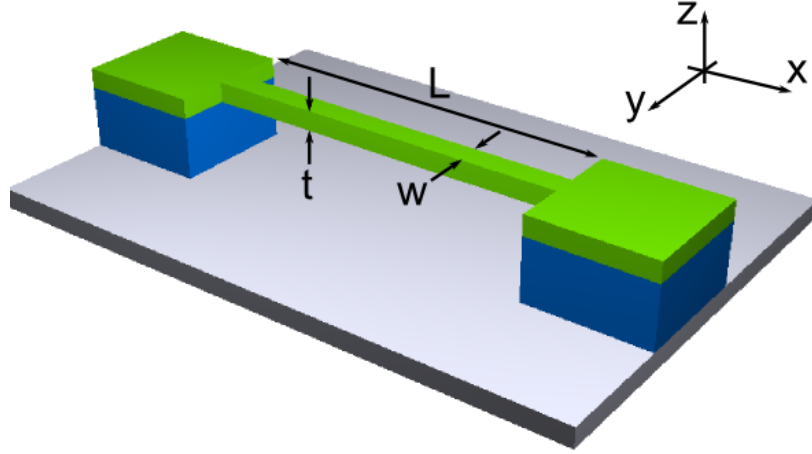
Fig. 2.1: Doubly clamped beam with length L, thickness t and width w

evaluated. Our analysis is focused in the linear regime since mass sensing through frequency shift with NEMS resonators is performed in this range. The motion of a beam in the limit of small displacement is governed and described by the Euler-Bernoulli beam theory, which applies to beams with aspect ratios $L/t >> 1$ [13]. In the case of a resonator a harmonic driving force $F(x,t) = g(x) \cdot f(t) = g(x) \cdot F_0 \cdot e^{-i\omega_c t}$ is applied to the beam, where g(x) is the position-depended force per unit length. The force is considered to be uniform across the beam cross section and directed along y. The carrier frequency ω_c is close to the resonance one ω_0. The equation of motion of a damped driven harmonic oscillator is given by :

$$\text{EI}\frac{\partial^4 y(x,t)}{\partial x^4} + \rho\text{S}\frac{\partial^2 y(x,t)}{\partial t^2} + b\frac{\partial y(x,t)}{\partial t} = g(x)f(t) \tag{2.1}$$

Where E is the Young's modulus, I the moment of inertia, b the damping coefficient, S the cross-sectional area, ρ the mass density and $y(x,t)$ is the displacement of the neutral axis at a point x along the beam. The partial differential equation (PDE) is solved using the Galerkin procedure [14]. The displacement $y(x,t)$ can be separated into two parts, one depends on position $\phi_n(x)$ and another on time $y_n(t)$.

$$y(x,t) = \sum_{\infty}^{n=1} y_n(t) \cdot \phi_n(x) \tag{2.2}$$

where $\phi_n(x)$ are eigensolutions of equation (2.1) and are obtained by solving the following differential equation.

$$\frac{\partial^4 \phi_n(x)}{\partial x^4} = \lambda_n^4 \cdot \phi_n(x) \tag{2.3}$$

The general solution to equation (2.3) is a linear combination of trigonometric equations, [15] (Volterra, p.312) and has the following form :

$$\phi_n(x) = C_1 \cos(\lambda_n x) + C_2 \cosh(\lambda_n x) + C_3 \sin(\lambda_n x) + C_4 \sinh(\lambda_n x) \tag{2.4}$$

The corresponding frequency equation for the flexural vibration of a beam of length L is given by :

$$f_n = \frac{(\lambda_n L)^2}{2\pi L^2} \sqrt{\frac{\text{EI}}{\rho \text{S}}} \tag{2.5}$$

where n is the mode number, $\lambda_n L$ the mode value for the n-th mode and f_n is the n-th free mode frequency in $[Hz]$. The eigen-frequencies depend on the boundary conditions and on the beam length. The most common geometries in NEMS devices are doubly clamped beams and cantilevers.

For a clamped-clamped beam of length L the boundary conditions are :
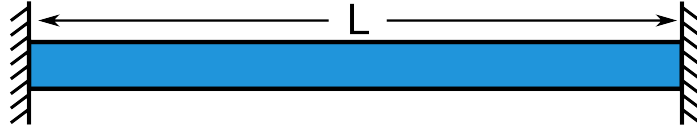
Fig. 2.2: fixed-fixed beam model

$\phi_n(0) = 0$, $\phi_n'(0) = 0$, $\phi_n(L) = 0$ and $\phi_n'(L) = 0$. The first eigen-values shown in (table 2.2) result,

n	1	2	3	4
$\lambda_n L$	$\lambda_1 L = 4.73$	$\lambda_2 L = 7.853$	$\lambda_3 L = 10.995$	$\lambda_4 L = 14.137$

Tab. 2.1: eigenvalues for a doubly clamped beam

For a cantilever beam of length L the boundary conditions are :
$\phi_n(0) = 0$, $\phi_n'(0) = 0$, $\phi_n''(L) = 0$ and $\phi_n'''(L) = 0$. The first eigen values shown in (table 2.2) result,
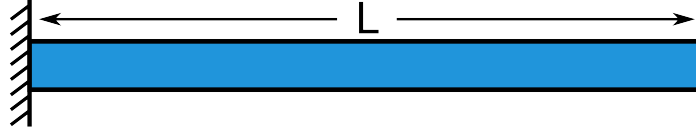
Fig. 2.3: fixed-free beam model

n	1	2	3	4
$\lambda_n L$	$\lambda_1 L = 1.875$	$\lambda_2 L = 4.694$	$\lambda_3 L = 7.854$	$\lambda_3 L = 10.995$

Tab. 2.2: eigenvalues for a clamped free beam

Since ϕ_n is a base it should satisfy the normalization condition. We have considered the base ϕ_n to be dimensionless.

$$\frac{1}{L} \int_0^1 \phi_n(x)\phi_n(x) = 1 \tag{2.6}$$

The first mode shape for a doubly clamped beam and a cantilever result :
a) Clamped-clamped beam

$$\phi_1(x) = \cos[(\lambda_1 L)\frac{x}{L}] - \cosh[(\lambda_1 L)\frac{x}{L}] - 0.982 \sin[(\lambda_1 L)\frac{x}{L}] + 0.982 \sinh[(\lambda_1 L)\frac{x}{L}] \tag{2.7}$$

b) Cantilever beam

$$\phi_1(x) = \cos[(\lambda_1 L)\frac{x}{L}] - \cosh[(\lambda_1 L)\frac{x}{L}] - 0.734 \sin[(\lambda_1 L)\frac{x}{L}] + 0.734 \sinh[(\lambda_1 L)\frac{x}{L}] \tag{2.8}$$

The maximum mode coefficient corresponding to the maximum displacement is achieved at the center of the beam for a clamped-clamped structure and at its end for a cantilever (figure 2.4). In order to find the full solution for y(x,t), we first put equation (2.2) into equation (2.1). By multiplying each side of the equation by ϕ_1 and integrating along the beam we obtain :

$$y''(t) + \frac{b}{\rho S}y'(t) + \frac{EI}{\rho S}\lambda_1^4 y(t) = \frac{f(t)}{\rho SL} \int_0^1 g(x)\phi_1(x)dx \tag{2.9}$$

This equation corresponds to a mass spring damped harmonic oscillator driven by a force $f(t)$.

$$y''(t) + \frac{\omega_0}{Q}y'(t) + \omega_0^2 y(t) = \frac{\eta_1 f(t)}{\rho SL} \tag{2.10}$$
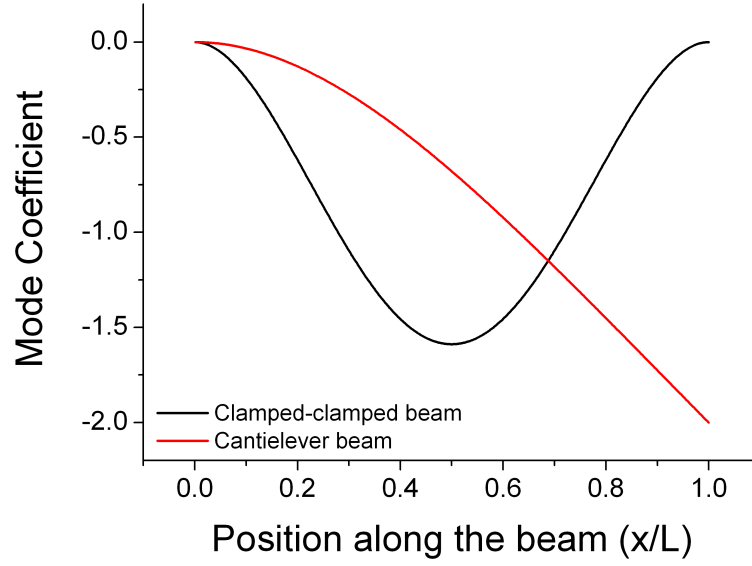
Fig. 2.4: Shape of the first mode for a doubly clamped beam and a cantilever

Where Q is the quality factor, the resonance frequency $\omega_0^2 = \frac{EI}{\rho S}\lambda_1^4$ and $\eta_1 = \int_0^1 g(x)\phi_1(x)dx$ is a constant depending on the force repartition along the beam. For a spatially uniform force distribution we have $g(x) = 1$. In the case of the doubly clamped beam $\eta_1 = 0.83$ and for a cantilever $\eta_1 = 0.783$. When the resonator is driven close to the first mode resonance, the deflection $y(x, t)$ reduces to $y(x, t) = y_1(t)\phi_1(x)$, the other modes being mechanically filtered. In the case of a periodic force $f(t) = F_0 \cdot cos(\omega t)$ the transfer function of the beam can be determined from the Fourier transform of equation (2.10) that results :

$$y_1(\omega) = \frac{\eta_1}{\rho SL \left(\omega_0^2 - \omega^2 + \mathrm{j}\omega\omega_0/Q\right)}F(\omega) \tag{2.11}$$

where $y(\omega)$ and $f(\omega)$ are the Fourier transform of $y(t)$ and $f(t)$. The time dependent motion equation is given by :

$$y_1(\omega, t) = A_1(\omega)\cos(\omega t - \varphi) = \frac{\eta_1 F_0}{\rho SL}\frac{1}{\sqrt{(\omega_0^2 - \omega^2)^2 + (\omega\omega_0/Q)^2}}\cos(\omega t - \varphi) \tag{2.12}$$

Where $\varphi = \mathrm{arctg}\left(\frac{\omega\omega_0/Q}{\omega_0^2 - \omega^2}\right)$ is the phase lag between the displacement $y(t)$ and the force $f(t)$. At resonance $\omega \approx \omega_0$ the phase lag is equal to $\pi/2$. The displacement at

any position x along the beam as a function of frequency ω and time t is given by :

$$y_n(x, \omega, t) = y_n(\omega, t) \cdot \phi_n(\frac{x}{L}) \tag{2.13}$$

2.1.1 The damped harmonic oscillator

The resonator dynamic behavior can then be described within a one dimension equivalent model at $(x = L/2)$ for the clamped-clamped beam and $(x = L)$ for the cantilever (figure 2.5).
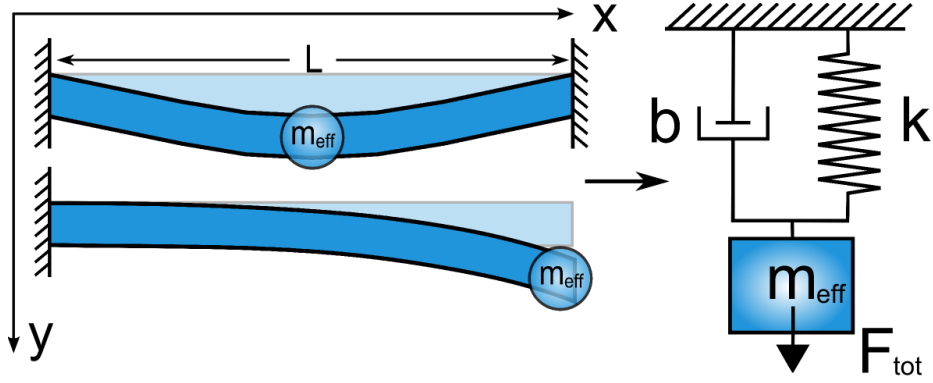
Fig. 2.5: One dimensional driven damped harmonic oscillator. Equivalent lumped mass/spring/damping, m_{eff} is the effective mass, k the spring constant, b the damping and F_{tot} the total force.

In the case of a doubly clamped beam the lumped spring/mass/damping model describes the displacement of the center of the beam, while for a cantilever it describes the displacement at the end of the beam.

$$y_1(\omega, \frac{L}{2}) = \frac{F_{tot}}{m_{eff}} \frac{1}{\sqrt{(\omega_0^2 - \omega^2)^2 + (\omega\omega_0/Q)^2}} \tag{2.14}$$

The effective mass of the equivalent resonator is $m_{eff} = \rho SL/1.58\eta_1 = 0.762\rho SL$ for a clamped-clamped beam and $m_{eff} = 0.638\rho SL$ for a cantilever beam. The total force is $F_{tot} = F_0 \cdot L$.

The *amplitude* is defined as the maximum displacement of a vibrating body from its equilibrium position. The condition for maximum amplitude for a sinusoidally driven damped resonator is given by :

$$\omega = \omega_0 \sqrt{1 - \frac{1}{2Q^2}} \tag{2.15}$$

The maximum amplitude obtained for this frequency results :

$$A_{\max} = \frac{2}{m\omega_0^2\sqrt{(2Q)^2 - 1}} \approx \frac{F_0 Q}{m_{eff}\omega_0^2} \qquad (2.16)$$

A damped resonator loses energy during each oscillation. To describe the rate of energy loss in a damped resonator, we define the quality factor Q that is equal to :

$$Q = \frac{\text{Energy stored in the resonator}}{\text{Energy lost per cycle}} = \frac{\omega_0}{\gamma} \qquad (2.17)$$

Where $\gamma = b/m$ is the damping coefficient divided by the resonator mass. For quality factors $Q >> 1$ we have $A_{\max} \approx \frac{f}{m\omega_0^2}Q$ obtained for $\omega \approx \omega_0$.

Resonators having higher Q factors oscillate with greater amplitudes but have a smaller range of frequencies for which they resonate. The range of frequencies for which the oscillator resonates is called the *bandwidth*. The bandwidth is inversely proportional to Q and is defined as :

$$\Delta f = \frac{f}{Q} \qquad (2.18)$$

The bandwidth represents the distance between the two points in the frequency domain where the signal is $1/\sqrt{2}$ of the maximum signal amplitude. Higher is the quality factor Q, narrower is the bandwidth and more stable the oscillator, since the oscillator will stay closer to its natural resonance frequency.

2.1.2 Circular cross-section beams

Most of the beams at the nanoscale such as carbon nanotubes or nanowires have circular cross sectional area. What will be their resonance frequency ? In the case of a carbon nanotube or a structure having a tubular geometry with outside diameter D_{out} and inside diameter D_{in}, the moment of inertia I and the cross-sectional area A result :

$$I_x = I_y = \frac{\pi}{64}(D_{out}^4 - D_{in}^4) \qquad (2.19a)$$

$$A = \frac{\pi}{4}(D_{out}^2 - D_{in}^2) \qquad (2.19b)$$

by substituting the equations (2.19a), (2.19b) into equation (2.5) the frequency equation for the fundamental mode is obtained :

$$f_n = \frac{(\lambda_n L)^2}{8\pi L^2}\sqrt{\frac{E(D_{out}^2 + D_{in}^2)}{\rho}} \qquad (2.20)$$
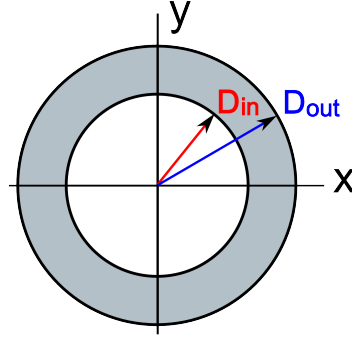
Fig. 2.6: Hollow cylindrical cross section, outside diameter D_{out}, inside diameter D_{in}.

For a multi-walled nanotube or a nanowire where $D_{out} >> D_{in}$, the resonance frequency formula for the fundamental mode becomes :

$$f_n = \frac{(\lambda_n L)^2}{8\pi} \frac{D_{out}}{L^2} \sqrt{\frac{E}{\rho}} \qquad (2.21)$$

2.1.3 Rectangular cross-section beams

For a rectangular cross section beam of width w and thickness t, figure 2.7 the area moment of inertia is given by :
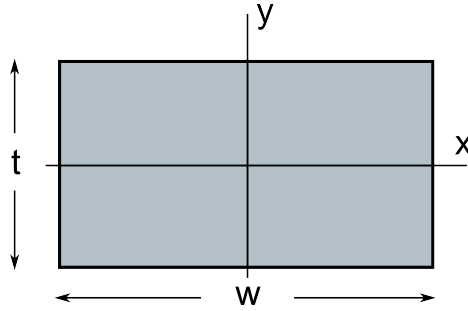
Fig. 2.7: rectangular cross section

$$I_x = \frac{wt^3}{12} \text{and} I_y = \frac{tw^3}{12} \qquad (2.22)$$

The resonance frequency for a beam vibrating in the y direction, according to (2.5) results :

$$f_n = \frac{(\lambda_n L)^2}{4\pi} \frac{t}{L^2} \sqrt{\frac{E}{3\rho}} \qquad (2.23)$$

13

The effective stiffness for the first mode in the case of a doubly clamped beam results :

$$k_{eff} = 0.762 \cdot m \cdot (2\pi f_n)^2 = 31.78 E \cdot w \left(\frac{t}{L}\right)^3 \tag{2.24}$$

2.1.4 Scale reduction effects on the mechanical behaviour of NEMS resonators

What does it happen to the mechanical properties (stiffness, resonance frequency, displacement amplitude, quality factor) of a NEMS resonator if we scale down the geometrical parameters L, t et w. If we consider the beam stiffness $k \propto w \cdot (t/L)^3$ it will reduce the same way as the beam width w. Devices with smaller stiffness can be actuated by smaller forces resulting in an improved force sensitivity ($x = F/k$). In the case of mass sensing devices with lower stiffness are more susceptible to thermal fluctuations resulting in higher frequency fluctuations (reduced dynamic range, see chapter 4). Beams with lower stiffness coefficients are advantageous for improving the sensitivity of force sensors, while deleterious for mass detection. The resonance frequency scales as $\omega_0 \propto t/L^2$. Devices with smaller dimensions will lead thus to higher resonance frequencies, increasing as $1/l$. The resonance frequency of NEMS resonator is determined from the mechanical amplitude measurements. An important parameter describing the mechanical displacement is the critical amplitude A_c representing the maximal linear displacement response of a vibrating beam. The nonlinearity effect in NEMS beam resonators has been the object of a dedicated research subject in our laboratory and were described in detail by Kacem et al. [16]. For a doubly clamped beam the critical amplitude is estimated to be $A_c = 1.685 t/\sqrt{Q}$, while for a cantilever beam $A_c = 6.3 L/\sqrt{Q}$. The force to drive the NEMS to the limit of linearity $f \propto k \cdot A_c \propto l^2$ scales down as l^2. The electrical signal S corresponding to the vibrating resonator depends on the vibrational area, which is proportional to the critical amplitude A_c time the beam length L (figure 2.8). For a doubly clamped beam the electrical signal depending only by the mechanical vibration will scale as $Scc \propto \frac{t \cdot L}{\sqrt{Q}}$ and for a clamped-free beam $Scf \propto \frac{L^2}{\sqrt{Q}}$. In both cases the area of the mechanical vibrations will scale as l^2. Assuming a scale reduction from $100 \mu m$ to $100 nm$ we will have an electrical signal reduction due to the mechanical vibration of about 6 orders of magnitude. This will lead to a decreased signal to noise ratio
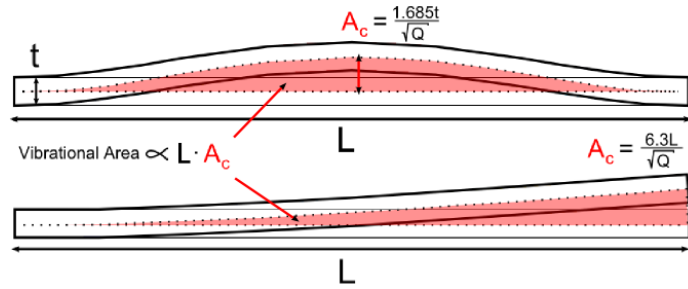
Fig. 2.8: Vibrational area of a NEMS resonator scaling as $L \cdot A_c$

SNR, which is a critical parameter for the sensors sensitivity. It is mandatory thus to evaluate the efficiency of possible transduction principles in order to chose the one which is the most adaptable to the nanoscale devices. In the next session we are going to define the criteria for an efficient electromechanical transducer and afterward evaluate their transdution gain for motion detection in NEMS devices.

2.2 Criteria definition for an efficient electromechanical transducer

Electromechanical transducers convert electrical energy into mechanical and vice versa. In the first case it is called an actuator since it uses an electrical signal to induce a mechanical motion. In the second one it is called a detector since it detects a mechanical motion. They are used for actuation and sensing of mechanical displacements. The actuator allows to control and to actuate the mechanical mass in a determined frequency. The detector permits to monitor this operation and eventual behavior changes. In vibrating electromechanical systems, measuring the mechanical displacement behavior helps us to get a full understanding of its main parameters such as amplitude, frequency and quality factor. The transition from MEMS to NEMS is associated with smaller dimensions and consequently with nanometer motion amplitudes. We showed in the previous section that the electrical signal corresponding to this displacement will decrease with l^2. Tiny electrical signals embedded in a noisy background result in deteriorated detection efficiency. Efficient coupling between the transducer and the mechanical mass is essential for the system performances. How can we solve these problems, which are the different alternatives and which fits bet-

ter to these systems ? For choosing an appropriate electromechanical transducer at the nano-scale we have to consider several important matters such as : transduction efficiency, sensitivity, on-chip integrated transduction, transduction bandwidth, low power consumption, low noise, no direct coupling between transducers etc.

The transduction efficiency express the ratio of the signal at maximum amplitude respect to the signal level far away from resonance (the background), it is otherwise called the signal to background ratio (S/B). This parameter tells the contrast between the two signal levels and the ability to distinguish a certain resonance peak from its background. When the device dimensions are reduced, the range of motion is highly decreased. The most important signal loss and consequently transduction efficiency deterioration is directly related to the smaller mechanical motions. We have to think about possible solutions to this issue. We can solve this problem in two different ways : First we have to find sensitive transducers, which are able to give the same output signals despite the scale reduction. Second we have to reduce the background level. If we are able to bring an improvement in both directions, we can increase the detection efficiency, even if we have to deal with smaller devices motions.

The resolution of a detection scheme is the capacity to resolve a signal in a noise floor and it is given by the signal to noise ratio (SNR). The transducer noise level is an important parameter since it will condition the ability to distinguish the effective signal and will determine the transduction resolution. Transducers with low noise levels and high transduction gain are highly required. In the ideal case a transducer converting efficiently the mechanical motion into an electrical signal will be limited only by the thermo-mechanical noise. Increasing the signal level is advantageous for both the SBR and the SNR.

Power consumption becomes a critical parameter when thousands of devices and arrays have to be operated in parallel, such as in figure 2.9. Thus efficient and low consumption actuators have to be designed for battery powered devices.

Smaller and ultrafast NEMS devices operating at very high frequencies need *broad band transducers* able to couple efficiently to the mechanical motion.
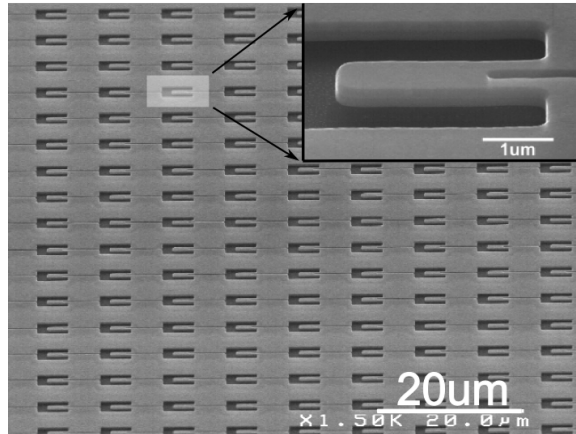
Fig. 2.9: Array of NEMS devices fabricated at LETI (Nanosystems VLSI alliance). Inset showing a single NEMS device.

The actuator through parasitic impedance couplings induces unwanted effects such as cross talking into the detector deteriorating its performances. This can result in additional noise and increased background level. For having an efficient detection we have to reduce the actuator parasitic signals getting into the detector. We have to use thus transducers that interact and couple efficiently with the mechanical element but with weak direct coupling to each other. How can we achieve it? We can reduce the cross talking and the coupling effects in two different ways : first we have to work at different frequencies and second we have to employ different principles between the transducers. With the first technique we impose distinct operation frequencies between the actuator and the detector, and thus minimize their coupling. This technique allows to couple the input/output signals only to the mechanical and to remain electrically separated from each other. An example of this technique is the capacitive actuation[17], where the electrostatic force applied to the beam has a frequency component at twice the frequency of the input signal. The beam motional capacitance (the output induced current) respect to a fixed detecting gate has a different frequency than the input signal [17, 18]. The second solution for reducing the coupling between the transducers consist on using two distinct physical interaction principles with the mechanical part. This means that the actuator and the detector will be "speaking" different languages with the mechanical part and wont interfere with each other. We have presented works based on separated actuation/detection principles, where capa-

17

citive actuation and piezoresistive detection is employed [19, 20]. In this techniques the actuation and the detection circuits interact with the mechanical beam while they affect weakly with each other. Separated transducers are also called *orthogonal transducers*[21].

On-chip integrated transducers are essential for developing portable and autonomous sensing applications. For mass production, the transducers should be *compatible with large array technologies*. We have thus to take in account actuation/detection techniques compatible with this processes.

2.3 Actuation of motion in nano-electromechanical systems

Actuation of motion in micro and nano-electromechanical systems has been realized using different techniques such as optic [22][5][23], magnetic [6][24], electrostatic [7][25][26], thermoelastic [27][28] and piezoelectric [8]. For choosing a suitable actuator we have to evaluate and compare these techniques according to the formentioned criteria.

2.3.1 Magnetomotive actuation

In the magnetomotive actuation the axis of a doubly clamped beam of length L is placed perpendicular to a static magnetic field $\vec{B}$ [6]. An alternating current I_{sd} applied along the beam generates a Lorentz force $F_L(t) = L \cdot B \times I_{sd}(t)$ figure 2.10. This force drives the beam to move in the direction transverse to its length and to the magnetic field. Depending on the orientation of the magnetic field we can cause an in-plane or out-of-plane motion. According to equation (2.14) for a mass spring damped harmonic oscillator we can write the motion equation of a resonator driven by a magnetic force $F_L(t) = L_{sd}(t)$.

$$y(\omega) = \frac{LBI_{sd}(\omega)}{m_{\text{eff}}\left(\omega_0^2 - \omega^2 + \text{j}\omega\omega_0/Q\right)} \tag{2.25}$$

Magnetomotive actuation allows to actuate NEMS at very high frequencies up to the GHz[24] even in presence of parasitic capacitances. This technique requires strong
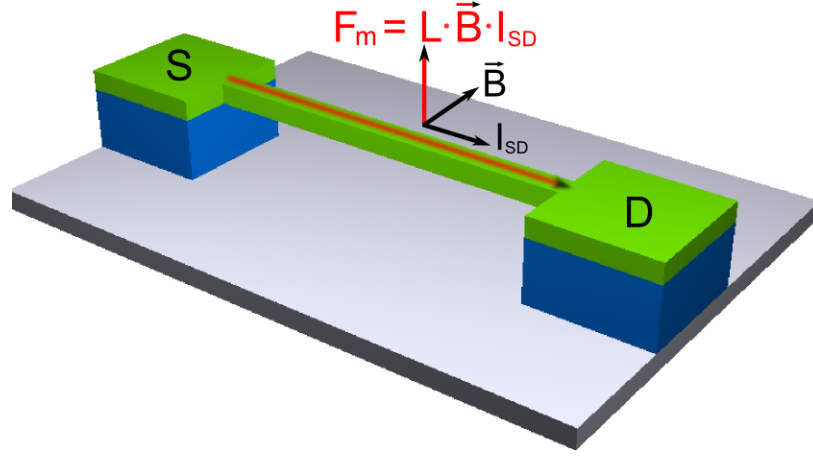
Fig. 2.10: Magnetic actuation principle of a doubly clamped beam. The current I_{sd} under the effect of a magnetic field $\vec{B}$ generates a Lorentz force $F = L \cdot \vec{B} \times I_{sd}$, where L is the beam length

magnetic fields $\vec{B} \approx 8T$[24], generated by using superconducting coils. It is not compatible for on-chip integrated actuation and not suitable for portable devices. Solutions to this problem can be thought by fabricating thin nano-magnetic films generating a magnetic field in the vicinity of the beam. The works of Bilhaut et al [10] in our laboratory were mainly focused in the integration of magnetic nanolayers for NEMS motion actuation. Some of the realizations for integrated magnetic actuation of doubly clamped beams and cantilevers are shown in figure 2.11

2.3.2 Electrostatic Actuation

The electrostatic force appears due to the attraction of separated charges. Two conducting materials with overlapping surface A and distance d from each other form a capacitor with capacitance :

$$C = \epsilon_0 \epsilon_r \frac{A}{d} \tag{2.26}$$

where ϵ_r is the dielectric constant of the insulator between the two conductors and ϵ_0 is the permittivity of free space $\epsilon_0 = 8.854 \cdot 10^{-12} F/m$. A potential difference V_g applied on this capacitor will cause an electrostatic force proportional to :

$$F_{el} = \frac{1}{2} \frac{\mathrm{d}C}{\mathrm{d}y} V_g^2 = \frac{1}{2} C_g' V_g^2 \tag{2.27}$$
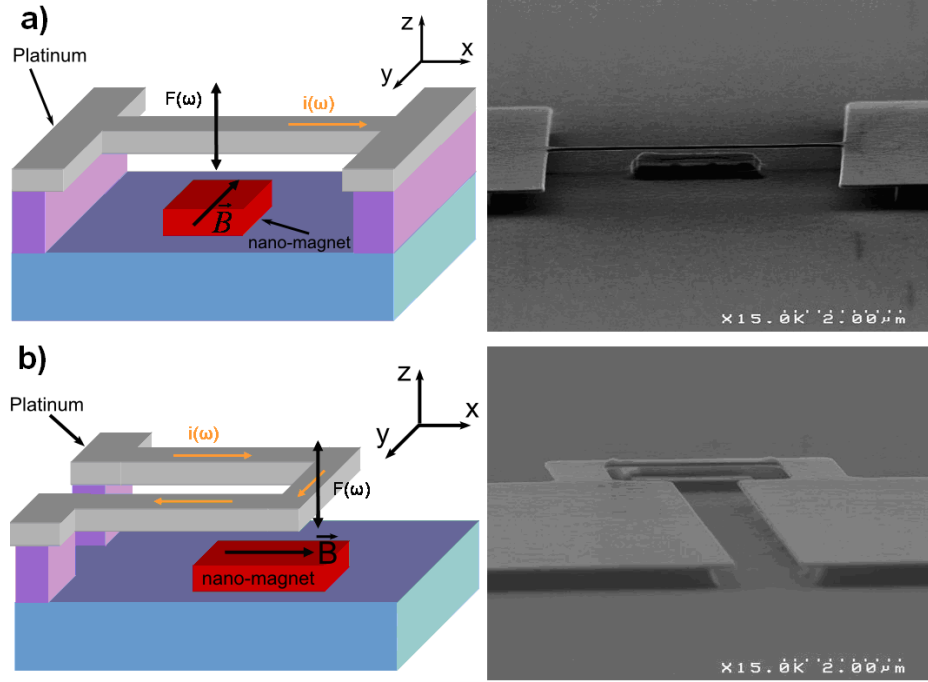
Fig. 2.11: a) Integrated magnetic nanolayer for the actuation of a doubly clamped platinum beam and b) Integrated magnetic nanolayer for the actuation of a platinum cantilever beam

where $C'_g = \frac{\mathrm{d}C_g}{\mathrm{d}y}$ is the capacitance derivative respect to the displacement. When scaling down the sizes the capacitor area will decrease as $l \cdot t$, reducing the capacitance between the gate and the beam and hence the efficiency of the electrostatic actuation. However this reduction is compensated by the smaller force required to drive the beam to nonlinearity which scales as $F \propto w \cdot t$. According to (2.14) the resonator motion results :

$$y(\omega) = \frac{C'_g V_g^2/2}{m_{\mathrm{eff}}\left(\omega_0^2 - \omega^2 + \mathrm{j}\omega\omega_0/Q\right)} \tag{2.28}$$

The main problem of capacitive actuation are the parasitic on-chip capacitances which reduce the actuation efficiency at very high frequencies. By proper RF design techniques we can use electrostatic actuation up to 1GHz [29, 30]. On-chip actuation is achieved by fabricating lateral gates on the beams. This technique is fully compatible with CMOS and VLSI technology. The same electrode used in a tree architecture can be used to actuate multiple resonators. It offers low power consumption and is suitable for portable applications.
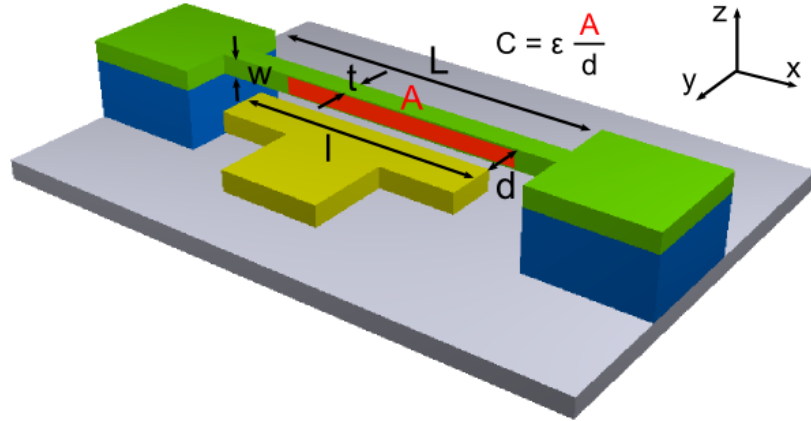
Fig. 2.12: In-plane electrostatic actuation of a doubly clamped beam. The gate-beam capacitance is proportional to $C = \epsilon \frac{A}{d}$, where A is the overlapping area between the gate and the beam, and d is the gate beam distance

2.3.3 Electrothermal Actuation

Electrothermal actuation has been largely used in the MEMS domain such as in MEMS switches [31], micromirrors[32], microtweezers[33] and AFM tips[4].

Thermo-elastic actuation is based directly on the thermal expansion of materials. It consists on a bilayer structure having different thermoelastic coefficients. When the structure is heated different internal stresses will develop inside the layers causing the structure to bend, figure 2.13. The bandwidth of this technique depends on the
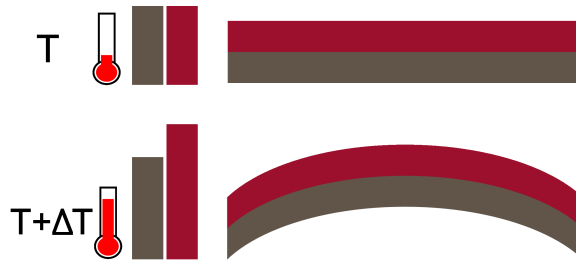
Fig. 2.13: Thermoelastic bending of a bilayer structure under heating

thermal time constant τ of the structures. In NEMS devices the time constant is $1ps < \tau < 1ns$ [21] indicating that it can be used for high frequency actuation. The power is delivered to the structure by applying a current which under the joule effect will heat the structure. The use of an electric current to provide a heat source is typical in thermally driven NEMS[27]. Using this principle our group has fabricated NEMS

devices for electrothermal actuation. An AlSi metallic loop has been patterned into the cantilever for providing the heat and actuating the structure figure 2.14. This is a very
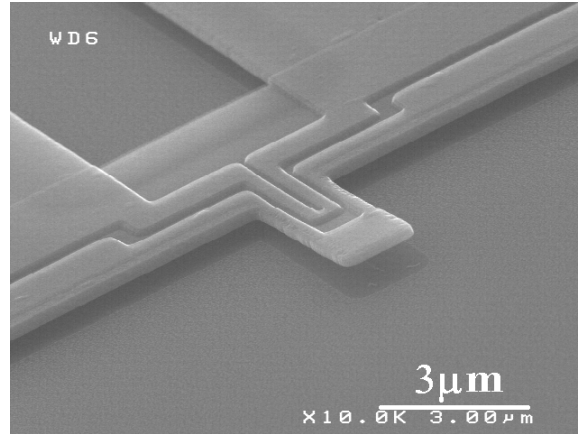
Fig. 2.14: A nanocantilever device patterned with AlSi metallic loops for electrothermal actuation and piezoresistive detection

efficient actuation technique, fully on chip and suitable with large array technologies. Since the actuation is based on the power dissipation upon the structures the main drawback is power consumption.

2.3.4 Piezoelectric Actuation

Actuation of motion through an electrical signal (voltage/current) requires transducers which are able to convert electrical energy into mechanical one. An alternative solution to this problem consists in using materials with piezoelectric characteristics. A piezoelectric crystal when subjected to a mechanical force develops an electrical potential to its extremities and becomes polarized. Vice versa the application of an electric potential across a piezoelectric crystal will cause deformations (elongation/shortening) of its geometry according to the polarity of the field and in proportion to the electric field. These behaviours are named the direct piezoelectric effect figure 2.15a and the inverse piezoelectric effect figure 2.15b.

The piezoelectric effect can be used in sensing while the inverse piezoelectric effect in actuation applications. Through a piezoelectric actuator one can convert an electrical signal into a precisely controlled physical displacement. Some common materials with piezoelectric characteristics are Quartz, ZnO, PZT, GaAs, AlN etc. In

(a) Direct piezoelectric effect   (b) Inverse piezoelectric effect
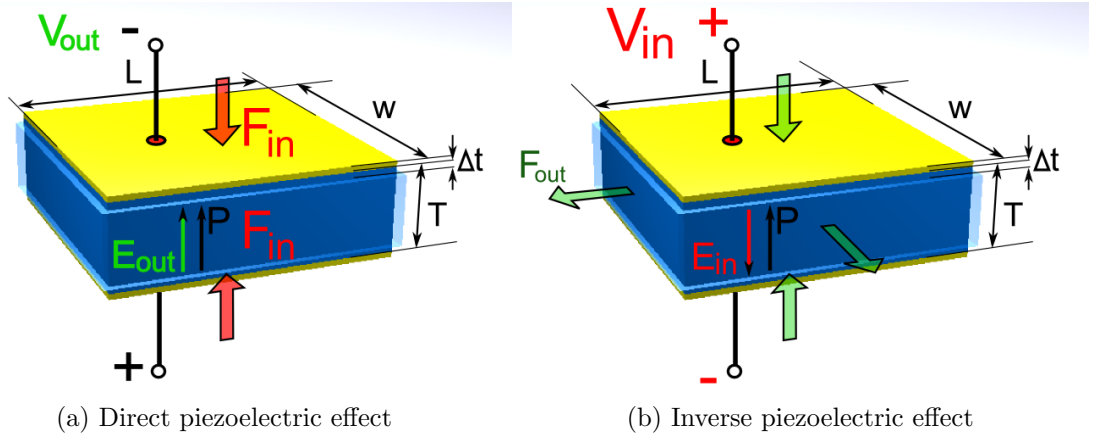
Fig. 2.15: When the applied electric field E has opposite direction to the polarization P of a piezoelectric crystal, the crystal will contract in thickness 'longitudinal' direction and will expand in the transverse direction. When the crystal is compressed the generated electric field has the same direction as that of the polarization P.

the MEMS domain actuators have been realized through deposition of piezoelectric thin films (GaAs,PZT,AlN) on silicon substrates with appropriate insulating and conducting layers [8][34][35]. Scaling the piezoelectric actuation to the nanoscale and to the NEMS domain raises a challenge because it is hard to deposit ultrathin films without deteriorating their piezoelectric properties. In thin films the piezoelectric coefficient is considerably reduced respect to bulk materials [36][37]. The main reason for this is due to limited crystallographic orientation in ultrathin films. It has been demonstrated that the intrinsic piezoelectric coefficient is dependent on the crystallographic orientation [38]. Maximizing the piezoelectric coefficient is of considerable importance in reducing the drive voltage or increasing the speed or the sensitivity of the transducer. Optimization of residual stress in individual layers to result in an overall stress compensated structure continues to pose a significant challenge. Piezoelectric actuated systems rely on active layers that provide electromechanical coupling to the structure. The purpose of the piezoelectric thin films is to generate bending in the beam by applying a moment to it. Let us assume a simple bilayer structure composed of a piezoelectric layer of aluminium nitride (AlN) and silicon Si of same thickness t. The application of an electric field E_z in the z direction will cause an elongation s_{xx} in the piezo layer along the x axis according to $s_{xx} = d_{31}E_z$, where d_{31} is the piezoelectric coefficient. When the piezolayer is strained it causes a bending

moment in the structure causing the beam to bend up or down depending on the sign of the electric field and the polarization of the layer. If we cancel the electric field the piezoelectric crystal is suddenly released from the strained position, the inertia and the elasticity of the crystal will tend to maintain a state of mechanical oscillation of constant frequency about one or more nodal points. The electric field $E_z = V/t$ can be applied through metallic electrodes (Mo/Pt/Au) contacting the piezoelectric layer, where V is the electrical potential on the electrodes. Upon the application of a high frequency signal the device is driven into resonance. figure 2.16. The static
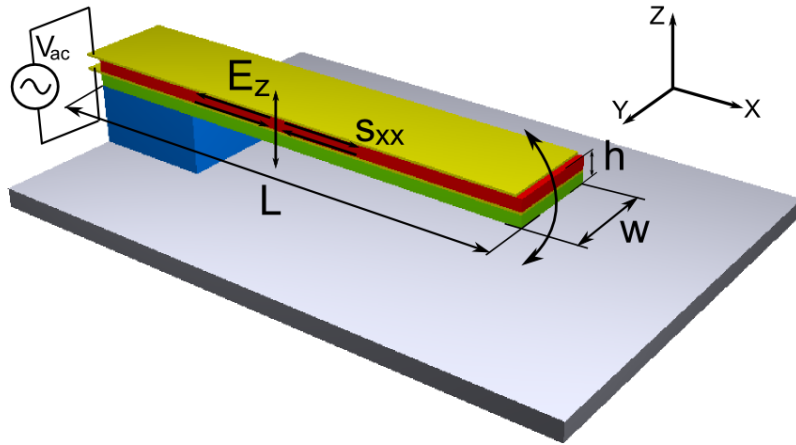
Fig. 2.16: A piezoelectric actuated bimorph cantilever

deflection δ at the tip of the piezoelectric layer due to the piezoelectric actuation when an electric voltage V is applied, is given by [39] :

$$\delta = \frac{kd_{31}L^2_{piezo}}{2E_{sub}I_{sub}}V \qquad (2.29)$$

where k is the beam spring constant, E_{sub} and I_{sub} are respectively the substrate Young's modulus and moment of inertia.

The piezoelectric method offers the advantage of extremely low power consumption, high bandwidth and linear actuation. The energy density available for actuation in piezoelectric actuators remains high, even as device sizes drop. This actuation method can be used to drive large displacements in NEMS structures at modest voltages and with low hysteresis. This method offers a high actuation bandwidth ranging from MHz-GHz[40][41] suitable for very high frequency applications. Precise control of film quality, such as stress and orientation is necessary for obtaining thin films with increased piezoelectric properties. Improvement of the sputter technology are strictly

linked to the efficiency of the piezo actuators. Recent results on our laboratory have shown the ability of integrating $100nm$ AlN piezoelectric layers into NEMS devices with excellent piezoelectric coefficients $d_{31} = 2.4pm/V$ [42][43], similar to their microscale counterparts. This technology enables the integration of an efficient actuation technique to NEMS devices.

2.4 Detection of motion in nanoelectromechanical systems

Detection of motion of NEMS resonators is far more difficult than actuation and requires extremely sensitive transducers. Here we are going to analyze the most common transduction principles used in NEMS such as, magnetomotive, capacitive and piezoresistive. We will evaluate their potential for efficient nanomechanical motion transduction. The efficiency is given by the transduction gain which is a figure of merit characterizing the mechanical to electrical signal conversion. We are going to consider a doubly clamped structure of $L = 10\mu m$, $t = 300nmm$, $w = 300nm$. The transduction gain and the output electrical signal obtained at the limit of linearity, will be avaluated for each method. We are going to estimate the effects of scale reduction on these paramters as the device sizes are scaled by a factor of 10 ($L = 1\mu m$, $t = 30nmm$, $w = 30nm$).

2.4.1 Magnetomotive detection technique

The magneto-motive detection technique[6, 44] relies on the electromotive (EMF) voltage generated by the motion of the nano-mechanical resonator which is placed perpendicular to a magnetic field $\vec{B}$, figure 2.17.

The motion of a beam resonator into a static magnetic field generates an electromotive voltage proportional to

$$V_{emf} = \eta L B \frac{dy}{dt} \tag{2.30}$$

where $\eta = 0.83806$ depends on the beam shape, and dy/dt is the derivative of the mechanical motion y respect to time. We have thus the conversion of the mechanical motion into an electrical measurable signal. Assuming an infinite source impedance,
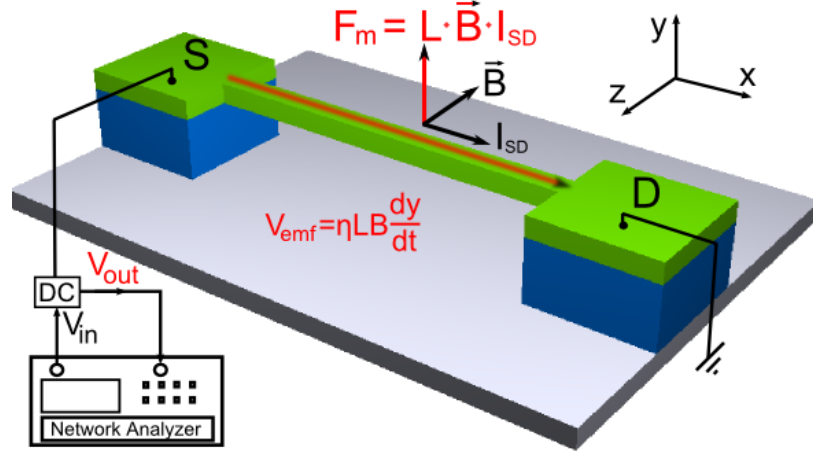
Fig. 2.17: Schematic illustration of the experimental setup used to measure the resonance properties of a doubly clamped beam. $F_m = L \cdot B \times I_{sd}$ is the magnetomotive force actuating the beam. The current I_{sd} is proportional to the input voltage V_{in} divided the beam resistance R, $I_{sd} = V_{in}/R$. DC represents the directional coupler, and the network analyzer NA measures the reflected electric signal from the NEMS resonator.
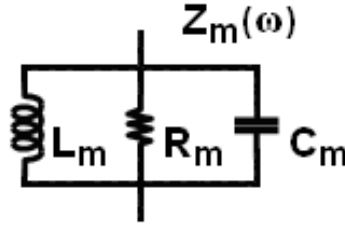
Fig. 2.18: Equivalent electromechanical impedance $Z_m(\omega)$

and substituting (2.25) in (2.30) we can write the voltage in the frequency domain as :

$$V_{emf}(\omega) = j\omega\eta LB \cdot y(\omega) = \frac{j\omega\eta L^2 B^2 I_{sd}(\omega)}{m_{\text{eff}}\left(\omega_0^2 - \omega^2 + j\omega\omega_0/Q\right)} \tag{2.31}$$

The magnetic coupled resonator is then equivalent to a parallel $R_m L_m C_m$[44] electrical circuit figure 2.18 with $Z_m(\omega)$ the electromechanical impedance. The output voltage $V(\omega)$ developed at the extremities of the parallel circuit, figure 2.18 as a function of a current source $I_{sd}(\omega)$ with infinite impedance, is given by :

$$V(\omega) = \frac{j\omega/C_m}{\omega_{LC}^2 - \omega^2 + j\omega/R_m C_m} I_{sd}(\omega) \tag{2.32}$$

Where $\omega_{LC} = 1/\sqrt{L_m C_m}$.

These relations imply equality of the resonance frequencies $\omega_{LC} = \omega_0$. From the equivalence between the Eqs (2.31) and (2.32) the electrical parameters in terms of the mechanical properties of the resonator can be identified[44] :

$$C_m = \frac{m}{\eta L^2 B^2} \tag{2.33a}$$

$$L_m = \frac{\eta L^2 B^2}{\omega_0^2 m} \tag{2.33b}$$

$$R_m = \frac{\eta L^2 B^2}{\omega_0 m} Q_0 \tag{2.33c}$$

The electromechanical impedance variation at the resonance is given by R_m. This parameter reflects the mechanical vibrations converted into an electrical impedance variation. The generated electromotive signal $V_{emf} = R_m \cdot I_{sd}$ is directly proportional to it. In order to understand the effects of the NEMS dimensions into the electrical signal we have expressed R_m as a function its geometrical parameters.

$$R_m = \frac{\eta L^2 B^2}{\omega_0 m} Q_0 = 0.169 \frac{Q_0 B^2}{\sqrt{E\rho}} \frac{L^3}{w \cdot t^2} \tag{2.34}$$

where $m_{eff} = 0.736\rho t w L$ and $\omega_0 = 6.48 \frac{t}{L^2}\sqrt{\frac{E}{\rho}}$. High impedance variations can be obtained with long and thin devices, but consequently with low resonance frequencies. If the dimensions L, w, t are scaled proportionally the R_m remains constant within the same magnetic field. How do we explain then the electromotive signal reduction when the dimensions are scaled from micro to nanometers ? This information is embedded in the drive current I_{sd} which represents the force for actuating the NEMS up to the nonlinearities ($V_{emf} = R_m \cdot I_{sd}$). The nonlinearities in a doubly clamped beam scale as $A_c = 1.685t/\sqrt{Q}$. The force to actuate the NEMS up to the nonlinearity and practically the applied current I_{sd} will reduce the same way. To understand better the electromotive signal reduction we will analyze its dependence from the critical amplitude. The maximal electromotive signal V_{emf}^{max} is obtained when the NEMS is driven up to the nonlinearity. If in equation (2.31) we substitute the displacement at resonance $y(\omega_0)$ with the critical amplitude $A_c = 1.685t/\sqrt{Q}$ we obtain :

$$V_{emf}^{max}(\omega_0) = \eta\omega_0 LBA_c = 9.11\sqrt{\frac{E}{\rho}} \frac{B}{\sqrt{Q}} \frac{t^2}{L} \tag{2.35}$$

With scale reduction the electromotive voltage V_{emf}^{max} will decrease as t^2/l. The transduction gain of the magnetomotive detection technique in [V/m] can be extracted
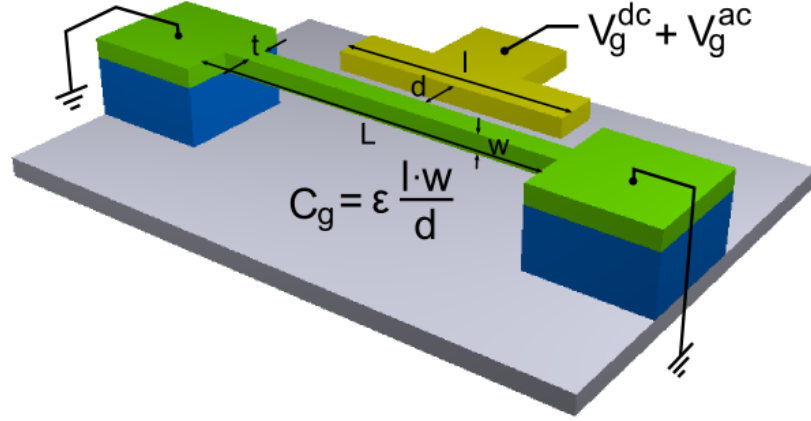
Fig. 2.19: In-plane displacement detection through capacitance variation measurements.

from equation (2.31),

$$\frac{V_{emf}}{y(\omega)} = \eta \omega l B = 5.41 \sqrt{\frac{E}{\rho}} \frac{t}{L} B \tag{2.36}$$

In order to have a high transduction gain large magnetic field should be used. We can observe from equation (2.36) that the transduction gain does not depend on the sizes of the beam but on their ratio t/l. For a doubly clamped beam of $L = 10\mu m$, $t = w = 300nm$, $B = 5T$ and $Q = 1000$ we have $\omega/2\pi = 25.55MHz$, $R_m = 8.1\Omega$, $V_{emf}^{max} = 107\mu V$ and the transduction gain $\frac{V_{emf}}{y(\omega)} = 6.7\mu V/nm$.

2.4.2 Capacitive Detection

The capacitance of two conducting materials is directly related by their distance $C_g = \epsilon_0 \epsilon A/d$. In the capacitive displacement detection technique the motion of a beam resonator is measured by monitoring the capacitance variation with respect to its gate electrode (figure 2.19). The motion of the beam with respect to the detection electrode will result in a change of capacitance. If we assume that the beam displacement $y << d$ is much smaller that the distance between them, we can approximate the capacitance variation to :

$$\delta C_g(t) \cong \left. \frac{\mathrm{d}C_g}{\mathrm{d}y} \right|_{y=0} \cdot y(t) = C_g' \cdot y(t) \tag{2.37}$$

where C_g is the beam-gate capacitance and $C_g' = \left. \frac{\mathrm{d}C_g}{\mathrm{d}y} \right|_{y=0}$ is defined as its derivative with respect to the displacement. The constant $a = l/L$ gives the electrode to beam

length ratio. The electrical charge q, stored in the system is proportional to $q = C_g V_g$, where $V_g = V_g^{dc} + V_g^{ac}$ is the beam-gate voltage. The vibrational motion of a beam resonator with respect to its fixed gate will generate a current flow across the capacitor proportional to :

$$I = \frac{\mathrm{d}q}{\mathrm{d}t} = V_g \frac{\mathrm{d}C_g}{\mathrm{d}y} \frac{\mathrm{d}y}{\mathrm{d}t} + C_g \frac{\mathrm{d}V_g}{\mathrm{d}t} \tag{2.38}$$

There are two terms contributing to the charge variation. The first is related to the tube displacement $y(t)$ and represents the effective signal. The second is due to the time varying voltage V_g. This term is always present and represents the background. By substituting eq. (2.28) in (2.38) we obtain the output current $I(\omega)$.

$$I(\omega) = \left[j\omega C_g + j\omega \frac{C_g'^{\,2} V_g^{dc2}/m}{\omega_0^2 - \omega^2 + j\omega_0\omega/Q} \right] \cdot \delta V_g^{ac} \tag{2.39}$$

The impedance between the gate and the beam is electrically equivalent to a static capacitance C_g in parallel with a series $R_m L_m C_m$ circuit, figure 2.20.
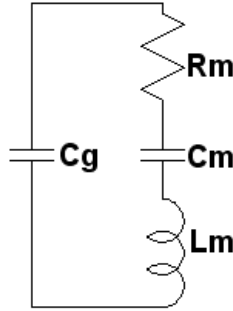
Fig. 2.20: Equivalent electrical impedance

The current $I(\omega)$ across the circuit as a function of the applied voltage for an infinite source impedance is given by :

$$I(\omega) = \left[j\omega C_g + j\omega \frac{1/L_m}{\omega_{LC}^2 - \omega^2 + j\omega R_m/L_m} \right] \cdot \delta V_g \tag{2.40}$$

where $\omega_{LC} = 1/\sqrt{L_m C_m}$. From the equivalence between the Equations (2.39) and (2.40), the electro-mechanical circuit parameters $R_m L_m C_m$ modeling the electro-

mechanical behavior of the resonator are obtained.

$$L_m = \frac{m}{C_g'^2 \cdot (V_g^{dc})^2} \tag{2.41}$$

$$C_m = \frac{C_g'^2 \cdot (V_g^{dc})^2}{m \cdot \omega_0^2} \tag{2.42}$$

$$R_m = \frac{m \cdot \omega_0}{C_g'^2 \cdot (V_g^{dc})^2 \cdot Q} \tag{2.43}$$

The motional impedance at resonance R_m reflects the conversion of the mechanical motion into an electrical current. A smaller motional capacitance at resonance corresponds to a smaller motional current. Since $I = V_g/R_m$ we have to minimize the electromechanical impedance R_m in order to have a higher output current. The maximal output current $I^{max}(\omega_0)$ is obtained when the resonator is driven up to its critical amplitude.

$$I^{max}(\omega_0) = \omega C_g' A_c V_g^{dc} = 10.88 a \epsilon_0 \sqrt{\frac{E}{\rho Q}} \frac{wt^2}{Ld^2} V_g^{dc} \tag{2.44}$$

The transduction gain for the capacitive detection technique in $\left[\frac{A}{m}\right]$ is given by :

$$\frac{I(\omega)}{y(\omega)} = \omega_0 C_g' V_g^{dc} = 6.458 a \epsilon_0 \sqrt{\frac{E}{\rho}} \frac{wt}{Ld^2} V_g^{dc} \tag{2.45}$$

For a doubly clamped beam of $L = 10\mu m$, $t = w = 300nm$, $\omega_0/2\pi = 25.55MHz$ with a lateral gate electrode of length $l = 2L/3$, gap $d = 200nm$, $V^{dc} = 5V$, $Q = 1000$ we have a static capacitance $C_g = 8.85 \cdot 10^{-17}F$, $\delta C_g = 7.07 \cdot 10^{-18}F$, $R_m = 52.39M\Omega$, $I^{max}(\omega_0) = 5.67nA$ and the transduction gain $\frac{I(\omega)}{y(\omega)} = 0.35nA/nm$. If we assume a fixed gate-beam distance d, the output current I_{out} will decrease as wt^2/l and the transduction gain as wt/L.

The capacitive detection technique widely used in MEMS becomes very complicated and inefficient with NEMS. The output current depending on the motional capacitance drops dramatically with size reductions.

2.4.3 Piezoresistive Detection

An effective and powerful way to sense the deformation of a beam or a cantilever consists in measuring its bending strain. A piezoresistive material presents a resistance
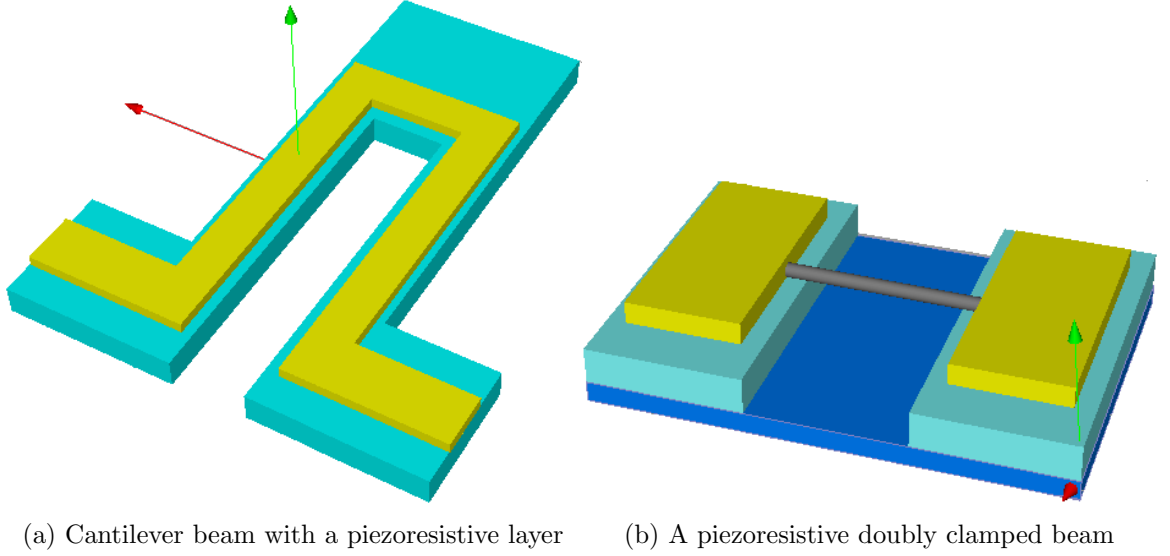
(a) Cantilever beam with a piezoresistive layer   (b) A piezoresistive doubly clamped beam

Fig. 2.21: Piezoresistive transduction configurations

change when a mechanical strain is applied on it. The relation between the resistance variation dR and the strain ϵ is given by the gauge factor GF.

$$\frac{dR}{R} = GF \cdot \epsilon = G\frac{dL}{L} \tag{2.46}$$

where R is the material resistance and L its nominal length. The strain is usually collected through piezoresistive layers or gauges [45] converting the vibrational mechanical motion into a resistance modulation (figure 2.21). In the case of a doubly clamped resonator the beam itself is a piezoresistive material. It is usually made of semiconducting doped silicon or nanowire[46, 47]. The elongation of a doubly clamped beam when its center $x = L/2$ is displaced by a distance y_c from the equilibrium is proportional to :

$$\epsilon(\omega, t) = \frac{\Delta L}{L} = \frac{1}{2L} \int_0^L \left(\frac{dy(x)}{dx}\right)^2 dx = 2.44 \left(\frac{y_c}{L}\right)^2 \tag{2.47}$$

The displacement y_c of the beam at $x = L/2$ as a function of frequency ω and time t has been previously evaluated in equation (2.14), where $y_c = y(L/2, \omega, t) = \frac{F}{m_{eff}} \frac{1}{\omega_0^2 - \omega^2 + \omega\omega_0/Q} cos(\omega t - \phi)$. Substituting in equation (2.47) we obtain the internal strain of the beam which results :

$$\epsilon(\omega, t) = \frac{2.44}{L^2} \frac{F^2}{m_{eff^2}((\omega_0^2 - \omega^2)^2) + \omega^2\omega_0^2/Q^2} cos(2\omega t - 2\phi) \tag{2.48}$$

The strain varies twice the beam motion frequency since in a vibration cycle the wire is lengthed twice. The resistance will vary with the same frequency as the strain and it is proportional to $\Delta R = GF\epsilon(\omega, t) \cdot R$, with GF the gauge factor and R the resistance of the piezoresistor. The resistance change in piezoresitive materials is measured by applying a voltage(current) and by reading the current (voltage) on the piezoresistor. The output voltage when a bias current V_b/R is applied to the piezoresistive results :

$$V_{out}(\omega, t) = \frac{2.44}{L^2} \frac{F^2}{m_{eff^2}((\omega_0^2 - \omega^2)^2) + \omega^2\omega_0^2/Q^2} GV_b \cdot cos(2\omega t - 2\phi) \qquad (2.49)$$

This technique simplifies significantly the read-out circuitry and there is no need for further alignment equipments giving access to nanoscale dimensions. Furthermore by applying a high frequency bias voltage at a frequency $V_b((2\omega + 2\Delta\omega)t)$, we would have a proportional signal component mixed to low frequencies easily measured with conventional electronics. The maximal output signal V_{out}^{max} with this method is obtained by driving the beam to the upper limit of its dynamic range.

$$V_{out}^{max} = \frac{2.44}{L^2} A_c^2 GV_b = \frac{6.92t^2}{QL^2} GV_b \qquad (2.50)$$

The transduction gain in $[\frac{V}{m}]$is equal to :

$$\frac{V_{out}(\omega)}{y_c(\omega)} = \frac{4.11t}{\sqrt{Q}L^2} GV_b \qquad (2.51)$$

For a doubly clamped semiconducting piezoresistor beam of $L = 10\mu m$, $t = w = 300nm$, $\omega_0/2\pi = 25.55MHz$, $Q = 1000$, $G = 50$ and $V_b = 2V$ we have $\Delta R/R = 3.3 \cdot 10^{-4}$, $V_{out}^{max} = 0.62mV$ and $\frac{V_{out}(\omega)}{y_c(\omega)} = 39\mu V/nm$.

In the case of a cantilever beam with a piezoresistive layer patterned on it (figure 2.22) when a static load F is applied at the end of the beam we will have a stress on its surface proportional to :

$$\sigma(x, y) = \frac{M(x)}{I}y = \frac{12F(L - x)y}{wt^3} \qquad (2.52)$$

where M is the bending moment, I the moment of inertia, y is the distance from the neutral axis.

In the case of a vibrating beam, the bending moment is $M = EI\frac{d^2y}{dx^2}$. The beam displacement is given by : $y(x, \omega) = y(\omega) \cdot \phi(x/L)$, where $y(\omega)$ gives the vibration
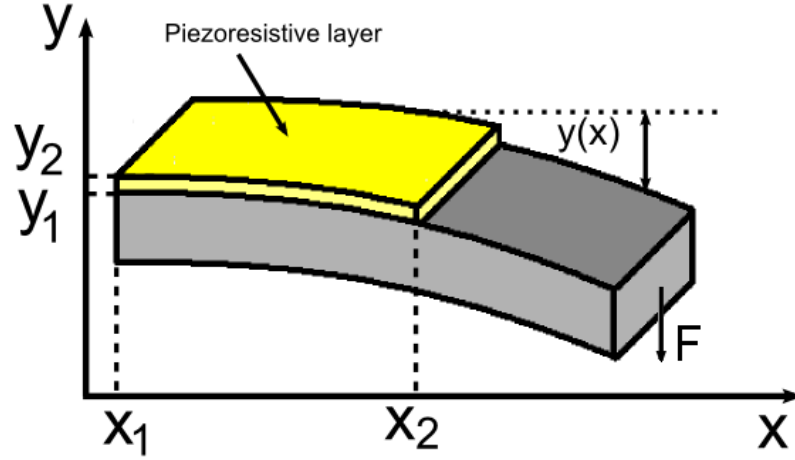
Fig. 2.22: Piezoresistive layer integrated for converting the stress due beam bending into a resistance variation

amplitude as a function of frequency ω (see equation (2.11)) and $\phi(x)$ describes the beam bending mode(see equation (2.8)).

$$y(\omega) = \frac{F_{tot}}{m_{eff}} \frac{1}{\sqrt{(\omega_0^2 - \omega^2)^2 + (\omega\omega_0/Q)^2}}$$

$$\phi(\tfrac{x}{L}) = \cos[(\lambda_1 L)\tfrac{x}{L}] - \cosh[(\lambda_1 L)\tfrac{x}{L}] - 0.734\sin[(\lambda_1 L)\tfrac{x}{L}] + 0.734\sinh[(\lambda_1 L)\tfrac{x}{L}]$$

The dynamical stress as a function of frequency ω, at a position x along the cantilever and at a distance c from the neutral axis can be calculated as :

$$\sigma(x,y,\omega) = \frac{M(x,\omega)}{I}c = E \cdot y(\omega)\frac{d^2\phi(x)}{dx^2}c \tag{2.53}$$

Assuming a piezoresistive layer of thickness h much thiner than the beam one $h << t$ in order to neglect the variations on the beam moment of inertia $I = wt^3/12$, we can find the average stress σ_{av} developed on the layer by integrating it along the layer length l and the thickness h.

$$\sigma_{av}(\omega) = E \cdot y(\omega)\frac{1}{h}\int_{\frac{t}{2}}^{\frac{t}{2}+h} c\left(\frac{1}{l}\int_0^l \frac{d^2\phi(x)}{dx^2}dx\right)dc \tag{2.54}$$

If we consider a cantilever beam of length L covered with a piezoresistive layer of length l, the ratio $b = l/L$ gives the beam coverage factor. The coefficient accounting for the stress collected by a layer of length $l = bL$ is given by the integral along x

which results :

$$\int_0^l \frac{d^2\phi(x)}{dx^2}dx = \frac{1}{L}\left(+1.376\cos\left[\frac{1.875l}{L}\right] - 1.376\cosh\left[\frac{1.875l}{L}\right]\right.$$
$$\left.+1.875\sin\left[\frac{1.875l}{L}\right] + 1.875\sinh\left[\frac{1.875l}{L}\right]\right) = \frac{S_k(l)}{L}$$

(2.56)

The stress coefficient S_k as a function of the coverage factor l/L is shown in figure 2.23 For collecting 95% of the stress on the cantilever it is sufficient to cover the beam with
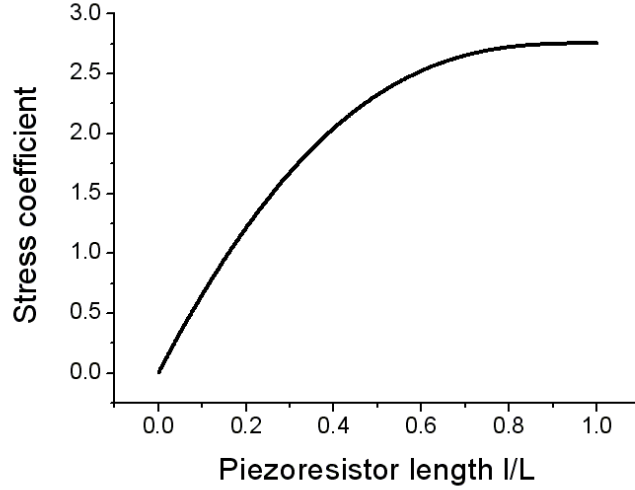
Fig. 2.23: The stress coefficient as a function of the coverage factor l/L

just 2/3 of its length. The final expression for the total stress on the piezoresistive layer as a function of its length l, thickness h results :

$$\sigma_{av}(\omega) = E\frac{(t+h)S_k(l/L)}{2bL^2}\frac{F_{tot}/m_{eff}}{\sqrt{(\omega_0^2 - \omega^2)^2 + (\omega\omega_0/Q)^2}}$$

(2.57)

The average strain ϵ_{av} can be calculated as $\epsilon_{av} = \sigma_{av}/E$. The output voltage V_{out} related to the strain variation on the piezolayer with gauge factor GF when biased by a voltage V_b results :

$$V_{out}(\omega) = \epsilon_{av}GFV_b = \frac{(t+h)S_k(l/L)}{2bL^2}GFV_b\frac{F_{tot}/m_{eff}}{\sqrt{(\omega_0^2 - \omega^2)^2 + (\omega\omega_0/Q)^2}}$$

(2.58)

For maximizing the strain variation the distance of the piezoresistors from the neutral axis should be maximized. The maximal signal obtained by driving the NEMS at the upper limit of the dynamic range is :

$$V_{out}^{max} = GFV_b\epsilon_{max} = 6.3\frac{S_k(l/L)}{2b\sqrt{Q}}\frac{t+h}{L}GFV_b \qquad (2.59)$$

We can observe from equation (2.59) the V_{out}^{max} is independent on the NEMS dimensions and depends on the gauge factor and the maximal allowed bias voltage V_b. In order to have high output signals even with nanometric beam dimensions we can envisage working with doped piezoresistors for having bigger gauge factors and applying higher voltages. The transduction gain in $\left[\frac{V}{m}\right]$ is given by :

$$\frac{V_{out}(\omega)}{y(\omega)} = \frac{S_k(l/L)}{2b}\frac{t+h}{L^2}GFV_b \qquad (2.60)$$

For a cantilever beam of $L = 10\mu m$, $t = w = 300nm$, $\omega_0/2\pi = 25.55MHz$, $Q = 1000$, with a metallic piezoresistive layer of thickness $h = 20nm$, $G = 2$ and $V_b = 100mV$ we can attain a transduction gain of $\frac{V_{out}(\omega)}{y_c(\omega)} = 1.24\mu V/nm$. If we consider a piezoresistive layer with $GF = 50$ where we can apply a bias voltage of $V_b = 2V$ we would have a transduction gain of $\frac{V_{out}(\omega)}{y_c(\omega)} = 0.624mV/nm$.

By driving the cantilever at the critical amplitude $A_c = 1.99\mu m$ we obtain the maximal $\Delta R/R = 2.48 \cdot 10^{-2}$, $V_{out}^{max} = 2.48mV$ in the metallic case and $\Delta R/R = 0.621$, $V_{out}^{max} = 1.24V$ for the semiconducting one. This results are very high since we considered the maximal linear displacement of about $2\mu m$. For a displacement of $10nm$ we would have $\Delta R/R = 1.24 \cdot 10^{-4}$, $V_{out}^{max} = 12.48\mu V$ for the metallic and $\Delta R/R = 3.12 \cdot 10^{-3}$, $V_{out}^{max} = 6.24mV$ for the semiconducting.

The higher output signal obtained with semiconducting piezoresistive cantilevers is due to the bigger transduction gain, higher dynamic range and increased applicable bias voltage. If we compare the semiconducting piezoresistive cantilever to the doubly clamped beam we have a factor of around 16 in the transduction gain. The gain is proportional to the amount of the collected stress. If we evaluate the stress collected by the doubly clamped beam at its critical amplitude $A_c = 15.98nm$ we have $\sigma = 0.997MPa$. For the same amount of displacement the stress collected by the piezoresistive layer on the cantilever is $\sigma = 16.07MPa$. These results were confirmed by finite element analysis (FEM) simulations. We have a factor of 16 between them which is reflected in the transduction gain. The problem with doubly clamped beams

is that we cannot exploit a first order stress since the regions opposite to the neutral axis have opposite sign and cancel each other (figure 2.24). The stress collected in

stress on a fixed-fixed beam

stress on a fixed-free beam
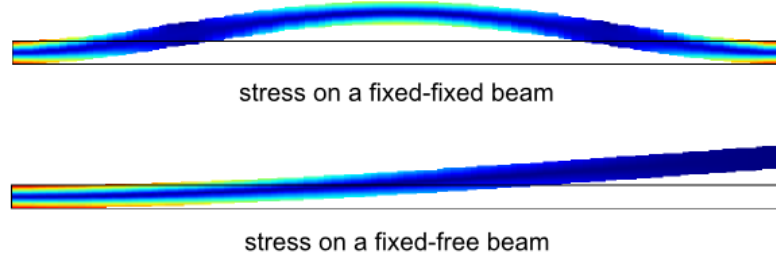
this case is a second order one due to the beam elongation. It results more efficient placing piezoresistive layers at regions experiencing maximal stress as in the case of the cantilever beams (figure 2.24). When the device dimensions are further decreased additional layers will deteriorate the mechanical properties of the NEMS devices. We can imagine cantilevers directly made of piezoresistive doped silicon or nanowire strain gauges attached to a vibrating beam as will be shown in section 3.3.1. The higher output signal obtained with semiconducting piezoresistive cantilevers respect to doubly clamped beams even if they have comparable transduction gain is due to their higher dynamic range and oscillation amplitude.

The interesting result of piezoresistive detection consist in the fact that by reducing the device dimensions we have an increased transduction gain scaling as $1/L$ (eq. (2.51), (2.60)). In figure 2.25 we have depicted the transduction gain for a beam of dimensions $L = 10\mu m$, $t = w = 300nm$, (cantilever and doubly clamped beam) when its sizes are reduced by a factor of 10.

Engineering stress/strain is an efficient way to detect the mechanical motion of smaller dimension systems, since the same force applied to a smaller cross sectional area results in an increased stress/strain variation and higher transduction gain. Instead of exploiting second order piezoresistive effect for motion transduction we can imagine solutions for collecting first order strains (see section 3.3.1). For measuring the impedance variations due to the mechanical motion we have to use appropriate measurement techniques allowing to extract the maximal signal from the NEMS and to avoid external signal attentuation. In the following section we are going to analyze the different measurement techniques employed for measuring the electromechanial
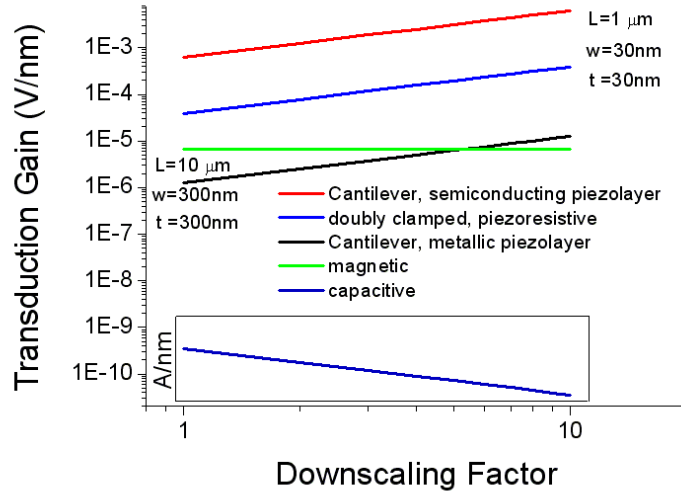
Fig. 2.25: Transduction gain for a cantilever and a doubly clamped beam obtained with the various methods as a function of the scaling factor

impedance variations.

2.5 Measurement techniques in nanoelectromechanical systems

Various measurement techniques can be employed for measuring the transduced electromechanical signal of NEMS resonators. In this section we will discuss the reflectrometry, transmission and bridge electric schemes. We will evaluate their efficiency or inefficiency when applied to these systems. Finally we want to chose a scheme which suits better and is more efficient in terms of signal to background ratio.

2.5.1 Reflectometry measurement technique

In the reflectrometry configuration the resonance frequency detection is achieved by monitoring the power reflected back at the load. The NEMS resonator is modeled by an RLC circuit with mechanical impedance Z_m, and by its nominal electrical resistance R_c figure 2.26. In this configuration the power reflected from the NEMS is proportional to the reflection coefficient Γ which is given by :
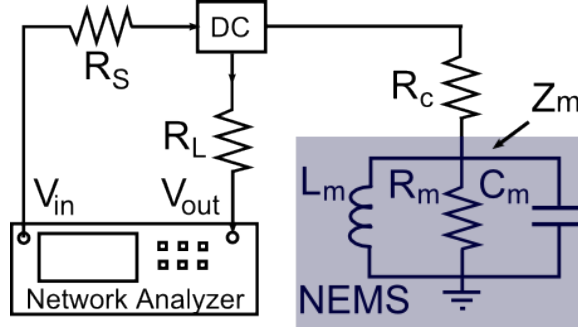
Fig. 2.26: Schematic diagram for the magnetomotive reflection technique, $R_s = 50\Omega$ is the source impedance, $R_L = 50\Omega$ is the load impedance, DC is the directional coupler and the NEMS is modeled with a parallel $R_m L_m C_m$ impedance.

$$\Gamma = \frac{Z_L - Z_0}{Z_L + Z_0} \tag{2.61}$$

Out of resonance the NEMS impedance is equal to $Z_L = R_c$, while at the resonance $Z_L = R_c + Z_m(\omega_0)$, where $Z_m(\omega_0) = R_m$ models the electromechanical impedance at the resonance. $R_s = R_L = Z_0$ is the characteristic impedance of the transmission line, typically 50Ω. Out of the resonance the reflection coefficient is equal to Γ_B which represents the background, while at resonance it is equal to $\Gamma(\omega_0)$:

$$\Gamma_B = \frac{R_c - Z_0}{R_c + Z_0} \tag{2.62a}$$

$$\Gamma(\omega_0) = \frac{R_c + R_m - Z_0}{R_c + R_m + Z_0} \tag{2.62b}$$

When $R_c \approx Z_0$ the reflection coefficient $\Gamma \approx 0$. This means there is almost no power reflected. When the electromechanical impedance $Z_m(\omega_0) = R_m$ is added to R_c the circuit is pushed further from 50Ω, thus resulting in a higher reflection coefficient and power reflected. The reflected signal is proportional to the variation of the reflection coefficient :

$$S = \frac{2 R_m Z_0}{(R_c + Z_0 + R_m) \cdot (R_c + Z_0)} V_{in} \tag{2.63}$$

where V_{in} is the incident potential. The power reflected is directly proportional to the variation of the reflection coefficient which itself is a function of the electromechanical impedance $Z_m(\omega)$ Eq. (2.62b). The signal to background ratio is given by :

$$\frac{S}{B} = \frac{2 R_m Z_0}{(R_c + Z_0 + R_m) \cdot (R_c - Z_0)} \tag{2.64}$$

If we consider the electromechanical impedance evaluated in section 2.4.1, where $R_m = 8.1\Omega$, $Z_0 = 50\Omega$ and a minimal two terminal resistance of $8k\Omega$ for a highly p++ doped silicon beam ($\rho \approx 6.9\Omega \cdot cm$) we can evaluate the SBR. The signal to background ratio obtained at resonance is equal to $SBR = -97dB$. This scheme is suitable for NEMS devices having a small two terminal resistance R_c and close to 50Ω. The detection efficiency is improved when the background is reduced. A good matching between the NEMS and the electronics provides a low reflected power out of resonance and consequently a low background. For high impedance devices where $R_c \gg Z_0$, the reflection coefficient approaches 1. A reflection measurement will be quite inefficient and insensitive to the mechanical signal, because nearly all of the power is reflected both on and off resonance.

Capacitive reflectrometry technique

Reflectrometry detection in the capacitive case is hard and complicated since the impedance to be measured is very high and the signal is almost all reflected. The electrical impedance seen from the gate is equivalent to capacitance C_g in parallel with an RLC series circuit, figure 2.20. Out of resonance the impedance seen from the gate is proportional to $|Z_{el}| \approx 1/\omega C_g \approx 70M\Omega$ which is very large. On resonance this impedance drops to $|Z_{el}| \approx R_m = 52.3M\Omega$, which still remain many orders of magnitude bigger than 50Ω. To couple efficiently the electromechanical impedance change, an impedance transformation using an LC network as shown in figure 2.27 is necessary. the equivalent on-resonance impedance at the output of the circuit is
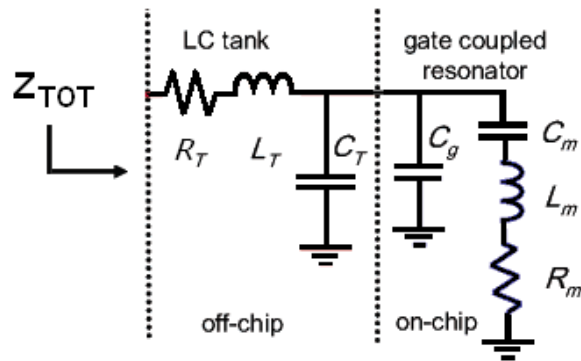
Fig. 2.27: Schematic diagram for the capacitive reflection meausurement technique

approximated to :

$$Z_{tot}(\omega_0) = \frac{Z_{LC}^2}{R_m} + R_T \tag{2.65}$$

where $Z_{LC} = \sqrt{L_T/C_T}$ is the characteristic impedance of the LC resonator, and R_T represents additional ohmic impedance as a result of losses in the inductor L_T. In order to couple efficiently and match the 50Ω at resonance ω_0, two conditions should be fulfilled :

1. $\frac{Z_{LC}^2}{R_m} = 50\Omega$

2. $\frac{1}{\sqrt{L_T C_T}} = \omega_{LC} = \omega_0$

For calculating the matching network parameters (L_T and C_T), the resonator resonance frequency ω_0 should be known. The reflection coefficient at resonance assuming $Z_{LC}^2/R_m = Z_0 = 50\Omega$ is equal to :

$$\Gamma(\omega_0) = \frac{R_t}{R_t + 2Z_0} \tag{2.66}$$

The background at resonance is given by the mismatch from 50Ω.

$$B(\omega_0) = \frac{R_t - Z_0}{R_t + Z_0} \tag{2.67}$$

The variation of the reflection coefficient which is proportional to the impedance variation at the output of the LC circuit represents the effective signal.

$$S = \frac{2Z_0^2}{(R_t + Z_0)(R_t + 2Z_0)} V_{in} \tag{2.68}$$

The signal to background results :

$$\frac{S}{B} = \frac{2Z_0^2}{(R_t - Z_0)(R_t + 2Z_0)} \tag{2.69}$$

For $R_T \approx 500\Omega$ and $Z_0 = 50\Omega$, the signal to background results $\frac{S}{B} = -34.6dB$. As it can be observed the detection efficiency of this technique is limited by the impedance mismatch.

2.5.2 Transmission detection technique

The transmission technique is used to measure the electrical signal of high impedance devices. The NEMS total impedance is modeled by $Z(\omega) = R_c + Z_m(\omega)$, where
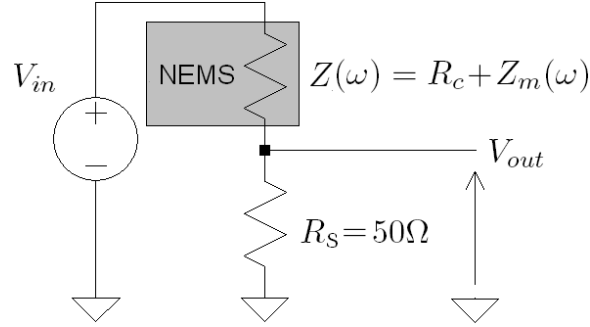
Fig. 2.28: Schematic diagram for the transmission measurement technique

R_c is its nominal resistance and $Z_m(\omega)$ its electromechanical impedance. The output voltage is proportional to :

$$V_{out} = \frac{R_s}{Z(\omega) + R_s} V_{in} \qquad (2.70)$$

The electromechanical signal can be calculated as the difference between the on-resonance and off-resonance signal.

$$S = V_{on} - V_{off} = \frac{R_s R_m}{(R_s + R_c)(R_s + R_c + R_m)} V_{in} \qquad (2.71)$$

where R_m is the real part of the electromechanical impedance at resonance. The signal to background ratio is proportional to :

$$\frac{S}{B} = \frac{R_m}{R_c + R_s + R_m} \cong \frac{R_m}{R_c} \qquad (2.72)$$

This measuring technique is broadband and suits better than the refletrometry one to devices with high impedances. If we evaluate the SBR for the device with $R_c \approx 8k\Omega$ and $R_m = 8\Omega$ we have $\frac{S}{B} = -60dB$ an improvement of $37dB$ respect to the reflectrometry technique. However since $\frac{S}{B} = \frac{R_m}{R_c}$ very high two terminal impedances R_c will lead to significant signal attenuation. For compensating the two terminal high resistance and reducing the background a balanced bridge technique should be used.

Capacitive Transmission measurements

Transmission technique in the capacitive case is implemented by measuring the induced current on the beam, eq. (2.40). At resonance the circuit impedance is equivalent to the resistance R_m in parallel with the gate capacitance C_g, figure 2.29. Given
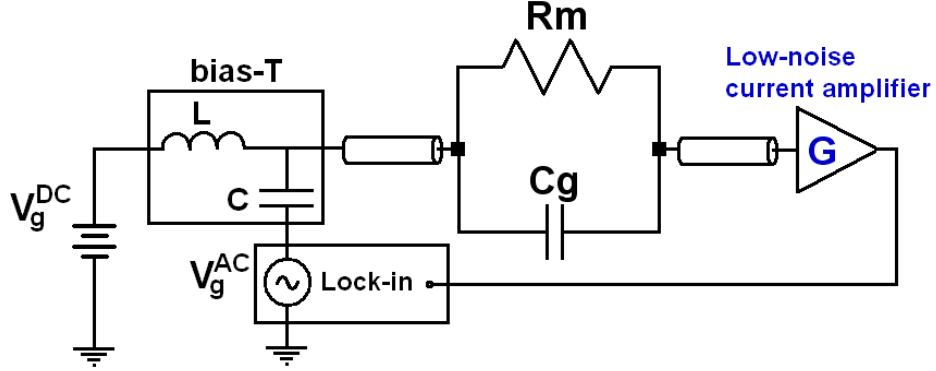
Fig. 2.29: Schematic of the measurement circuit

that the amplitude of displacement depends on the frequency of the actuation signal a synchronous lock-in technique is used for actuating and detecting the displacement. The current flowing on R_m represents the effective signal, while that of C_g represents the background. The electromechanical signal is given by :

$$I_S(\omega_0) = \frac{1}{R_m}V_{ac} \tag{2.73}$$

while the background is proportional to :

$$I_B(\omega_0) = \omega_0 C_g V_{ac} \tag{2.74}$$

The signal to background results :

$$\frac{S}{B} = \frac{I_S(\omega_0)}{I_B(\omega_0)} = \frac{1}{\omega_0 R_m C_g} = \frac{C_g'^2 \cdot (V_g^{dc})^2 \cdot Q}{m \cdot \omega_0^2 C_g} \tag{2.75}$$

The SBR obtained with this technique for the same device is $\frac{S}{B} = 2.56 dB$. In order to have a high output current it is necessary having high motional capacitances. High motional capacitances are associated to high static ones. Since $C_g' \propto lw/d^2$ and and $C_g = lw/d$, for increasing the SBR the distance between the detection gate and the beam has to be decreased to its limits.

2.5.3 Balanced bridge detection technique

The balanced bridge technique has been widely used for Si and SiC resonators [24],[48],[49]. The bridge circuit with a NEMS resonator on one side of the bridge and a balancing resonator on the other, was designed to improve the S/B ratio. The

42

voltage at the output port RO is nulled for ($\omega \neq \omega_0$), by applying two $180°$ out of phase voltages to the drive D1 and D2 ports as shown in figure 2.30. As a result of
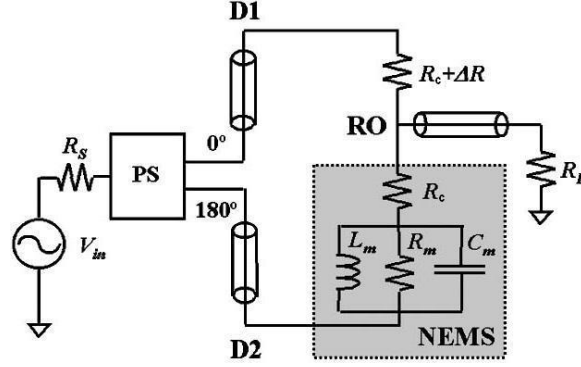
Fig. 2.30: The bridge technique configuration, PS is the phase shifter used to apply 180 phase shifted signals to the bridge extremities. R_S is the source resistance and R_L the load resistance.

nonidealities a resistance variation ΔR may be present between the two sides of the bridge. This variation will break the bridge geometry, thus resulting in a non-nulled voltage at the midpoint RO. This signal represents the background. The voltage at the midpoint RO for an infinite load impedance, assuming $Z_L >> R_c >> \Delta R >> R_m$, is given by :

$$V_0 = \frac{Z_m - \Delta R}{2R_c} V_{in} \tag{2.76}$$

At the resonace $Z_m = R_m$, and the voltage at the midpoint RO is given by :

$$V_{\omega_0} = \frac{R_m - \Delta R}{2R_c} V_{in} \tag{2.77}$$

The background B is given by :

$$B = \frac{\Delta R}{2R_c} V_{in} \tag{2.78}$$

The effective signal S results :

$$S = V_{\omega_0} - B = \frac{R_m}{2R_c} V_{in} \tag{2.79}$$

The signal to background ratio becomes then :

$$\frac{S}{B} = \frac{R_m}{\Delta R} \tag{2.80}$$

The S/B ratio depends only on R_m and ΔR. If we assume a resistance difference within 10% $\Delta R = 400\Omega$ for the device with $R_c = 8k\Omega$ and $R_m = 8$, the $\frac{S}{B} =$

$-26dB$. The advantage of this configuration is that the dependence of R_c on the (S/B) has completely dissappeared. Since the bridge is designed to be equilibrated the backround signal is due only to the resistance difference between them. Reducing the background by bridge compensation enables a higher contrast for distinguishing the effective signal and improves the detection efficiency. We can immagine the same method for compensating the background of the capacitive detection. In this case we would be limited by the capacitance variation between the two sides of the bridge. The signal to background in this case would be $\frac{S}{B} = \frac{1}{\omega_0 R_m \Delta C_g}$. Assuming 10% variation the SBR would be improved by $20B$.

2.5.4 Discussion

The most suitable actuation methods for on-chip actuation are capacitive and thermoelastic. Both of them have advantages and drawbacks. Capacitive offers low power actuation, but its efficiency is deteriorated at high frequencies. Thermoelastic is a very efficient and broad band actuation technique but expensive in terms of power consumption. Both of these techniques are compatible with large array technologies and can be used to drive simultaneously multiple cantilevers. In the following table the transduction gain and the output signal for each method is shown : Our

	Transduction gain	Maximal output signal
Magnetomotive	$\frac{V_{emf}}{y(\omega)} = 5.41\sqrt{\frac{E}{\rho}}\frac{t}{L}B = \frac{6.7\mu V}{nm}$	$V_{emf}^{max} = 9.1\sqrt{\frac{E}{\rho}}\frac{B}{\sqrt{Q}}\frac{t^2}{L} = 107\mu V$
Capacitive	$\frac{I(\omega)}{y(\omega)} = 6.458a\epsilon_0\sqrt{\frac{E}{\rho}}\frac{wt}{Ld^2}V_g^{dc} = \frac{0.35nA}{nm}$	$I^{max}(\omega_0) = 10.8a\epsilon_0\sqrt{\frac{E}{\rho Q}}\frac{wt^2}{Ld^2}V_g^{dc} = 5.67nA$
Piezoresistive fixed-fixed	$\frac{V_{out}(\omega)}{y_c(\omega)} = \frac{4.11t}{\sqrt{Q}L^2}GV_b = \frac{39\mu V}{nm}$	$V_{out}^{max} = \frac{6.92t^2}{QL^2}GV_b = 0.62mV$
Piezoresistive metallic cantilever	$\frac{V_{out}(\omega)}{y(\omega)} = \frac{S_k(l/L)}{2b}\frac{t+h}{L^2}GV_b = \frac{1.24\mu V}{nm}$	$V_{out}^{max} = 6.3\frac{S_k(l/L)}{2b\sqrt{Q}}\frac{t+h}{L}GV_b = 2.48mV$
Piezoresistive semiconducting cantilever	$\frac{V_{out}(\omega)}{y(\omega)} = \frac{S_k(l/L)}{2b}\frac{t+h}{L^2}GV_b = \frac{0.624mV}{nm}$	$V_{out}^{max} = 6.3\frac{S_k(l/L)}{2b\sqrt{Q}}\frac{t+h}{L}GV_b = 1.24V$

Tab. 2.3: Motion detection

goal was to obtain the highest signal with the lowest background. For achieving this objective we focused our effort on two directions : first, analyzing different methods for choosing the one offering the highest transduction gain nevertheless the size reduction. Second, selecting the appropriate measurement schematic for reducing the background. From the methods in table 2.3 the piezoresistive is a potential candidate for detecting the mechanical motion of nems resonators. It is fully integrable, broadband and offers the highest transduction gain. The capacitive method is frequency limited and its efficiency is reduced significantly by size reduction. Magnetomotive offers acceptable transduction gains but it is still limited by integration issues. In piezoresistive nanobeams and cantilevers the piezoresistance is an intrinsic material property and size reduction will not deteriorate these characteristics. The resistance variation in piezoresistors according to equation (2.46) is proportional to the gauge factor and the amount of elongation. The electrical signal thus can be increased by maximizing both these parameters. Choosing materials with higher gauge factors will result in a bigger resistance variation. The problem of piezoresistive materials with high gauge factors is that they are associated with high resistance. In a transmission measurement in terms of signal to background there would be no improvement since the resistance increase of the piezoresistor scales with a higher factor. The background can be reduced by using the bridge techniques. This scheme is very efficient because it allows to compensate undesired effects such as background, temperature fluctuations, parasitic couplings etc. The maximum elongation is given by the critical amplitude which represents the maximal linear behavior limit. Cantilevers offer a higher signal with respect to doubly clamped beam as they posses a higher dynamic range. The dynamic range is an important parameter characterizing a sensor sensitivity. In order to have an improved mass resolution cantilever beams in bridge configurations should be used.

Chapitre 3

Motion detection of in plane nano-cantilevers through piezoresistive nanowires

3.1 Piezoresistance and gauge factor of transducer materials

Piezoresistance express the resistance change of a material due to the mechanical strain applied on it. The relation between strain and resistance variation is given by the gauge factor GF.

$$GF = \frac{dR/R}{dL/L} = \frac{dR/R}{\epsilon} \tag{3.1}$$

where R is the piezoresistor resistance, L its length and ϵ is the longitudinal strain.

The electrical resistance of a material is a function of both its physical geometry and its resistivity :

$$R = \frac{\rho \cdot L}{A} \tag{3.2}$$

Fig. 3.1: wire resistance

where ρ is the resistivity and A is the cross sectional area of the wire.

An axial force applied on the wire causes it to stretch, thus changing its geometrical and electrical properties. The resistance variation is proportional to :

$$\frac{dR}{R} = \frac{d\rho}{\rho} + \frac{dL}{L} - \frac{dA}{A} \tag{3.3}$$

For a wire with diameter D and cross sectional area $A = \pi D^2/4$ we have :

$$\frac{dA}{A} = \frac{2dD}{D} \tag{3.4}$$

The Poisson's ratio expresses the ratio of the transverse strain respect to the longitudinal axial strain. For a wire with an axial load the Poisson ratio is defined as :

$$\nu = -\frac{dD/D}{dL/L} \tag{3.5}$$

If we substitute equations (3.4), (3.5) into equation (3.3) we obtain :

$$\frac{dR}{R} = (1 + 2\nu)\epsilon + \frac{d\rho}{\rho} \tag{3.6}$$

The gauge factor for a wire conductor becomes :

$$GF = (1 + 2\nu) + \frac{d\rho/\rho}{\epsilon} \tag{3.7}$$

There are two sources affecting the gauge factor GF, the geometric and the resistivity one. The geometric component basically comes from the fact that a strained element undergoes a change in dimension and represents the Poisson effect. The change in dimensions is the only source of piezoresistance in metals, typically of the order of 2[]. In semiconductors the mechanical strain affects the electronic band structure of the material. Changing the internal atomic position by applying a strain to the semiconductor will modify the energy band gap slightly. Small shifts can have a significant effect on the resistivity. The change in resistance is much larger than the dimensional change, resulting in $GF \approx 100$ depending on the doping, direction of the mechanical strain and the current flow respect to the crystal axes.

The relationship between the electric field and the current density in a conductor is given by the Ohm's law :

$$E = \rho \cdot j = (1 + \frac{d\rho}{\rho}) \cdot \rho_0 \cdot j \tag{3.8}$$

This can be written in a matrix form in the Cartesian coordinate system as follows :

$$\frac{1}{\rho_0} \begin{bmatrix} E_x \\ E_y \\ E_z \end{bmatrix} = \begin{bmatrix} j_x \\ j_y \\ j_z \end{bmatrix} + \frac{1}{\rho_0} \begin{bmatrix} d\rho_{xx} & d\rho_{xy} & d\rho_{xz} \\ d\rho_{xy} & d\rho_{yy} & d\rho_{yz} \\ d\rho_{xz} & d\rho_{yz} & d\rho_{zz} \end{bmatrix} \cdot \begin{bmatrix} j_x \\ j_y \\ j_z \end{bmatrix} \qquad (3.9)$$

where E_i and J_i are the components of the electric field and the current density. According to equation (3.9) the resistivity ρ can be described by a tensor with 6 different components. The relationship between the resistivity and the stress σ_{ij} is described by a tensor of rank 4, and for a cubic crystalline material it is reduced to :

$$\frac{1}{\rho_0} \begin{bmatrix} d\rho_{xx} \\ d\rho_{yy} \\ d\rho_{zz} \\ d\rho_{xy} \\ d\rho_{xz} \\ d\rho_{yz} \end{bmatrix} = \begin{bmatrix} \pi_{11} & \pi_{12} & \pi_{12} & 0 & 0 & 0 \\ \pi_{12} & \pi_{11} & \pi_{12} & 0 & 0 & 0 \\ \pi_{12} & \pi_{12} & \pi_{11} & 0 & 0 & 0 \\ 0 & 0 & 0 & \pi_{44} & 0 & 0 \\ 0 & 0 & 0 & 0 & \pi_{44} & 0 \\ 0 & 0 & 0 & 0 & 0 & \pi_{44} \end{bmatrix} \cdot \begin{bmatrix} \sigma_{xx} \\ \sigma_{yy} \\ \sigma_{zz} \\ \tau_{xy} \\ \tau_{xz} \\ \tau_{yz} \end{bmatrix} \qquad (3.10)$$

The matrix π denotes the piezoresistive coefficients π_{ij} of which only 3 are assumed to be independent (π_{11}, π_{12} and π_{44}). In most cases the π_{44} is neglected, and the indexes 11 and 12 are replaced by l and t, respectively standing for longitudinal and transversal. The expression for the electric field is :

$$E_x = \rho_0 \left[j_x + (\pi_{11}\sigma_{xx} + \pi_{12}(\sigma_{yy} + \sigma_{zz})) \cdot j_x + \pi_{44}\tau_{xy} \cdot j_y + \pi_{44}\tau_{xz} \cdot j_z \right]$$
$$E_y = \rho_0 \left[j_y + \pi_{44}\tau_{xy} \cdot j_x + (\pi_{11}\sigma_{yy} + \pi_{12}(\sigma_{xx} + \sigma_{zz})) \cdot j_y + \pi_{44}\tau_{yz} \cdot j_z \right]$$
$$E_z = \rho_0 \left[j_z + \pi_{44}\tau_{xz} \cdot j_x + \pi_{44}\tau_{yz} \cdot j_y + (\pi_{11}\sigma_{zz} + \pi_{12}(\sigma_{xx} + \sigma_{yy})) \cdot j_z \right]$$

According to equation (3.6) the resistance variation results :

$$\frac{dR}{R} = \pi_{11}\sigma_{xx} + \pi_{12}(\sigma_{yy} + \sigma_{zz}) + (1 + 2\nu)\epsilon \qquad (3.12)$$

In semiconductors the piezoresistive term is 2 orders of magnitude higher than the geometric term, which can be neglected. Thus Equation (3.12) can be simplified to :

$$\frac{dR}{R} = \pi_l \sigma_l + \pi_t \sigma_t \qquad (3.13)$$
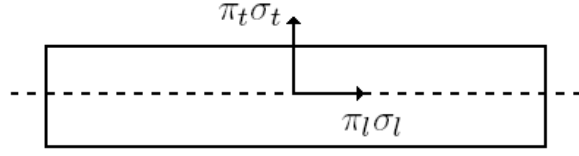
Fig. 3.2: Longitudinal and transverse piezoresistane in the nanowire

For a nanowire the primary current density and the electric field are along its axes, which may not coincide with the cubic crystal axes. The general expressions for π_l and π_t are obtained by applying coordinate transforms to the original full tensors. The longitudinal and transversal piezoresistive coefficients for an arbitrary direction are given as :
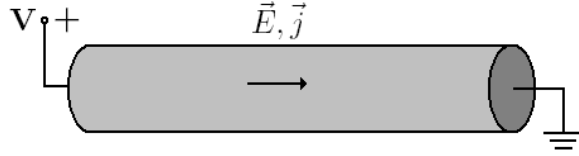
Fig. 3.3: Electric Field and current density in the nanowire

$$\pi_l = \pi_{11}^{'} = \pi_{11} - 2\left(\pi_{11} - \pi_{12} - \pi_{44}\right)\left(l_1^2 m_1^2 + l_1^2 n_1^2 + m_1^2 n_1^2\right) \tag{3.14}$$

$$\pi_t = \pi_{12}^{'} = \pi_{12} + \left(\pi_{11} - \pi_{12} - \pi_{44}\right)\left(l_1^2 l_2^2 + m_1^2 m_2^2 + n_1^2 n_2^2\right) \tag{3.15}$$

Where (l_1, m_1, n_1) and (l_2, m_2, n_2) are the sets of direction cosines between the longitudinal resistor direction and the crystal axes.

The piezoresistance coefficients for bulk silicon are given in the following table :

Type	Resistivity	π_{11}	π_{12}	π_{44}
Units	$\Omega \cdot cm$	$10^{-11}Pa^{-1}$	$10^{-11}Pa^{-1}$	$10^{-11}Pa^{-1}$
n-type	11.7	-102.2	53.4	-13.6
p-type	7.8	6.6	-1.1	138.1

Tab. 3.1: Piezoresistive coefficients for bulk silicon

In the following table there are given the longitudinal and transverse piezoresistance coefficients for various combinations of direction in cubic crystals :

Longitudinal Direction	π_l	Transverse Direction	π_t
(100)	π_{11}	(010)	π_{12}
(001)	π_{11}	(110)	π_{12}
(111)	$\frac{1}{3}\left(\pi_{11} + 2\pi_{12} + 2\pi_{44}\right)$	$(1\bar{1}0)$	$\frac{1}{3}\left(\pi_{11} + 2\pi_{12} - \pi_{44}\right)$
$(11\bar{0})$	$\frac{1}{2}\left(\pi_{11} + \pi_{12} + \pi_{44}\right)$	(111)	$\frac{1}{3}\left(\pi_{11} + 2\pi_{12} - \pi_{44}\right)$
$(11\bar{0})$	$\frac{1}{2}\left(\pi_{11} + \pi_{12} + \pi_{44}\right)$	(001)	π_{12}
(110)	$\frac{1}{2}\left(\pi_{11} + \pi_{12} + \pi_{44}\right)$	$(1\bar{1}0)$	$\frac{1}{2}\left(\pi_{11} + \pi_{12} - \pi_{44}\right)$

Tab. 3.2: Longitudinal and transversal piezoresistive coefficients for various combinations of directions in cubic crystals

In many silicon micromachined devices, resistors are oriented along the $<110>$ direction in (100) plane wafers. For a p-type bulk resistor along the $<110>$ and $<111>$ direction we have respectively :

$\pi_l{<}110{>} = 71.8 \ \pi_t{<}110{>} = -66.3$,

$\pi_l{<}111{>} = 93.5 \ \pi_t{<}111{>} = -44.5$.

3.2 Piezoresistor choice

Piezoresistive strain sensors directly integrated into the devices prove to be very useful for nanoscale motion detection. In this context various question arise : Which type should we use, metallic or semi-conducting piezoresistors ? How can we optimize the piezoresistive transducers for an efficient motion detection ? The figure of merit of piezoresistive displacement transduction is the signal to noise ratio. This means we should increase the transduction gain (sensitivity) while maintaining a low noise level. The transduction gain can be maximized by using large gauge factor sensors suggesting semi-conducting materials. The main noise sources generated on the transducers are flicker noise, Johnson noise and the piezoresistively transduced thermo-mechanical noise.

Flicker noise is related to the conductance fluctuations on a resistor. It is called $1/f$ noise because its noise power spectral density goes down as the inverse of the frequency. The empirical model proposed by Hooge [50] states that the voltage noise

power spectral density ($[V^2/Hz]$) of a homogeneous resistor is proportional to the total number of carriers N enclosed in its volume according to :

$$S_H = \frac{\alpha V_B^2}{Nf} = \frac{\alpha V_B^2}{Ltwpf}$$ (3.16)

where α is a dimensionless parameter called Hooge constant which was found to vary with annealing from $3 \cdot 10^{-6} - 3 \cdot 10^{-4}$. V_B is the bias voltage applied to the piezoresistor and f the frequency. The number of carriers N in a semiconductor with uniform doping is proportional to its volume $V = Ltw$ times the doping concentration p. We can observe that the 1/f noise power density varies inversely with the volume and the doping.

The *Johnson noise* depends only on the resistance of the resistor R, and the temperature T. It has a spectral density independent of frequency otherwise called 'white noise'. The voltage noise power density ($[V^2/Hz]$) is :

$$S_J = 4k_BTR = 4k_BT\rho\frac{L}{tw}$$ (3.17)

Both the Johnson and $1/f$ noise can be predicted from the doping and geometry. The noise level can be minimized by correctly dimensioning the gauges and finding the right doping concentration. We will consider first how the noise is affected by the geometry.

For a fixed doping density the Hooge's noise is inversely proportional to the volume. This means we have to increase the volume ($V = Ltw$) of the resistor for having a lower noise. Fixed doping concentration implies fixed resistivity. In order to obtain a smaller Johnson noise for a given resistivity we have to decrease the L/tw ratio. In both cases lower noise is obtained by maximizing the cross-sectional area of the piezoresistor ($s = tw$). $1/f$ noise is a frequency dependent noise which is decreased significantly at high frequencies. Usually at high frequencies Johnson becomes the dominant source of noise. The Johnson noise can be reduced further by diminishing the piezoresistor length. The limit of length reduction is the point where the flicker noise starts to become comparable to the Johnson noise as a result of the volume decrease.

Assuming a fixed geometry what would be the appropriate doping concentration for obtaining a lower noise? In order to decrease both noises, we have to increase the doping concentration. In the case of the Hooge's relationship this will result in a higher number of carriers, while in the case of Johnson noise will result in lower resistivity and lower noise. Another important parameter dependent on the resistivity that has to be taken in account is the gauge factor. This parameter becomes smaller as the resistivity goes down. Although a higher doping concentration offers a lower noise, it has costs in terms of reduced sensitivity. Our objective is to maximize the signal to noise ratio. We should decrease the noise as much as possible without affecting significantly the gauge factor. This requires to find the right doping concentration for which the signal to noise ratio is maximized. Assuming that Johnson is the dominant noise source at high frequencies, the signal to noise ratio will be proportional to :

$$SNR \propto \frac{GFV_b}{\sqrt{\rho}} \qquad (3.18)$$

with GF, V_b, ρ being respectively the gauge factor, the bias volage applied to the piezoresistor and ρ its resistivity.

According to experimental data of Mason et al[], Tufte et al [] and Kerr et al[], the gauge factor scales down with doping concentration p as :

$$P(p) = log\left(\frac{b}{p}\right)^a \qquad (3.19)$$

with $a = 0.2014$ and $b = 1.53 \cdot 10^{22}$. The resisitivity of doped semiconductor is given by :

$$\rho = \frac{1}{q\mu(p)p} \qquad (3.20)$$

where μ is the mobility and q the charge. The signal to noise ratio as a function of doping concentration p results :

$$SNR \propto V_b \cdot log\left(\frac{b}{p}\right)^a \sqrt{q\mu(p)p} \qquad (3.21)$$

The SNR as a function of doping concentration is plotted in figure 3.4. We can observe that the signal to noise ratio is maximised for heavy doping concentrations.

Another important problem is the power dissipated on the gauges. The power dissipation is proportional to the square of the bias voltage and inversely proportional
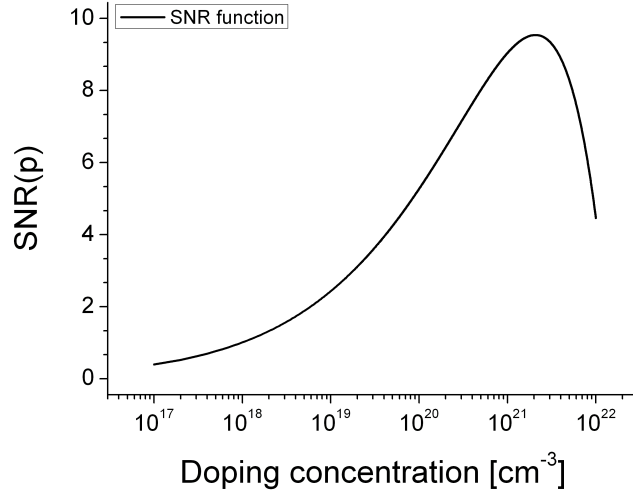
Fig. 3.4: signal to noise ratio as a function of doping concentration

to the resistance $P = V^2/R$. In order to have a lower consumption higher resistivities are required. For a constant power consumption P, the signal to noise ratio is proportional only to the gauge factor.

$$SNR \propto GF\sqrt{P} \tag{3.22}$$

A good compromise between optimal signal to noise ratio and low power consumption is obtained for doping concentration of $10^{-19}cm^{-3}$. Let us consider a metallic and semi-conducting piezoresistor of resistance 50Ω and $5k\Omega$ respectively, biased at $V_b = 100mV_{rms}$. The common gauge factor of metallic piezoresistors is of the order 1-2, resulting in a $SNR \propto 2V_b/\sqrt{50\Omega}$. In order to obtain the same SNR ratio with a semi-conducting piezoresistor a minimum gauge factor of 20 is required, with a power consumption of two orders of magnitude smaller.

Thermomechanical noise is another noise source, consisting on the piezoresistively transduced mechanical fluctuations due to thermal energy. The voltage noise power density is proportional to the force spectral density of the cantilever times the gauge factor :

$$S_{TH} \propto GFV_b\frac{4M_{eff}\omega_0 k_B Tk}{Q} \tag{3.23}$$

Both the signal and the voltage noise power scale the same way with the bias voltage and the gauge factor. If thermomechanical is the dominant noise source, the signal

to noise ratio results independent from GF and V_b. Thus the signal to noise ratio would be independent of the nature of the piezoresistor. The thermomechanial noise is highest at resonance since the motion fluctuations are bigger. Usually this type of noise is smaller than Johnson and 1/f. Considering the restricted bandwidth of the measurements, the contribution of this noise can be neglected.

Semiconducting nano gauges which can be attached to moving structures offer the advantage of being fully integrable and do not require additional layer deposition. Semiconducting gauges support higher bias voltages and are more robust to charges. The bias voltage can be tuned in order to find an optimum between the SNR and the power consumed. The output signal would be higher with high gauge factors GF resulting in a superior signal to background and easier to detect.

3.3 In-plane motion NEMS architecture

Technological advances require to combine different functionalities and systems into a single electronic chip. Co-integration of nano-mechanical elements and electronics devices necessitates high end fabrication processes, comparable with bottom-up synthesis techniques and compatible with CMOS technology. Using the same fabrication process for the mechanics and electronics is indispensable for obtaining them on a single chip. Based on these constraints we have chosen an in-plane motion architecture for the for-mentioned reasons. The device can be fabricated using compatible CMOS-technology and very large scale integration processes. The in-plane design offers an increased flexibility of design and simplifies the process development. The NEMS are fabricated using a 200-mm silicon-on-insulator (SOI) wafer of (100) orientation with a 160-nm-thick top silicon structural layer (resistivity $10\Omega \cdot cm$) and a 400-nm-thick sacrificial oxide layer. The top silicon layer was implanted with boron ions (p-type) through a thin layer of thermal oxide. Homogeneous doping ($3 \cdot 10^{19}cm^{-3}$) in the whole thickness of the top silicon was obtained through specific annealing step (for material reconstruction and doping activation), resulting in top layer resistivity of approximately $6m\Omega \cdot cm$. A hybrid e-beam/DUV lithography technique [14] was used to define the nano-resonators and electrode pads, respectively. Top silicon layer was etched by anisotropic reactive ion etching (RIE). In order to decrease the lead resistances, the interconnecting leads have been thickened with a 650 nm thick AlSi layer,

a typical metal for CMOS interconnections process. Finally, the nano-resonators have been released using a vapor HF isotropic etching to remove the sacrificial layer oxide beneath the structures.

The NEMS devices are intended for mass sensing applications based on frequency shift as a result of mass variation. The mass sensors can be developed using two common geometries such as doubly clamped beams and cantilevers. We have decided to work with cantilevers because of their higher dynamic range. The dynamic range affects directly the mass sensitivity of these devices and it is smaller in the case of doubly clamped beams [51].

The NEMS device is composed of a fixed-free lever beam, two piezoresistive gauges and a lateral actuation electrode figure 3.5. These components are patterned on the
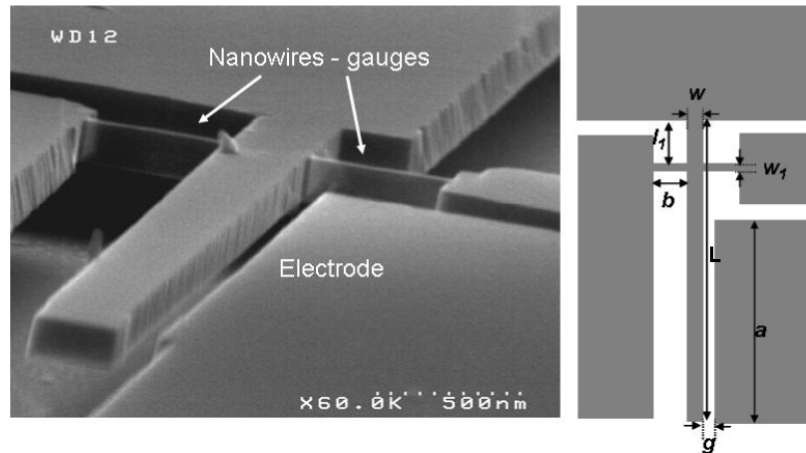
Fig. 3.5: Geometry of an in-plane NEMS resonator with lateral gate electrostatic actuation. The piezoresistive p++ nanowire gauges are used to convert the mechanical strain exerted by the beam into a resistance variation. The nanowire gauges are simetrical to each other for allowing a differential bridge measurement.

same p^{++} doped silicon layer within a single lithographic process. This simplifies enormously the fabrication process and reduces the lithographic steps. The piezoresistive gauges are attached to the cantilever and experience a strain variation during its motion. Their goal is to convert a mechanical displacement into a resistance variation. The gauges are positioned at a distance $l_1 = 0.15L$ from the cantilever end. This value was chosen to maximize the stress exerted on the gauges during the cantilever

motion. The gauges have been etched along the $< 110 >$ direction in order to benefit from the high gauge factor associated with p^{++} doped silicon. The driving electrode was patterned along one side of the vibrating beam for electrostatic actuation. The device dimensions and general architecture are given in table 3.3. This design benefits

L	w	l_1	b	w_1	a	g
5 μm	300 nm	700 nm	500 nm	80 nm	3.5 μm	200 nm

Tab. 3.3: Typical values of the device

from two major amplifying effects, which contribute on maximizing the stress on the gauges. First the leverage arm effect , and second the quality factor which amplifies the displacement at resonance by a factor of Q. To evaluate the dynamical behavior of the NEMS geometry shown in [12], we used a model based on Euler-Bernoulli beam theory.

3.3.1 In-plane actuation and motion transduction through piezoresistive nanowire gauges

The cantilever is actuated in-plane electrostatically by a lateral electrode. The force applied to the cantilever is proportional to :

$$F = \frac{1}{2}\frac{dC}{dy}V_{\mathrm{g}}^2 \tag{3.24}$$

where C is the cantilever gate capacitance and V_{g} is the gate voltage.

The cantilever gate capacitance is evaluated considering a parallel plate capacitor model. The capacitance per unit length is given by :

$$C = \frac{t\epsilon_0}{g} \tag{3.25}$$

where g is the gate cantilever gap and t is the gate thickness.
Considering a first order development of $\frac{dC}{dy}$ in $y(x,t)$ we have that :

$$\frac{dC}{dy} = \frac{t\epsilon_0}{(g - y(x,t))^2} = \frac{t\epsilon_0}{g^2} + \frac{2t\epsilon_0 y(x,t)}{g^3} \tag{3.26}$$

The voltage applied to the gate can be the sum of a DC and an AC term :

$$V_{\mathrm{g}} = V_{\mathrm{dc}} + V_{\mathrm{ac}}\cos(\omega t) \tag{3.27}$$

Putting together equation (3.24), (3.26) and (3.27) we obtain the force per unit length applied to the cantilever.

$$F(x,t) = \left(\frac{t\epsilon_0}{2g^2} + \frac{t\epsilon_0 y(x,t)}{g^3} \right) \left(V_{\mathrm{dc}}^2 + \frac{V_{\mathrm{ac}}^2}{2} + 2V_{\mathrm{ac}}V_{\mathrm{dc}}\cos(\omega t) + \frac{V_{\mathrm{ac}}^2}{2}\cos(2\omega t) \right) \tag{3.28}$$

The force will cause a displacement on the cantilever. Its displacement is governed by the Euler-Bernoulli beam equation :

$$EI\frac{\partial^4 y(x,t)}{\partial x^4} + \rho S\frac{\partial^2 y(x,t)}{\partial t^2} + b\frac{\partial y(x,t)}{\partial t} = F(x,t) \tag{3.29}$$

From this model, we can easily compute the first Eigen frequency, ω_0, the leverage arm factor α as well as the force F_g acting on the gauges. The device consists in a fixed free cantilever with certain displacement constraints imposed by the gauges at the attachment position l_1. We consider that the gauges are stiff enough so there is no in-plane displacement but a rotation at this position. The beam motion on the left and right side is continuous independently from the gauges. The continuity law imposes that the slope and the curvature of the cantilever at the gauge position should be the same on both sides. The equivalent model is that of a fixed free cantilever pinned at the gauge distance as shown in figure 3.6. The wave function for the fundamental mode has been calculated using the following boundary conditions : $u_1(0) = u_1(l_1) = u_2(l_1) = 0$, $u_1^{'}(0) = 0$, $u_2^{''}(L) = 0$ and $u_2^{'''}(L) = 0$, where u_1 and u_2 are the wave function of the fundamental mode for the left and right side of the lever respectively. In order for u_n to be a base it should satisfy the normalization condition :

$$\frac{1}{L} \left(\int_0^{l_1} (u_1[x])^2\, dx + \int_{l_1}^L (u_2[x])^2\, dx \right) = 1 \tag{3.30}$$

The continuity relationship of the wave at the anchoring position imposes the same slope and curvature for both sides, which is expressed in terms of boundary conditions as $u_1^{'}(l_1) = u_2^{'}(l_1)$ and $u_1^{''}(l_1) = u_2^{''}(l_1)$. The Galerkin projection of the Euler-Bernoulli
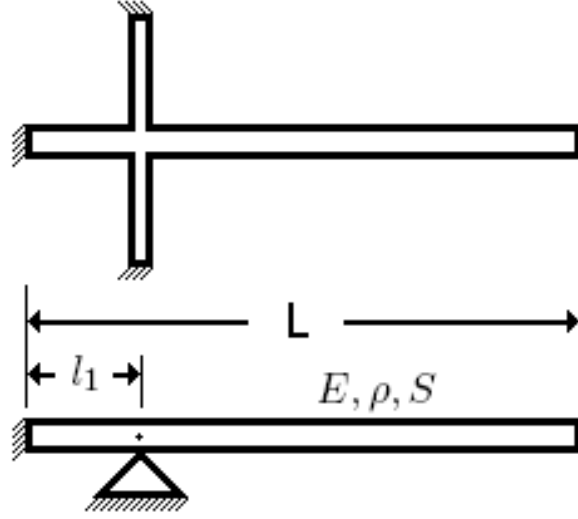
Fig. 3.6: Analytical model

equation on the first modal vector leads to a mass-spring damped harmonic oscillator model.

$$
\begin{aligned}
y''(t) + \frac{b}{\rho S}y'(t) &+ \left(\frac{EI}{\rho S} * \lambda_1^4 - \frac{t\epsilon_0(V_{ac}^2 + 2V_{dc}^2)}{\rho S g^3} \right) y(t) = \\
&= \frac{1}{\rho S L} \int_{L-a}^{L} \left(\frac{t\epsilon_0 \left(V_{ac}^2 + 2V_{dc}^2\right)}{2g^2} + \frac{2t\epsilon_0 V_{ac} V_{dc} cos(\omega_0 t)}{g^2} + \frac{t\epsilon_0 V_{ac}^2 cos(2\omega_0 t)}{2g^2} \right) u_2(x)dx \\
&= \frac{\eta}{\rho S L}(F_0 + F_1 \cos(\omega t) + F_2 \cos(2\omega t)) = \frac{1}{M_{eff}}(F_0 + F_1 \cos(\omega t) + F_2 \cos(2\omega t))
\end{aligned}
$$

$$(3.31)$$

where η is a constant and represents the projection of the electrostatic force on the modal base and $M_{\text{eff}} = \rho \text{SL}/\eta$ represents the effective mass.

$$
\eta = \int_{L-a}^{L} u_2(x)dx = 0.726 \tag{3.32}
$$

From equation (3.31) We can distinguish three different force components. A static force F_0 and two sinusoidally ones, respectively at ω and 2ω. The force transferred on the gauges F_g has been calculated as the difference of the shear forces between the left and right side of the pinning position.

$$
F_g(\omega) = EI \left[\frac{d^3 u}{dx^3} \right]_{l_1-}^{l_1+} y_1(\omega) = 9.28 EI\lambda_1^3 \cdot \frac{\omega_0^2}{\omega_0^2 - \omega^2 + j\omega\omega_0/Q_0} \cdot F_{el}(\omega) \tag{3.33}
$$

where $\lambda_1 = 2.1178/l$.

Finally the leverage arm factor α has been estimated and the force transferred to the gauges is proportional to :

$$F_g(\omega) = \alpha \frac{\omega_0^2}{\omega_0^2 - \omega^2 + j\omega\omega_0/Q_0} \cdot F_{el}(\omega) \tag{3.34}$$

At resonance where $\omega = \omega_0$ the force amplification is given by :

$$\frac{F_g(\omega_0)}{F_{el}(\omega_0)} = \alpha \cdot Q \tag{3.35}$$

A comparison with the results of Finite Element Modeling (FEM) largely validated our analytical model, as shown in table 3.4.

	$\omega_0/2\pi$	α	M_{eff}
Analytical model	21.10 MHz	6.05	140 fg
FEM model	20.65 MHz	5.2	NA

Tab. 3.4: Comparison of predictions of analytical and FEM models - M_{eff} is the effective mass

The slight discrepancies are due to the assumption that the gauge anchoring is purely rotational, with no bending moment introduced by the gauges. This design permits to exploit a first order piezoresistive effect. The cantilever beam applies a longitudinal force F_g on the gauges causing a stress proportional to F_g/s, where s is the gauge cross-sectional area. The strain ϵ induced on the gauges is transduced into a resistance variation ΔR through the piezoresistive effect :

$$\frac{\Delta R(\omega)}{R} = GF \cdot \frac{F_g(\omega)}{2 \cdot s \cdot E} \tag{3.36}$$

where E is the Young's modulus of the gauges. The resistance variation can be read-out by imposing a bias current I_b on the gauges and measuring the potential variation at the bridge center. The current is imposed by applying two 180 out of phase bias voltage V_b to the gauges extremities. The purpose of this schematic is to suppress the continuous background at the bridge center and getting a nulled voltage.

3.4 Circuit electrical behaviour at high frequencies

Understanding the electrical behavior of the "test-bench - NEMS" set and it optimal operation point is crucial and necessary for having correct measurements. The NEMS devices present a two terminal resistance of $10 - 30k\Omega$. This resistance combined with cables and parasitic capacitances composes a low-pass filter circuit. The same way it will present a flat region and a cut-off frequency and can be modeled with an equivalent electrical circuit. The flat region depends on the circuit resistances and the cut-off frequency on its capacitances. In order to model the "test-bench - NEMS" with an equivalent electrical circuit two parameters are required : the NEMS resistances and the cable capacitances. The cable resistance has been neglected since it is much smaller $50\Omega << 10k\Omega$ respect to the NEMS one. The NEMS capacitance which is also much smaller than that of the cables $100pF/m$ is also neglected. The two terminal DC resistance of the NEMS branches has been evaluated using two point measurements. The results obtained from the device under test were, $R_2 = 16.18k\Omega$, $R_3 = 17.42k\Omega$ and $R_4 = 4.78k\Omega$.

The second experiment consisted on measuring the frequency response of the "NEMS-testbench" set and define the branch capacitances. For measuring the branch capacitances we have simplified the measurement configuration. This was done with the aim of measuring only one branch capacitance at a time. This was achieved by applying the bias only in one port, grounding the other and measuring in between figure **??**. The measurement have been performed with a Stanford S830 lock-in, with input impedance of $R = 100M\Omega$ and $C = 25pF$. The output voltage of the circuit V_{out} is proportional to :

$$V_{out}(\omega) = \frac{R_3}{(R_2 + R_3)(1 + j\omega C_{tot}R_4) + j\omega C_{tot}R_2R_3}V_2(\omega) \qquad (3.37)$$

where $C_{tot} = C_{lock-in} + C_4$ is the total capacitance.

The cut-off frequency of the system is given by :

$$f_c = \frac{R_2 + R_3}{(R_2 + R_3)R_4 + R_2R_3}\frac{1}{2\pi \cdot C_{tot}} \qquad (3.38)$$

The branch capacitance has been estimated as :

$$C_{tot} = \frac{R_2 + R_3}{(R_2 + R_3)R_4 + R_2R_3}\frac{1}{2\pi \cdot f_c} \qquad (3.39)$$

(a) Measurement configuration of the branch ca- (b) Electrical schematic of the capacitance measu-
pacitances   rement
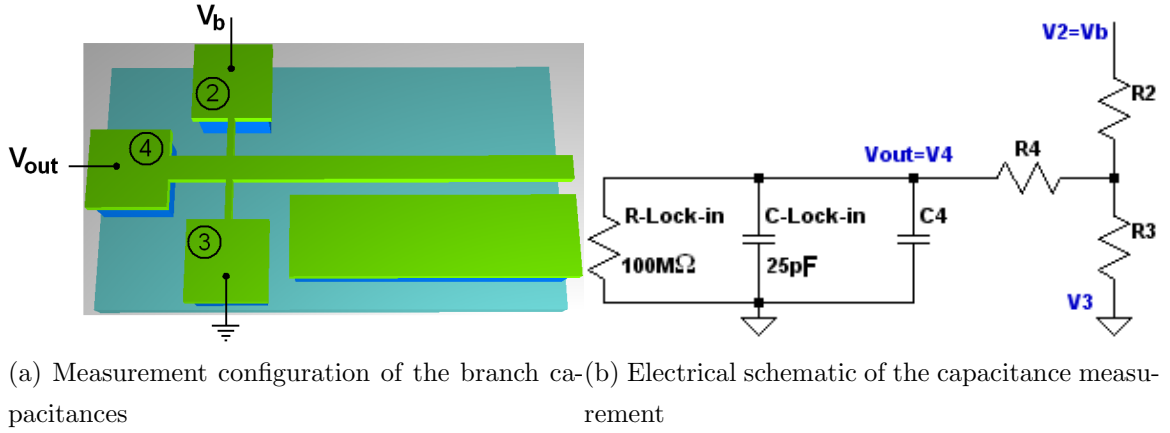
Fig. 3.7: Measurement configuration for the branch capacitances

This parameter is estimated by measuring experimentally the cut-off frequency. For biasing the device we used the lock-in internal source. An alternate signal has been applied to the NEMS, $V_b = 100mV_{rms}$ and its frequency was scanned from 0-2Mhz. The measured output voltage versus frequency is shown in figure 3.8. The curves ob-
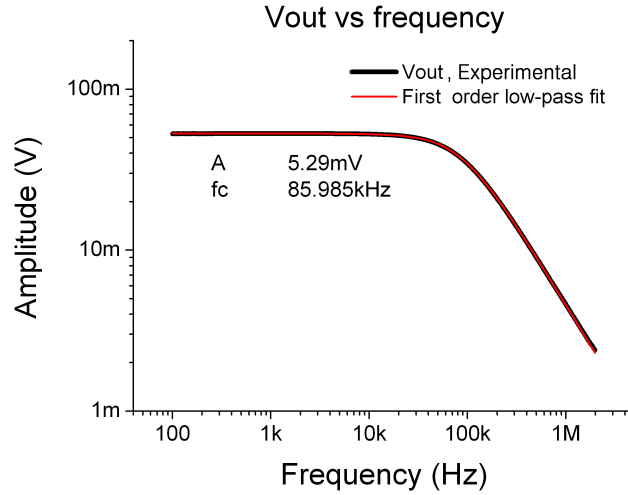
Fig. 3.8: The output voltage versus frequency, experimental measurements and first order low-pass fit

tained from measurement were fitted using a first order low-pass filter and the cut-off frequency was estimated. From equation (3.39) we can calculate the branch capacitance. For a frequency of 58kHz as estimated from the fitting we obtained a branch

resistance of $C_4 = 115.5pF$. The capacitance of the other branches was estimated the same way resulting in $C_2 = 113pF$ and $C_3 = 117pF$.

An electrical circuit model figure 3.9 was designed and simulated via SPICE using the resistance and capacitance values obtained experimentally. The response of the
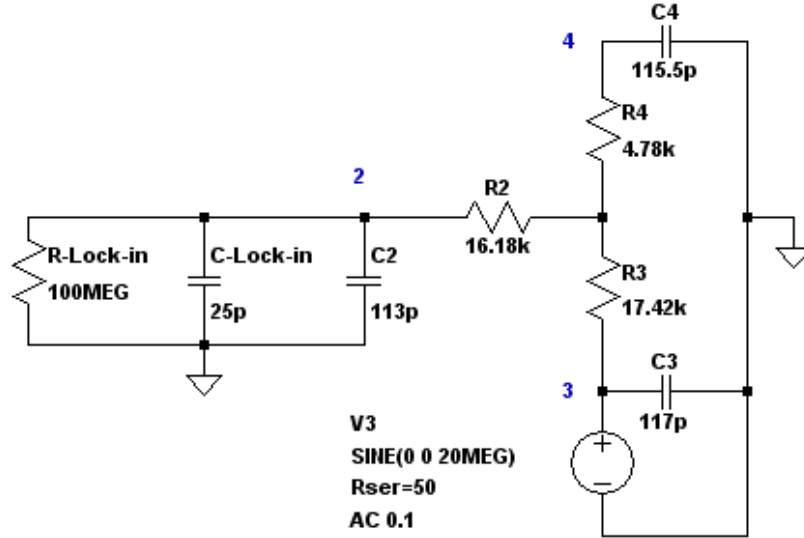
Fig. 3.9: The output voltage versus frequency

simulation fits perfectly to the experimentally ones, figure 3.10. These results confirmed that the electrical circuit modeled correctly the frequency behavior of the whole test-bench NEMS set. The important information we gained was the frequency range where measurements can be performed correctly. This intrinsic filter behavior attenuates significantly the signal at high frequencies and makes measurement almost impossible. The optimal range operation with no attenuation goes up to 100kHz varying with the devices resistance.

3.5 Overcoming high frequency signal attenuation through a downmixing detection technique

To avoid parasitic impedances and cross talking, we had to make measurements at low frequencies. This was achieved with a heterodyne down-mixing technique. The mixing technique consists in multiplying together two different signals $A_1 cos(\omega t)$ and
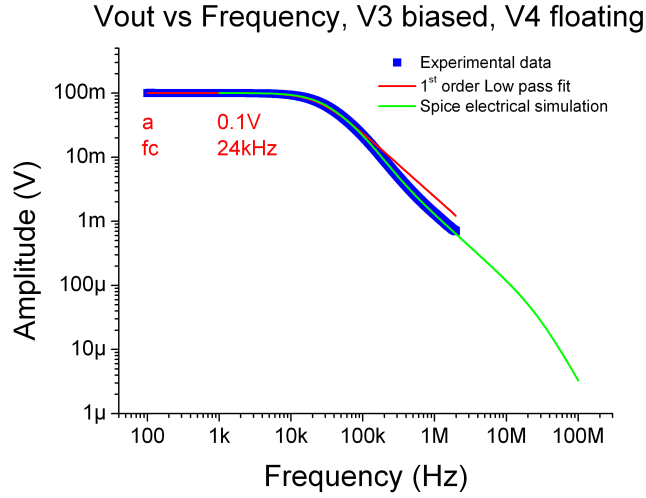
Fig. 3.10: The output voltage versus frequency

$A_2cos((\omega + \Delta\omega)t)$. The output signal will have an amplitude proportional to $\frac{A_1A_2}{2}$ and frequency components at low $\Delta\omega$ and high 2ω frequencies.

$$V_{out} \propto \frac{A_1A_2}{2}\left[cos(\Delta\omega t) + cos(2\omega t)\right] \quad (3.40)$$

In our case the piezoresistive gauges were used as signal mixers and allowed to read
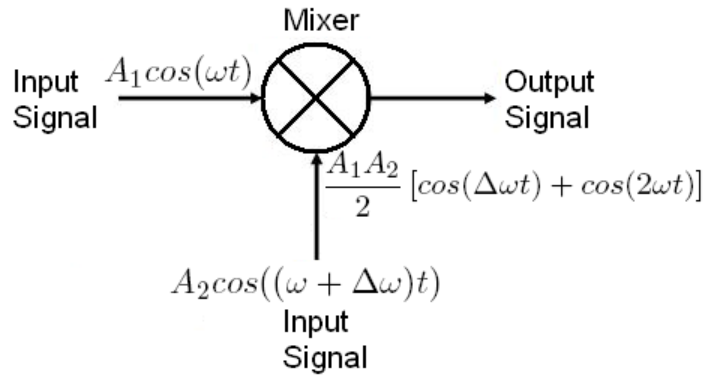
Fig. 3.11: The mixing technique

out the resistance variation at a lower frequency, (typically between 10 kHz and 30 kHz) [17]. When the lever beam is vibrating at a given frequency ω it will cause a resistance variation on the gauges with the same frequency, $\Delta R(\omega)$ (equation (3.36)). This variation can be measured by applying a bias voltage on the gauges. The current

flowing on this resistance will depend by the applied voltage V_b. Since $\Delta R << R$, we can approximate the current with a first order expression in ΔR.

$$I_b(t) = \frac{V_b(t)}{R + \Delta R cos(\omega t)} \approx \frac{V_b(t)}{R} - \frac{V_b(t) \cdot \Delta R cos(\omega t)}{R^2} \tag{3.41}$$

The relative resistance variation in piezoresistive gauges is of the order of $\Delta R/R = 10^{-3} - 10^{-4}$, with this assumption the second term of equation (3.41) is negligible compared to the first one. The voltage generated by the gauge is proportional to its resistance variation $\Delta R \cdot cos(\omega t)$ times the current flowing on it. According to the
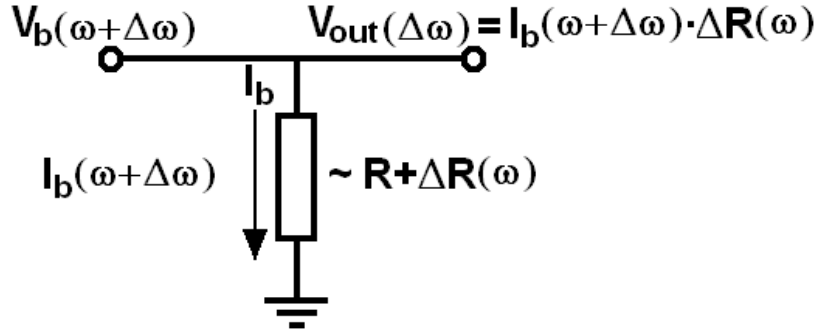
Fig. 3.12: Schematic of the piezoresistive gauge acting as a signal mixer.

mixing technique a low frequency component at $\Delta\omega$ can be obtained by applying a bias voltage of $V_b(\omega + \Delta\omega)$.

$$V_{out} = I_b(\omega + \Delta\omega) \cdot \Delta R(\omega) = \frac{1}{2}I_b \cdot \Delta R[cos(\Delta\omega) + cos(2\omega + \Delta\omega)] \tag{3.42}$$

The gauges acting as motion transducers and signal mixers allow to convert the motion into an electrical signal and to shift it at a lower frequency. The advantage of low frequency measurements is that we have bypassed the signal attenuation problem due to the parasitic impedances.

The bridge configuration

In the nano-electromechanical device the gauges are situated in a bridge configuration. We are interested in measuring the voltage at the center of the bridge, which has to be connected to the input of the Lock-in amplifier. An equivalent schematic modeling the electrical behavior of the setup is shown in figure 3.13. For simplification we have considered the case when $V_{b2} = 0$. A bias voltage $V_{b1}(t) = V_b cos((\omega + \Delta\omega)t)$
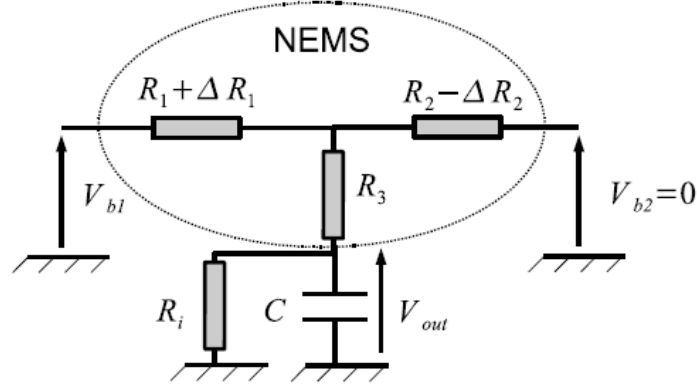
Fig. 3.13: Electrical schematic of the measurement

is applied on the first branch and the second one has been grounded. The LNA measures the voltage V_{out} at the output of the middle branch. This voltage is different from the one present at the bridge center, due to the current flowing on the branch R_3, which causes a potential drop. The input impedance of the lock-in consists of a $R_{in} = 100M\Omega$ impedance in parallel with a $C_{in} = 25pF$ capacitance. For an operation frequency of $10^8 rad/s$, characteristics of our devices, the impedance presented by the capacitance is about 200Ω. Under these conditions the parallel impedance R_{in} can be neglected. The strain on the gauges is modulated at a frequency ω by the cantilever. The strain modulations will induce resistance variations $R_1(t) = R_1 + \Delta R_1 cos(\omega t)$ and $R_2(t) = R_2 - \Delta R_2 cos(\omega t)$ at the same frequency. The resistance variation on the opposite side has opposite sign. This is due to the fact that they experience opposite strain. When the first experience a tensile strain the second will experience a compressive one resulting in opposite resistance variation. The output voltage at the lock-in has been evaluated using a linear differential equation.

$$V_{b1}(t) = R_1(t)\left(1 + \frac{R_3}{R_1(t)} + \frac{R_3}{R_2(t)}\right)C\frac{dV_{out}}{dt} + \left(1 + \frac{R_1(t)}{R_2(t)}\right)V_{out} \qquad (3.43)$$

For desribing the output voltage V_{out} we have used a perturbative approach :

$$V_{out} = V_o^{(0)} + V_o^{(1)} + ... \qquad (3.44)$$

where $V_o^{(0)}$ is of the order 0 in ΔR and $V_o^{(1)}$ of the first order. $V_o^{(0)}$ verifies the relationship :

$$\frac{R_2}{R_1 + R_2}V_{b1}(t) = \tau\frac{dV_o^{(0)}}{dt} + V_o^{(0)} \qquad (3.45)$$

and $V_o^{(1)}$ is defined by the following relationship :

$$
\begin{aligned}
\left(\frac{\Delta R_1(t)}{R_1} + \frac{R_3}{\alpha}\left(\frac{\Delta R_2(t)}{R_2^2} - \frac{\Delta R_1(t)}{R_1^2}\right)\right)\tau\frac{dV_o^{(0)}}{dt} - \frac{R_2\Delta R_1(t) + R_1\Delta R_2(t)}{R_2(R_1 + R_2)}V_o^{(0)} \\
= \tau\frac{dV_o^{(1)}}{dt} + V_o^{(1)}
\end{aligned}
$$

(3.46)

where $\alpha = \left(1 + \frac{R_3}{R_1} + \frac{R_3}{R_2}\right)$ and $\tau = \frac{R_1 R_2}{R_1 + R_2}\alpha C$.

The expression for the component of order 0 in ΔR at the frequency $\omega' = (\omega + \Delta\omega)$ results :

$$
V_{out}^{(0)} = \frac{R_2 V_b}{R_1 + R_2}\frac{cos(\omega' t - \varphi)}{\sqrt{1 + (\omega'\tau)^2}} \approx \frac{R_2 V_b}{R_1 + R_2}\frac{cos(\omega' t - \varphi)}{\omega'\tau}
$$

(3.47)

For $\omega' \approx 10^8 rad/s$, $\tau = 75 10^{-8}s$ et $\omega'\tau = 75$ ($R_1 \approx R_2 \approx R_3 \approx 10k\Omega$ et $C = 50pF$). Experimentally we couldn't observe this component with the spectrometer since it is filtered and attenuated by the system. We are interested in the component $V_o^{(1)}$, that carries the information related to the resistance variations. This term expressed in equation (3.49) produces two frequency components : one at $\Delta\omega$ an the other at $(2\omega + \Delta\omega)$ which is filtered by the system. The voltage term at low frequency results :

$$
\begin{aligned}
\frac{V_0^{(1)}}{V_b} &= +\frac{R_2}{R_1 + R_2}\left(\frac{\Delta R_1}{R_1} + \frac{R_3}{\alpha}\left(\frac{\Delta R_2}{R_2^2} - \frac{\Delta R_1}{R_1^2}\right)\right)\frac{\omega'\tau}{\sqrt{1 + (\omega'\tau)^2}}\frac{sin(\Delta\omega t + \varphi)}{2} \\
&- \frac{R_2\Delta R_1(t) + R_1\Delta R_2(t)}{(R_1 + R_2)^2}\frac{1}{\sqrt{1 + (\omega'\tau)^2}}\frac{cos(\Delta\omega t + \varphi)}{2}
\end{aligned}
$$

(3.48)

When the two bias voltage are applied simultaneously the output voltage becomes :

$$
\begin{aligned}
V_0^{(1)} &= +V_{b1}\frac{R_2}{R_1 + R_2}\left(\frac{\Delta R_1}{R_1} + \frac{R_3}{\alpha}\left(\frac{\Delta R_2}{R_2^2} - \frac{\Delta R_1}{R_1^2}\right)\right)\frac{\omega'\tau}{\sqrt{1 + (\omega'\tau)^2}}\frac{sin(\Delta\omega t + \varphi)}{2} \\
&- V_{b2}\frac{R_1}{R_1 + R_2}\left(\frac{\Delta R_2}{R_2} + \frac{R_3}{\alpha}\left(\frac{\Delta R_1}{R_1^2} - \frac{\Delta R_2}{R_2^2}\right)\right)\frac{\omega'\tau}{\sqrt{1 + (\omega'\tau)^2}}\frac{sin(\Delta\omega t + \varphi)}{2} \\
&- (V_{b1} - V_{b2})\frac{R_2\Delta R_1(t) + R_1\Delta R_2(t)}{(R_1 + R_2)^2}\frac{1}{\sqrt{1 + (\omega'\tau)^2}}\frac{cos(\Delta\omega t + \varphi)}{2}
\end{aligned}
$$

(3.49)

3.5.1 Electric schemes for piezoresistive motion detection

For measuring the component at low frequency we have to use an indirect lock-in synchronous method. According to equation (3.31) the cantilever can be actuated at a frequency ω or 2ω. Two alternative schematics can be employed for the measurement depending on the actuation method used :

1. The ω detection scheme with DC+AC actuation, figure 3.14

2. The 2ω detection scheme with AC actuation, figure 3.15
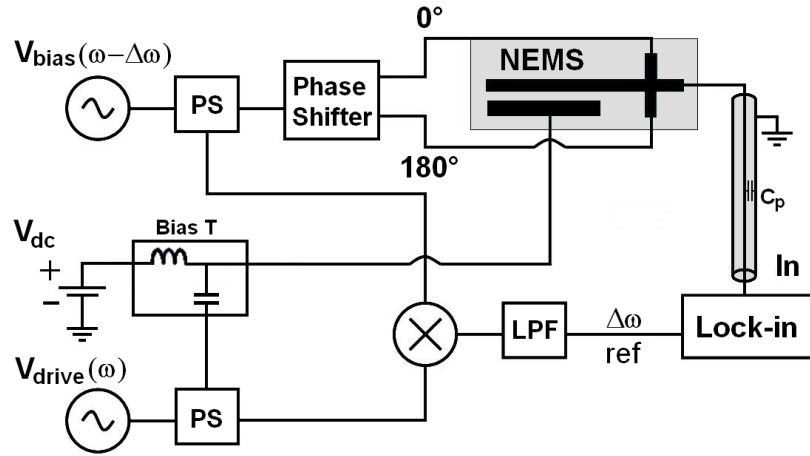
Fig. 3.14: Schematic of the experimental setup with $DC + AC$ actuation used for detecting the resonant motion of the NEMS. PS, LPF are power splitter and low-pass filter respectively.

The ω force component is proportional to $F(\omega) \propto V_{dc}V_{ac}\,cos(\omega t)$. The drive signal to actuate the lever consist of a static and alternate voltage $V_g = V_{dc} + V_{ac}cos(\omega t)$. It is applied to the actuation electrode using a bias T circuit. The electrostatic force $F(\omega)$ causes a resistance variation $\Delta R\,cos(\omega t)$, which is read by applying a bias voltage $V_b\,cos((\omega + \Delta\omega)t)$. The gauges are biased through a 180 phase shifter. The goal of the opposite voltages on the gauges is to obtain a nulled voltage at the bridge center, and reduced background. As we have previously explained only the component at low frequency $\Delta\omega$ can be measured by the lock-in, since the higher one $(2\omega - \Delta\omega)$ is filtered by the system. Another mixing between the drive and the bias signal has been generated externally in order to obtain the reference for the lock-in. The signals are obtained from the same source generators through power splitters assuring a correct synchronous measurement.
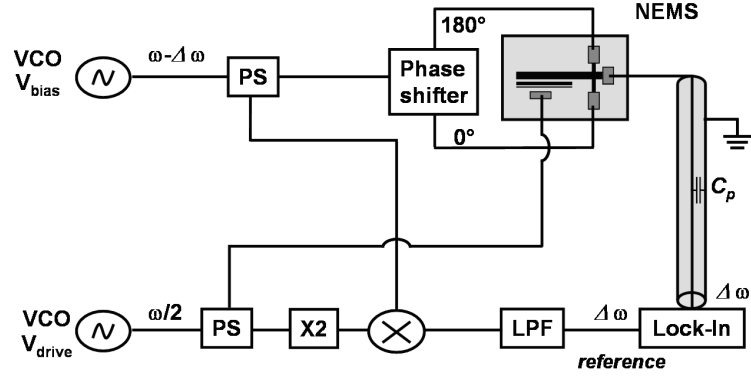
Fig. 3.15: Schematic of the experimental setup with $\omega/2$ actuation used for detecting the resonant motion of the NEMS. PS, LPF are power splitter and low-pass filter respectively.

In the second scheme, figure 3.15 the beam is actuated at a frequency ω with a drive voltage $V_d cos(\omega/2)$. Because the electrostatic force is proportional to $F = \frac{1}{2}CV_d^2$, the cantilever vibrates at the double frequency ω. It is called the 2ω technique since the cantilever oscillates at twice the frequency of the drive signal. For obtaining the $\Delta\omega$ reference the signal $V_b cos(\omega - \Delta\omega)$ has to be mixed with a signal at a frequency ω. Since the drive signal has a frequency of $\omega/2$ it is sent through a frequency doubler in order to achieve a correct reference. For implementing these schemes and testing our in-plane detection concept based on suspended piezoresistive gauges we had to develop a dedicated testbench.

3.6 Test-bench assembly for NEMS motion detection

For testing the NEMS devices we have manufactured a vacuum chamber with feed-through coaxial cables figure, 3.16. The coaxial cables used in our experiments had an SMA/SMB termination. For placing the NEMS into the vacuum chamber and interfacing it with the coaxial cables we have fabricated a dedicated RF printed circuit board (PCB). The PCB has SMA connectors in one side and RF cooper pads on the other. The SMA connectors can be connected with the SMA cables while the cooper pads to the NEMS leads. The NEMS has been placed in the center of the PCB and connected to the pads through wire bonding as shown in figure 3.17.

Fig. 3.16: The vacum chamber setup used for low pressure measurements
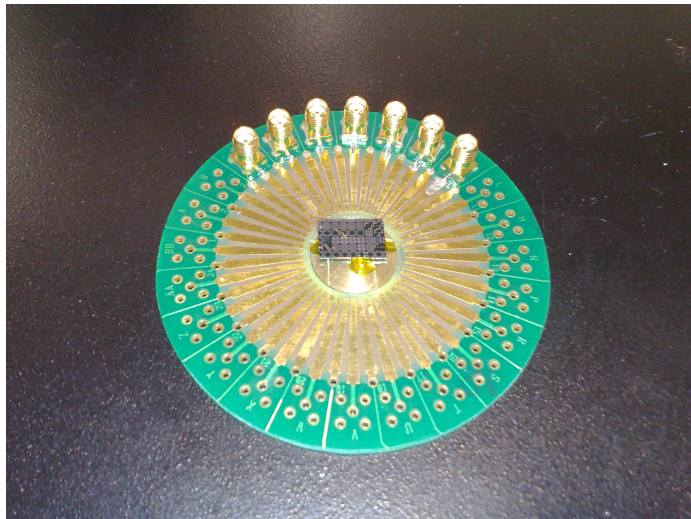
Fig. 3.17: Dedicated printed circuit board used for interconnections

The CALEO wedge bonding machine with gold wires of diameter $d = 80\mu m$ has been used for the bonding. All the pads have been short circuited before connecting the NEMS to the PCB in order to avoid any discharge that can destroy the device. The vacuum was achieved with a turbo pump connected directly to the chamber, figure 3.18.

The dedicated chamber has a small volume which permits to reach easily high vacuum levels. The coaxial cables have then been connected to the external electronics

Fig. 3.18: The Adixen turbo pump used for creating the vacuum into the chamber

for the test, figure 3.19. This setup allowed us to place and control the device into the chamber..
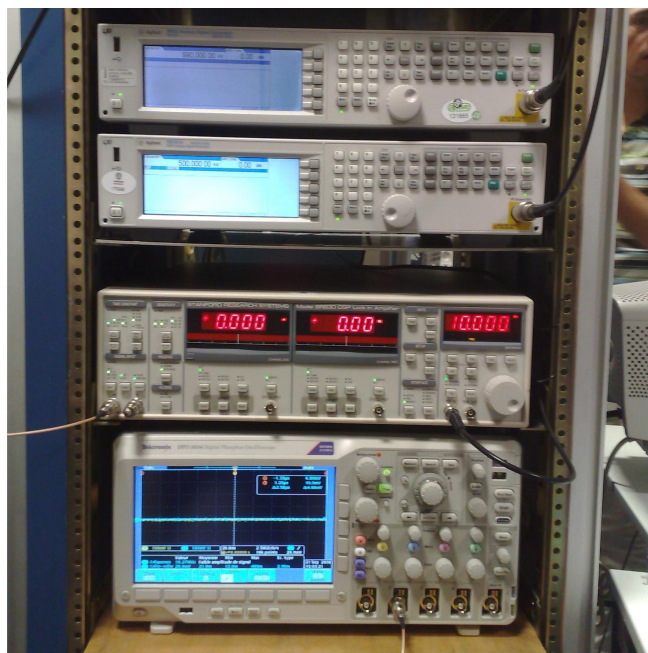
Fig. 3.19: Electronic equipments, employed for the experiment, Lock-in, source generators.

We have implemented an external electrical circuit, figure 3.20 following the schematic of figure 3.15. This circuit allowed to generate the lock-in reference, to bias

and drive the NEMS. The drive signal $V_d(\omega/2)$ is sent through a doubler before being mixed with the bias one $V_b(\omega + \Delta\omega)$. Since the output of the mixer is filtered through a low-pass filter only the $\Delta\omega$ component is sent to the lock-in which serves as the reference. The outputs of the 180 phase shifter bias the two gauges respectively, while the drive signal is sent to the actuation electrode. We have placed high pass filters before biasing and driving the NEMS in order to avoid low-frequency components that could be reflected from the mixing circuitry.
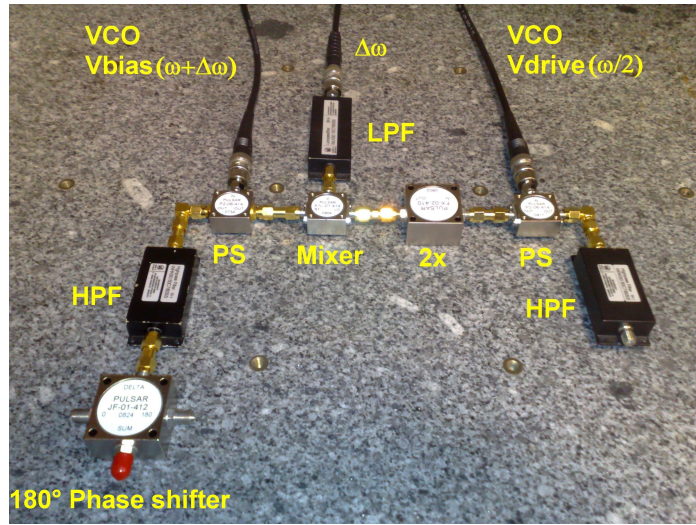
Fig. 3.20: Electronic equipments, employed for the experiment, Lock-in, source generators.

3.7 NEMS resistivity measurements

These experiments consist in measuring the resistances of the polarization and the read-out branches. The goal is to :

– Define the nature of the contacts and validate their Ohmic behaviour.
– Evaluate the resistivity of the leads, gauges and their doping concentration.
– Set the operation point ; test experimentally the gauge breaking point.

Each branch is composed by the connection leads (in green) plus the suspended gauges (in red) as shown in figure 3.21. The resistance of each branch is composed by the sum of the lead plus the gauge resistance, $R_b = R_l + R_g$. For measuring the device resistance two methods have been used : two point and four point measurement. In the two point measurement a bias voltage is imposed between the two branches
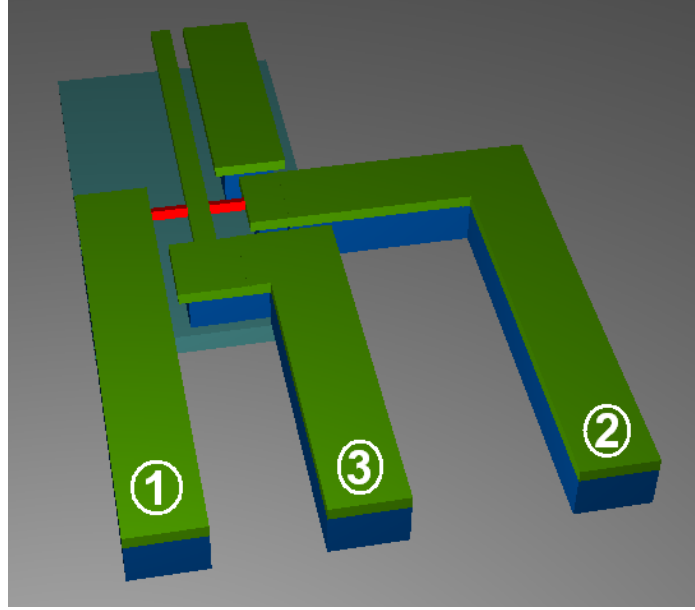
Fig. 3.21: layout of the branches composed by the connecting leads and the suspended gauges

and the flowing current is measured. We have used this technique to validate the Ohmic behaviour of the contacts. In figure 3.22 it is shown the V(I) curve behaviour measured between the branches 1 and 2. The experimental data were fitted to a linear curve which crosses the coordinate system at origin, validating its ohmic behaviour. The resistance R of a conductor of uniform cross section can be computed as $R = \rho \frac{l}{S}$, where l is the length of the conductor, S is the cross-sectional area and ρ is its electrical resistivity. By measuring the electrical resistance of the branches and through the layout design we can extract their resistivity as : $\rho = R \cdot \frac{S}{l}$. The two terminal resistance R_{12} has been measured on different devices in order to obtain a statistic distribution of their value. The resistivity and the doping are quite consistent from one device

	Resistance (Ω)	Resistivity $(\Omega \cdot cm)$	Doping (cm^{-3})
Mean value	15927	0.00698	$1.355 \cdot 10^{19}$
Standard error	441	0.00019	$4.66 \cdot 10^{17}$

Tab. 3.5: Resistivity and doping of the branches

to the other but the extracted doping $1.35 \cdot 10^{19}$ is smaller than the expected one $1.6 \cdot 10^{19}$. This process is well controlled and there is no reason for it to be smaller. We have thought to measure separately the resistance of each branch R_1, R_2 using a
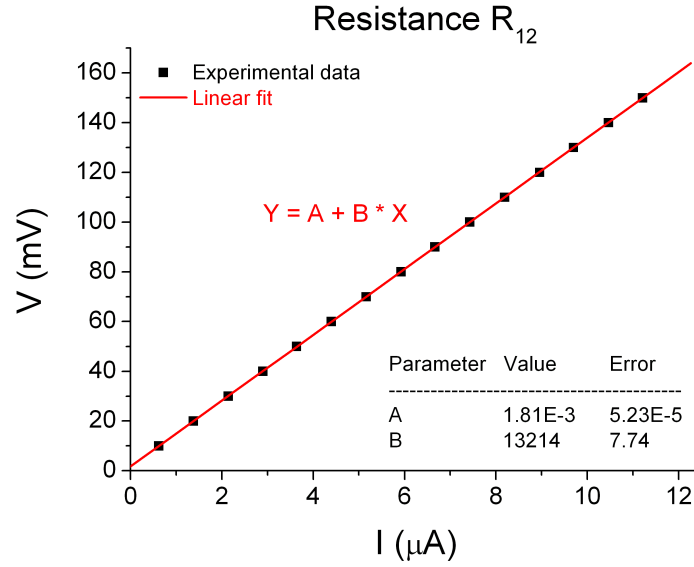
Fig. 3.22: V(I) curve obtained on the branch 1-2

four point measurement technique and evaluating their resistivity. The lengths of the pads connecting each gauge are different by design, which explains the variations of the resistances on each branch. We have observed a systematic resistivity variation between the left and the right branches. Given that the wafer is doped the same way through a homogeneous process, the resistivity of the leads should be the same over the sample and there is no reason for it to be different. How can be explained then such variations ? A possible explication to this problem is that the gauges are presenting a different resistivity from the leads even if they are doped the same way. Since each branch is composed by the lead and the gauge part, the evaluated resistivity is the average of both parts. Indeed in the branches with shorter leads we have obtained a higher resistivity than in branches with longer ones, suggesting a higher resistivity for the gauges. Under this assumption we have evaluated a resistivity for the leads and one for the gauges. The resistance of each branch is given as $R = R_l + Rg = \rho_l \frac{l_l}{S_l} + \rho_g \frac{l_g}{S_g}$. By measuring the resistance of each branch (R_1, R_2) and solving the following system :

$$R_1 = \rho_l \frac{l_{l1}}{S_{l1}} + \rho_g \frac{l_{g1}}{S_{g1}}$$

$$R_2 = \rho_l \frac{l_{l2}}{S_{l2}} + \rho_g \frac{l_{g2}}{S_{g2}} \tag{3.50a}$$

we have obtained the gauge and the lead resistivity table 3.6. From this data the

	Resistivity leads $(\Omega \cdot cm)$	Resistivity gauges $(\Omega \cdot cm)$	Doping leads (cm^{-3})	Effective doping gauges (cm^{-3})
Mean value	$6.122 \cdot 10^{-3}$	$8.041 \cdot 10^{-3}$	$1.6 \cdot 10^{19}$	$1.12 \cdot 10^{19}$
Standard error	$4.373 \cdot 10^{-4}$	$5.038 \cdot 10^{-4}$	$1.563 \cdot 10^{18}$	$9.246 \cdot 10^{17}$

Tab. 3.6: Resistivity of the leads and gauges

doping of the leads results $1.6 \cdot 10^{19}$ which is what we were expecting. How is it explained that the resistivity of the nano-gauges is higher than that of the bulk? The increase in resistivity has already been observed in doped semiconductors of similar dimensions such as silicon nanowires [52]. This could be due to surface depletion which will reduce the electrically active cross section of the wire resulting in a higher resistivity.

3.7.1 Resistance measurements through a local AFM technique

Another AFM technique for measuring locally the resistivity of the leads has been implemented. There are two possible methods using the AFM for resistance measurements. The first one consists on making a four point probe measurement. A potential is applied to the first lead with the second grounded and the AFM tip is used in contact mode to probe locally the potential drop figure.

The voltage measured by the AFM probe is proportional to :

$$V_p = \frac{V_1}{R_{l2}} R(x) \tag{3.51}$$

The AFM probe is scanned through the resistive lead for a length ΔL in the direction parallel to the electric field. The potential variation is proportional to the resistance

(a) AFM four point probe resistivity measurement (b) Electrical equivalence of the measurement setup
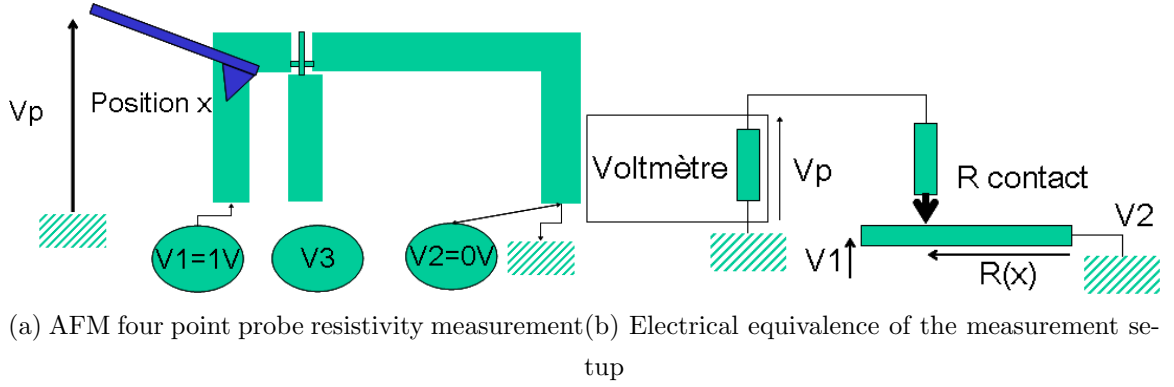
Fig. 3.23: schematic of the AFM resistance measurement setup

(a) (b)
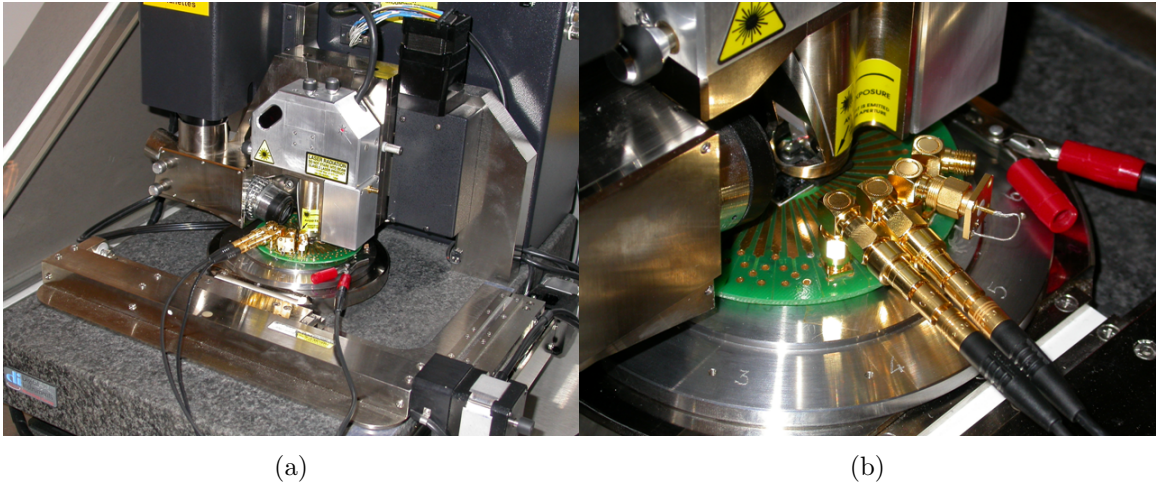
Fig. 3.24: AFM resistance measurement setup

variation along the length ΔL, where $\Delta R = R_{l2}\frac{\Delta V_p}{V_1}$. The resistivity is then estimated as $\rho = \frac{\Delta R}{\Delta L}S$, where S is the cross-sectional area of the leads $S = 10\mu m \cdot 0.16\mu m$.

The second method consists on biasing one of the leads and grounding the other. The AFM is then used in the KFM mode for imaging the potential gradient. The resistivity is evaluated the same way as in the previous technique $\rho = \frac{\Delta R}{\Delta L}S$. The resistivity of the leads obtained with this technique is $6.61 \cdot 10^{-3}\Omega \cdot cm$ resulting in a doping of $1.45 \cdot 10^{19}cm^{-3}$. For reducing the uncertainty with this technique we have to scan slowly along the field direction and for longer distances.
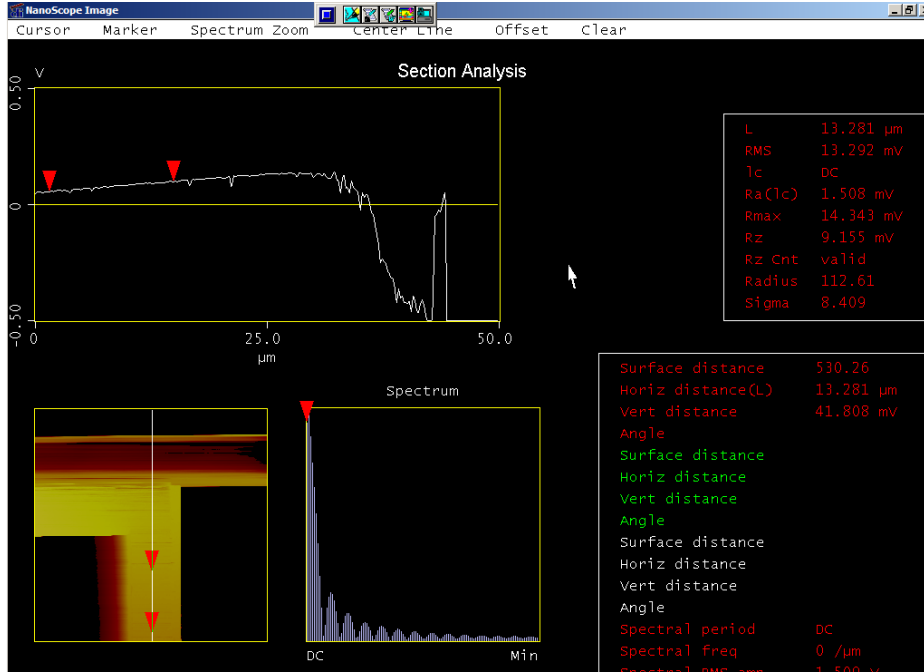
Fig. 3.25: resistivity measurements using the KFM method

3.7.2 Maximal current density

The bias current flowing on the gauges generates heat due to the Joule effect. The power dissipated per unit volume goes up to $p = \rho j^2$, where j is the current density.

$$j = \frac{I}{t \cdot w_j} \tag{3.52}$$

For $t = 160nm$ and $w_j = 80nm$, the current density for a current of $1\mu A$ is estimated to be $78 \cdot 10^6 A/m^2$. For estimating the order of magnitude of the elevation of temperature we have adopted a simplified model of the heat conduction in a 1 dimensional rod of length l. The temperature at its extremities is assumed to be $(T = T_0)$. The temperature profile is described by the following equation :

$$c\frac{\partial T}{\partial t} = \kappa\frac{\partial^2 T}{\partial x^2} + \rho j^2 \tag{3.53}$$

For the silicon we have :

-the thermal conductivity coefficient is $\kappa = 148W \cdot m^{-1} \cdot K^{-1}$,

-the Specific heat capacity $c = 1.631 \cdot 10^6 J/m^3/K$,

-the resistivity which depends on the doping.

In an established equilibrium, the temperature profile is parabolic with a maxima at the centre. The maximal temperature is given by :

$$\Delta T = \frac{\rho}{\kappa} l^2 j^2 \tag{3.54}$$

The characteristic length that can be considered in this problem is around $1\mu m$. If we consider a resistivity of $10^{-4} \Omega \cdot cm$, we would have and increase of $\Delta T = 0.5K$ for $I = 10\mu A$. The temperature variation depends strongly on the length of the rod and goes up as l^2. This estimation is quite critical , since if l is 10 times larger, then ΔT would be 100 times more important. Experiments were performed to define
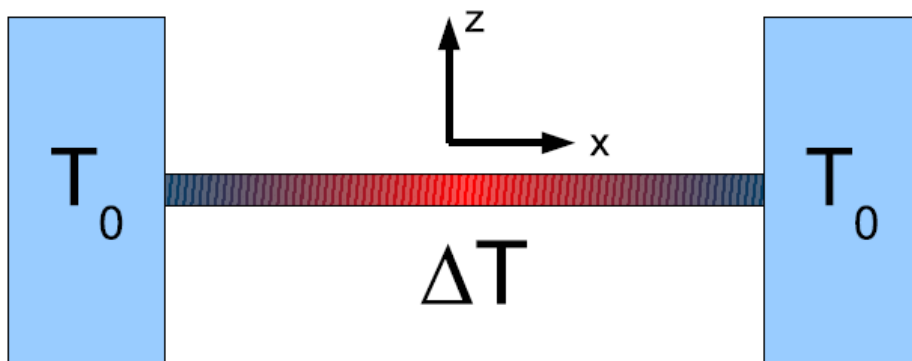
Fig. 3.26: 1-dimensional heat model for the strain gauges

the maximal current density supported by the gauges. The device was placed in a two point measurement seup. A DC poential was applied on the gauges and the current was monitored. The potential has been increased slightly until the gauges were broken. The device resistance before breaking was $17k\Omega$ and the breaking happened at $V_{dc} = 9.8V$ with a current of $I = 520\mu A$. The maximal current density supported by the gauges as evaluated from this data is $j = 3.25 \cdot 10^8 A/m^2$. From the electrical tests only one of the gauges was broken and the other parts remained intact. The device was observed with a SEM in order to verify the gauge breaking.

3.8 Experimental results of piezoresistive nanowire motion transduction

Different measurements were performed on the devices as a function of the bias and drive voltage. The cantilever displacement depends on the applied electrostatic
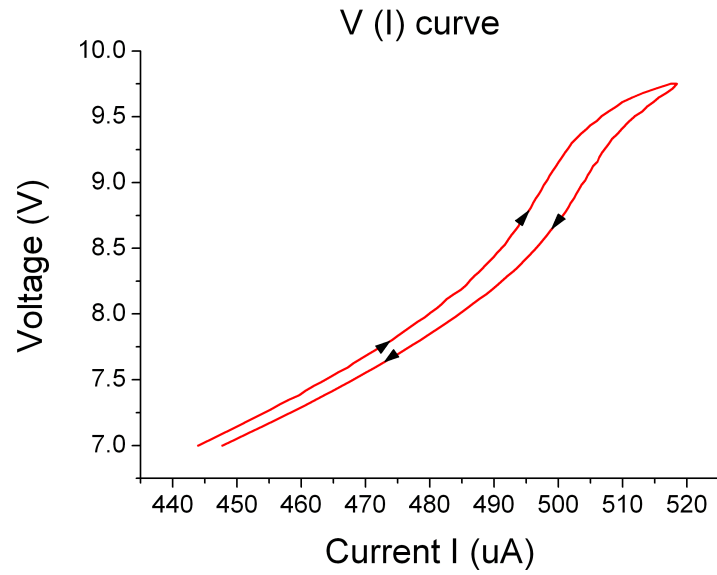
Fig. 3.27: I/V curves before gauge breaking

(a)   (b)
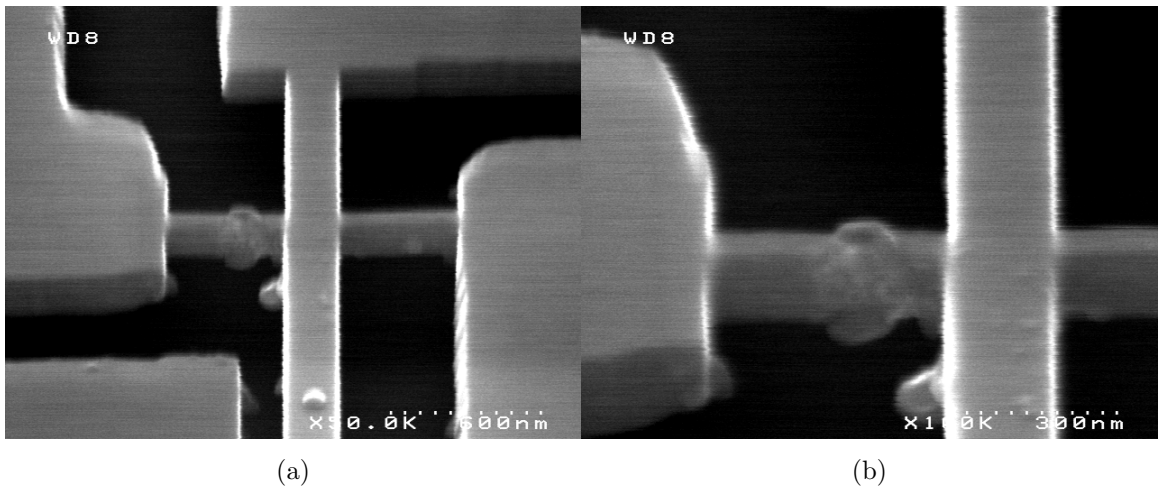
Fig. 3.28: SEM images after gauge breaking

force which is proportional to $F = C'[V_d \cdot cos(\omega t)]^2/2$. This force will have an AC $F_{AC}(\omega)$ and a static F_{DC} component proportional to V_d^2. The first will have a direct consequence on the displacement amplitude while the latter affects the lever stiffness thus changing the resonance frequency. This is confirmed by the experimental results where the resonance signal amplitude and frequency show a quadratic behaviour with

V_d (see Fig. 3.29 and 3.30).
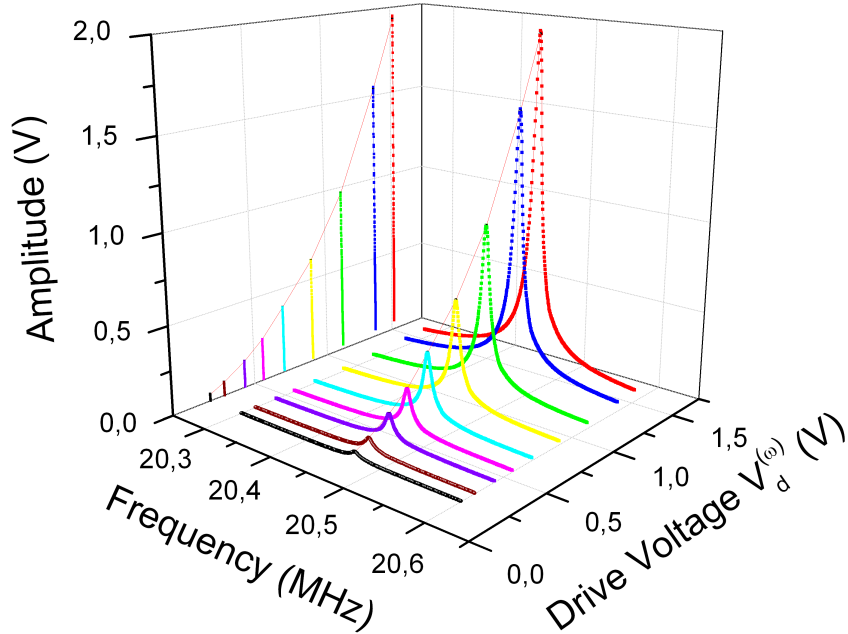
Fig. 3.29: Quadratic behaviour of the signal amplitude with the drive voltage V_d
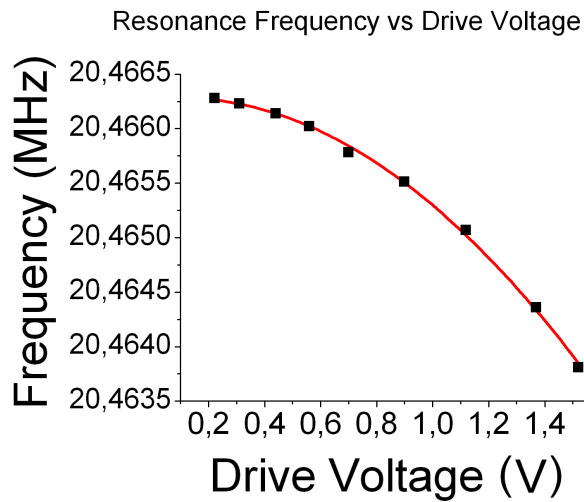
Fig. 3.30: Quadratic behaviour of the resonance frequency with the drive voltage V_d

The measured output signal is plotted as a function of the bias voltage. In figure 3.31 we show the measured linear behaviour as expected from equation (3.49). The NEMS devices are very robust and able to support elevated electrical bias and drive
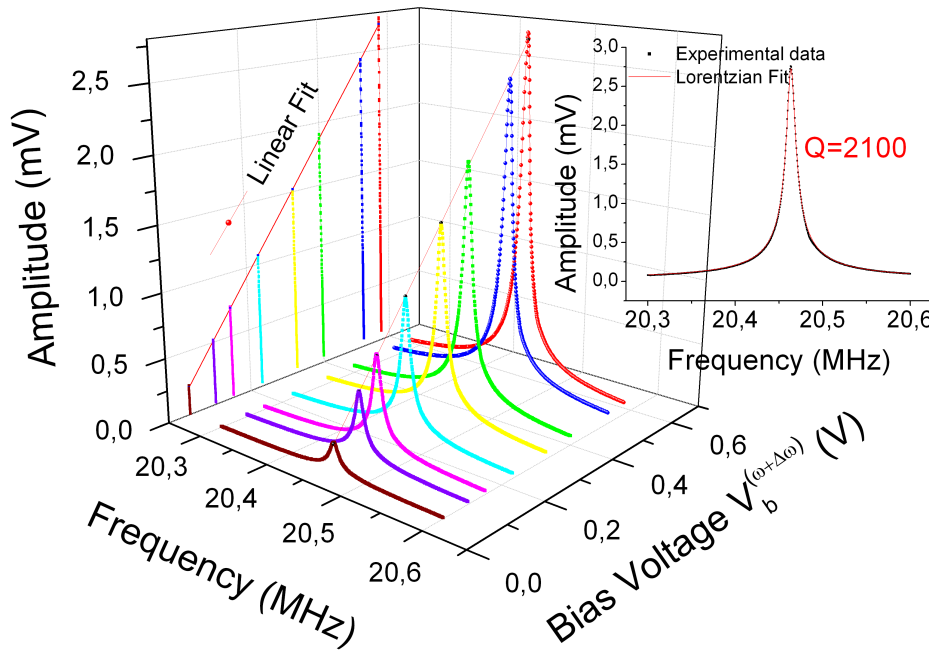
Fig. 3.31: Linear behaviour of the signal amplitude with the bias voltage V_b

signals going up to several volts. For co-integration of NEMS with CMOS (surroun-
ding electronics), it is desirable to work with comparable signal levels. The detection
scheme shows remarkable transduction efficiency with a huge peak to peak output
voltage of 3mV generated directly from the nano-mechanical motion without any ex-
ternal amplification. This huge built-in transduction gain makes possible to obtain a
self-sustaining resonator and regenerate the signal with just a transistor of moderate
gain [20].

Chapitre 4

Mass sensing with NEMS through resonance frequency shift

Mass sensing with electromechanical systems is usually performed by precisely determining the resonance frequency of the resonator and then by looking for a frequency shift as a result of the added mass. The relationship between the resonance frequency ω_0 and the effective mass M_{eff}, for the one-dimensional harmonic oscillator with effective spring constant k_{eff} is given by $\omega_0^2 = k_{eff}/M_{eff}$. Assuming that $\delta M << M_{eff}$ we can linearize the expression for the mass sensitivity.

$$\delta M \approx \frac{\partial M_{eff}}{\partial \omega_0} \delta \omega_0 = R^{-1} \delta \omega_0 \tag{4.1}$$

The sensitivity, otherwise called the minimum detectable mass δM depends on the minimum measurable frequency shift $\delta \omega_0$ and the inverse mass responsivity R^{-1}. Assuming that the spring constant k_{eff} of the mode which depends on the beam elastic properties and geometry remains unaffected we can estimate the responsivity expression.

$$R = \frac{\partial \omega_0}{\partial M_{eff}} = -\frac{\omega_0}{2 M_{eff}} \tag{4.2}$$

From equation (4.1) and (4.2) the sensitivity of the mass sensor resonator reults :

$$\delta M \approx -2 \frac{M_{eff}}{\omega_0} \delta \omega_0 \tag{4.3}$$

As it can be observed from equation (4.3) for frequency-shift mass sensing applications the limit of sensitivity is imposed by the frequency fluctuations $\delta \omega_0$. What is

the minimum detectable frequency shift $\delta\omega_0$ we are able to resolve in a noisy system and which are the main noise sources affecting this resolution ? There are at least three main noise sources affecting the frequency fluctuations and the mass sensitivity of the system : (1) thermal vibrations of the cantilever, (2) noise in the transducer, (3) noise generated by the amplifier and other electronics. The minimum detectable frequency shift can be estimated by integrating the spectral density of the frequency fluctuations $S_\omega(\omega)$ over the effective measurement bandwidth Δf :

$$\delta\omega_0 \approx \left[\int_{\omega_0 - \pi\Delta f}^{\omega_0 + \pi\Delta f} S_\omega(\omega) d\omega \right]^{1/2} \tag{4.4}$$

The $S_\omega(\omega)$ is expressed in units of $(rad/s)^2$. Considering a low noise displacement transducer, the ultimate mass sensitivity will be limited by the thermomechanical noise of the cantilever beam.

4.1 Thermomechanical noise sensitivity analysis

Here we will analyze the mass sensitivity limited by the thermomechanical noise. These fluctuations are a result of the thermally driven random motion of the cantilever beam. Considering the one-dimensional harmonic oscillator with resonance frequency ω_0, effective mass M_{eff} and effective spring constant $K_{eff} = M_{eff}\omega_0^2$, the mean square displacement fluctuations of the cantilever end $< x_{th} >$ satisfies the equipartition energy relationship [53] $1/2 k_{eff} <x_{th}^2> = 1/2 k_b T$. where k_b is the Boltzman constant and T the temperature. The spectral density of the random displacements $S_x(\omega)$ in units of m^2/Hz is given by :

$$S_x(\omega) = \left| G(\omega)^2 \right| S_F(\omega) = \frac{1/M_{eff}^2}{(\omega^2 - \omega_0^2)^2 + \omega^2\omega_0^2/Q} \frac{4M_{eff}\omega_0 k_b T}{Q} \tag{4.5}$$

where $|G(\omega)|^2$ is the response function of the damped harmonic oscillator and $S_F(\omega) = 4M_{eff}\omega_0 k_b T/Q$ is the thermomechanical force spectral density (in units N^2/Hz) with a white spectrum [53]. In the sensor configuration a digital phase locked loop (PLL) is used to read the frequency variations while the beam is driven at resonance by the voltage controlled oscillator (VCO). In order to take advantage of the full dynamic range the beam is driven up to the maximum of linearity with constant mean square amplitude $< x_c >$. The energy delivered to the NEMS beam

represents the maximum drive energy and is equal to $E_c = M_{eff}\omega_0^2 < x_c^2 >$. Thermal displacement fluctuations will add in turn frequency fluctuations with an effective white spectral density given by [54]

$$S_\omega(\omega) = \frac{S_\phi(\omega)}{(\partial\phi/\partial\omega)^2} \approx \left(\frac{\omega_0}{2Q}\right)^2 \frac{S_x(\omega)}{< x_c^2 >} = \frac{\omega_0^5}{Q^3}\frac{k_bT}{E_c}\frac{1}{(\omega^2 - \omega_0^2)^2 + \omega^2\omega_0^2/Q} \qquad (4.6)$$

$S_\phi(\omega) = S_x(\omega)/ < x_c^2 >$ gives the spectral density of phase fluctuations with units dB/Hz. By substituting equation (4.6) into equation (4.4) and integrating equation for $Q \gg 1$ and $2\pi\Delta f \ll \omega_0/Q$ we obtain $\delta\omega_0$:

$$\delta\omega_0 \approx \left[\frac{k_bT}{E_c}\frac{\omega_0\Delta f}{Q}\right]^{1/2} \qquad (4.7)$$

Substituting the expression obtained for $\delta\omega_0$ into equation (4.3) we get :

$$\delta M \approx 2M_{eff}\left(\frac{E_{th}}{E_c}\right)^{1/2}\left(\frac{\Delta f}{Q\omega_0}\right)^{1/2} \qquad (4.8)$$

The ratio E_c/E_{th} represent the signal to noise power ratio (SNR) and the effective dynamic range. The dynamic range is commonly expressed in decibels where $DR = 10log(E_c/k_bT)$. A compact expression in terms of the effective mass M_{eff}, the resonance frequency ω_0, the quality factor Q, the responsivity R and of the effective dynamic range ΔR is given in equation (4.9)

$$\delta M \approx 2M_{eff}\left(\frac{\Delta f}{Q \cdot \omega_0}\right)^{1/2} \cdot 10^{-DR/20} \approx \frac{1}{R}\left(\Delta f\frac{\omega_0}{Q}\right)^{1/2} \cdot 10^{-DR/20} \qquad (4.9)$$

4.2 Key parameters for optimizing inertial mass sensors

The expression in equation (4.9) gives important indications on the parameters affecting the mass sensitivity of a NEMS resonator. These parameters can be tuned in order to achieve ultrasensitive mass detection. The sensitivity depends proportionally on the effective mass M_{eff} and the measurement bandwidth Δf, while it is inversely proportional to the responsivity R, quality factor Q, the resonance frequency ω_0 and the dynamic range ΔR. For decreasing the minimum detectable mass we have therefore to minimize M_{eff} and Δf and to maximize Q, ω_0 and ΔR. The potential

of the device size miniaturization for mass sensing shows up on the systems mass reduction which scales down as L^3. The devices we have fabricated have active masses on the order of $M_{eff} \approx 100 fg$. Smaller active masses can be achieved with nanowires or carbon nanotubes order of $10^{-18} g$ which have enabled atomic resolution mass sensing [1]. The smallest measurement bandwidth is required for filtering-out the noise, but it would deteriorate the response time. The minimum bandwidth we can use depends from the time response requirements for the system. High Quality factors are required for two reasons first for improving the sensitivity and second for lowering the resonator power consumption. If we consider the resonator as a lossy energy storage device, the energy delivered to it is dissipated in a time $t = Q/\omega_0$, which is the ring time of the oscillator. The minimum operation energy is defined as the energy which will drive the resonator at amplitudes comparable to those of thermal fluctuations. Considering the energy $E_{th} = K_b T$ of thermal fluctuations for a given mode, the minimum input power can be estimated as :

$$P_{min} = k_b T \omega_0 / Q \qquad (4.10)$$

For our NEMS devices with $20 Mhz$ resonance frequency and quality factor of $Q = 5000$ the minimum power required is P_{min} $2.6 nW$. Even if we multiply this power by a factor of 1000 in order to get high signal to noise ratios the power levels will remain in the μW range. The effect that the resonance frequency has on the sensitivity is more complicated. From the sensitivity expression it looks like higher resonance frequencies will result in increased responsivity of the system and smaller detectable masses. High frequency devices are achieved with low aspect ratios l/t or l/w. Low aspect ratio geometries yield high force constants, which would affect the dynamic range. The device geometry has to be tailored in order to find the optimal trade-off between high responsivity (high resonance frequency) devices and large dynamic ranges. The dynamic range DR for a NEMS device is defined as the ratio of its maximum displacement amplitude(at the onset of nonlienarity) to its rms displacement noise floor within the operation bandwidth Δf. The bottom of the dynamic range is defined by the thermomechanical induced displacement while the upper limit is defined by the onset of nonlinearities [51]. For maximizing the dynamic range of the sensor we should be able to reach its upper and lower limits. First, the largest *rms* drive level has to be applied to the resonator while producing a linear response and second ultrasensitive transducers limited only by the thermomechanical noise should

be employed for reading the resonator motion.

4.3 Mass sensitivity and its dependance on the geometrical paramteres

In section 4.1 we analyzed the ultimate mass sensitivity limited by the thermo-mechanical noise which depends on the effective mass M_{eff}, resonance frequency ω_0, bandwidth Δf, dynamic range ΔR and quality factor Q. How do these parameters change with scale reduction and how do they affect the mass sensitivity of a NEMS resonator? We will consider a beam resonator (clamped-clamped or fixed-free) with Young's modulus E, mass densitiy ρ, length L, thickness t and beam width w. The effective mass M_{eff} of the resonators depends on the material density ρ and its geometrical dimensions L, t and w, where $M_{eff} \approx \rho L t w$. For a clamped-clamped or fixed-free beam the resonance frequency was shown in Eq. (2.5) to be inversely proportional to the length of the beam $\omega_n = \frac{(k_n)^2}{2\sqrt{3}} \frac{t}{L^2} \sqrt{\frac{E}{\rho}}$, where k_n is the mode value of the $n - th$ mode. The dynamic range is given as the ratio of the maximum drive energy $E_c = M_{eff}\omega_0^2 a_c^2/2$ to the thermal energy $E_{th} = k_B T/2$, where a_c is the critical amplitude. For a doubly clamped beam $a_c = 1.685t/\sqrt{Q}$ [55] and for a fixed-free beam $a_c = 6.3L/\sqrt{Q}$[56]. By substituting the expressions of M_{eff}, ω_0, E_c, E_{th} and a_c into equation (4.8), the resonator mass sensitivity as a function its geometrical parameters is obtained. In the case of a doubly clamped beam the sensitivity is given by the relationship in equation (4.11a) and for a fxed-free beam by equation (4.11b) :

$$\delta M_{fixed-fixed} \propto c_1 \sqrt{k_B T \Delta f \sqrt{\frac{\rho^5}{E^3}} \frac{\sqrt{L^7 \cdot w}}{t^2}} \propto l^2 \qquad (4.11a)$$

$$\delta M_{fixed-free} \propto c_2 \sqrt{k_B T \Delta f \sqrt{\frac{\rho^5}{E^3}} \sqrt{\frac{L^5 \cdot w}{t}}} \propto l^2 \qquad (4.11b)$$

where c_1 and c_2 are numerical constants. As it can be observed reducing the size of the devices by one order of magnitude will result in an overall sensitivity improvement of two orders of magnitude. Since the mass sensitivity is proportional to the beam length L and inversely proportional to the beam thickness t, low aspect ratio devices would provide a better sensitivity. The resonance frequency $\omega_0 \propto t/L^2$ and the

beam stiffness $k \propto t^3/L^3$ are inversely proportional to the aspect ratio. This means that low aspect ratio devices are characterized by high resonance frequencies and increased beam stiffness. The resonator material properties also affect the sensitivity which is proportional to $\rho^{5/4}$ and inversely proportional to $E^{3/4}$, suggesting the use of low density materials with increased mechanical properties. Lighter and stronger materials with nanoscale dimensions and low aspect ratios would provide yoctogram sensitivities [1], [57]. How can such devices be realized nowadays? Despite the advances on scale reduction it is difficult to obtain nanometric size devices with the existing top-down fabrication techniques. However bottom-up techniques [58] have shown to obtain geometries with nanoscale dimensions. These geometries such as nanowires and carbon nanotubes are usually synthesized with chemical CVD processes. They present perfectly terminated structures with low mass density and the highest Young's modulues which makes these structure ideal components for ultra-sensitive mass sensors.

4.4 Experimental results

The experiments[59], performed at room temperature and pressure of less than 1 mTorr, showed a remarkably small and flat background, as shown in fifure 4.1. The measured quality factor was approximately 5000 in vacuum and 200 at atmospheric pressure. Quality factors up to 10000 were measured. The transduction efficiency is usually characterized by the signal to background ratio (SBR) and the signal to noise ratio (SNR). The SBR is the ratio between the useful signal and the background that comes from coupling between the NEMS and the environment. For instance, parasitic capacitance could couple the driving signal with the output. Any noise or drift of these external elements would also be additional noise sources that superimpose to the NEMS noises. The SNR is the ratio between the useful signal and their random variations at the resonance frequency. The resolution is directly deduced from the SNR considering the measurement bandwidth.

4.4.1 Signal to background ratio

We have proved that the geometrical and frequency decoupling between the actuation and detection results in a very large signal to background ratio (SBR) of 67dB. For ultra low mass sensing, SBR is an important parameter that has to be maximized. At the resonance, a large SBR means large variation of the phase for a small frequency shift (Bode representation). In a closed loop (phase locked loop for instance) the digital error on the readout of the phase will be then low with devices having a large SBR. Furthermore device with large background will be more sensitive to the random perturbations of its environment. This value is close to two orders of magnitude larger than previous SBR [48],[60],[61] at ambient temperature (300K). Four reasons to this large SBR can be mentioned. First actuation and detection are well decoupled because they are based on two different techniques. The intrinsic bridge configuration removes the background and improves the SBR of a factor 5 at least. The lever arm is a cantilever and the non linear regime is reached only for large displacements around 100 nm (compared to double clamped beam). The electrical actuation can be then quite large around 1.5V. Finally, the downmixing techniques that do not depend on the NEMS also improve the SBR by decreasing the background. Average value per wafer of resonant frequency is 19.16 MHz with a maximum dispersion of 2% showing the pretty good reproducibly of the VLSI process. V_{drive} can be set between a few hundred millivolts to 5 volts before having non linear behavior of the cantilever. V_{bias} can be set up to 10 V before gauge melting. In the experiment, the voltages are set to a value of 1.5V, which corresponds to the maximum supplied by our AC-generator.

4.4.2 Transducer efficiency and thermomechanical noise measurements

Our objective was that of scaling the size down to the nanoscale while maintaining an efficient transduction system. These has been been achieved with in-plane piezoresistive nanowire strain transducers. Thermomechanical noise measurement were performed in order to validate the transduction efficiency for ultimate motion detection. High transduction gain is necessary for overcoming external noise sources such as those coming from the electronics and being limited only by the intrinsic thermomechanical noise of the resonator. We have shown that the detection technique employed in our
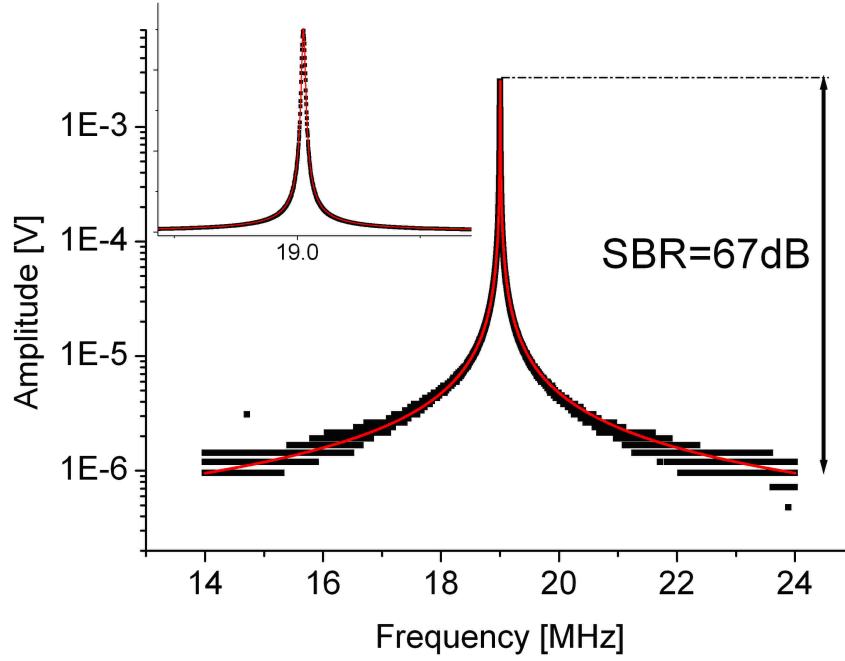
Fig. 4.1: Typical output signal from the structure shown in Fig. 1 in a vacuum with pressure under 1 mTorr. The signal to background ratio is 67 dB for $V_{drive} = 1.5V$ and $V_{bias} = 1.5V$ - Sampling time=30 ms. The inset shows the same data using linear scale. The maximum voltage (3mV) corresponds to a displacement of the cantilever end of 10 nm (still largely below the non linear regime).

experiments is highly efficient and able to resolve the thermomechanical motion of the nanoresonator. The thermomechanical noise peak detection uses the same principle shown by Bargatin et al [45]. There is no external drive and only a bias voltage V_b is applied to the gauges, the measurement configuration is shown in figure 4.2. We swept
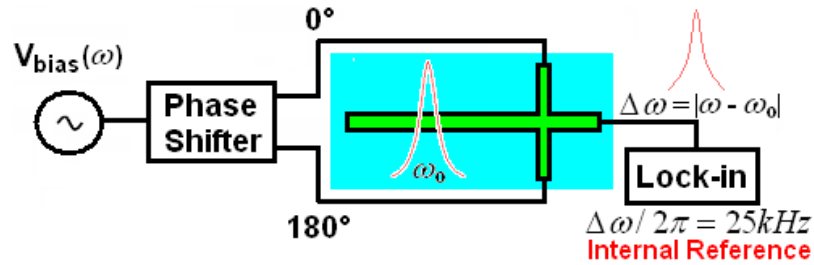
Fig. 4.2: Thermomechanical noise measurements configuration

the bias frequency ω_{bias} toward the fundamental resonance frequency of the resonator

ω_0 and measured the output noise ($V/\sqrt{Hz}$) with the lock-in at an offset frequency of $\Delta\omega/2\pi = 25kHz$. While approaching the resonance the noise fluctuations increase resulting on a resonance peak. The high frequency thermo-mechanical noise is shifted to a lower frequency $\Delta\omega = |\omega_{bias} - \omega_0|$ due to the down-mixing principle. Since the reference is set at a frequency $\Delta\omega/2\pi = 25kHz$ this condition is verified twice, while the bias is $25kHz$ below or above the resonance resulting on two peaks with amplitudes $23nV/\sqrt{Hz}$, separated by $50kHz$. The noise level is evaluated over a $1 - Hz$ bandwidth. The measured noise with these technique is shown in figure 4.3. The total
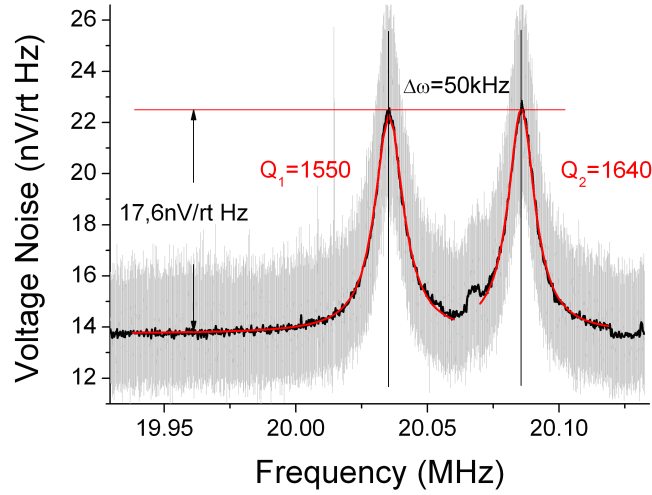
Fig. 4.3: Thermomechanical noise spectral density. Measurements performed using the down-mixing technique

noise measured is constituted by the thermomechanical noise S_{th} , the Johnson noise of the piezo transducers S_J and the read out noise referred to the input of the amplifier S_V. The noise floor $S_d^{1/2} \approx 13.73nV/\sqrt{Hz}$ resulted from both the Johnson noise and input noise of detection electronics. The thermomechanical noise $S_{th}^{1/2}$ can be calculated from the peak amplitude and the floor level and is approximately $17.76nV\sqrt{Hz}$. The Johnson noise is given by $S_J^{1/2} = \sqrt{4k_bTR} = 12.7nV/\sqrt{Hz}$, ($R \approx 10k\Omega$). The electronics noise is then $S_V^{1/2} = \sqrt{S_d - S_J} \approx 5.09nV/\sqrt{Hz}$, which agrees with the noise level specified by the manufacturer of the lock-in amplifier. The device displacement noise spectral density on resonance $\omega_0/2\pi = 20MHz$ at $T = 300K$ with $Q = 1600$ is estimated to be $S_z^{1/2} = \sqrt{4k_bTQ/(2\pi f_0 k)} = 154fm/\sqrt{Hz}$. The contribu-

tion arising from the cantilever's thermomechanical motion is $S_{th}^{1/2} \approx 17.6nV/\sqrt{Hz}$. We can deduce the displacement responsivity (transduction gain) of the devices as $R_v^z = S_{th}^{1/2}/S_z^{1/2} = 0.114nV/fm$. We can use this responsivity to further evaluate the displacement resolution imposed by the off-resonance output voltage noise floor which yields $x_n \approx 13.73nV\sqrt{Hz}/0.114nV/fm = 120.2fm/\sqrt{Hz}$. These results show that we can achieve the ultimate displacement resolution limited by the thermomechanical noise. Assuming an ideal "zero noise" detection scheme the displacement resolution will be always limited by the intrinsic device thermomechanical noise.

4.4.3 Signal to noise ratio

Typically, 1/f-noise created by resistance fluctuations is the main limitation in piezoresistive sensors [62]. However, these resistance fluctuations were not observed in our devices at 20-MHz operating frequency. In order to investigate the consistency of such a result, we computed 1/f-noise density using Hooge's empirical relation [63],

$$S_H = \frac{HV_{bias}^2}{N\left|f - f_{bias}\right|} \tag{4.12}$$

where N is the total number of carriers within the gauge and f_{bias} is the bias frequency. The Hooge parameter H is extracted from the measurement of the relative resistance variation according to the readout voltage frequency for two amplitudes (see Fig. 4.4).

An AC-bias (15 kHz) is used to remove the 1/f-noise of the lock-in. By linearly fitting the data, we find H to be approximately 10^{-6}. From Eqn. (4.12), we then estimate the resulting noise to be a few nV/Hz at 20 MHz, which is negligible compared to other source of noise. To illustrate this, we included the noise floor level (Johnson and electronics noises) and the thermomechanical noise level in terms of relative resistance fluctuation in Fig. 4.4. For frequencies higher than 100 kHz 1/f-noise appears to be lower than other noises. This result is in particular obtained thanks to homogenous doping ($10^{19}cm^{-3}$) in the whole thickness and specific annealing. Bad doping process in conjunction with low doping level could lead to opposite conclusion. It is important to note that we obtain a priori an unexpectedly large SNR (see Fig. 4.5). For our semiconductor nanowire gauges, we infer the piezoresistive gauge factor to be approximately 40, compared to at most a few unities for metallic-layer piezoresistors.
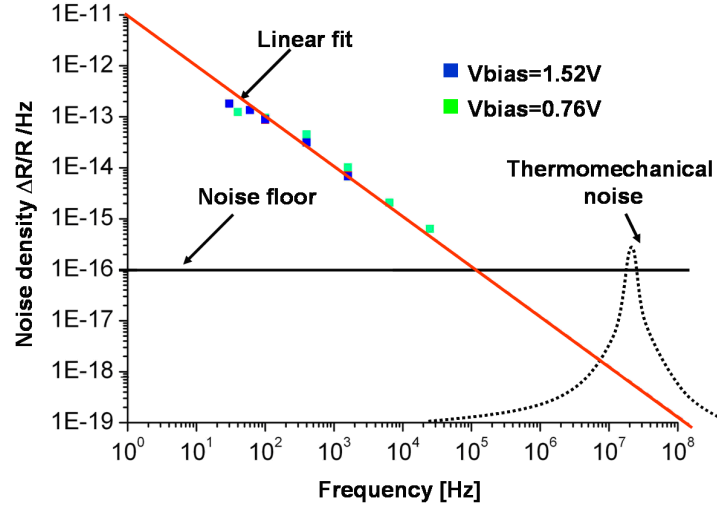
Fig. 4.4: Contribution of different noise sources expressed in relative resistance change, which is independent of V_{bias}. 1/f noise density measurement for different bias voltages (colored squares) compared with both the noise floor and the thermomechanical noise. Red curve is the linear fit of the experimental data for 1/f noise. Black curve corresponds to the noise floor (i.e. electronic and Johnson noises). Black dashed curve corresponds to a schematic of the thermomechanical noise.

The large resistance of the gauges, which is roughly one or two orders of magnitude ($1k\Omega$) larger than that of metallic-layer piezoresistors (10)Ω. Taking into account the Johnson noise only, the SNR is given by :

$$SNR_J = \frac{V_{out}}{\sqrt{S_J}} \propto \frac{GFV_b\epsilon}{\sqrt{4k_bTR}} \tag{4.13}$$

where T and R are the temperature and the gauge resistance respectively, k_b is the Boltzmann constant, V_b is the RMS value of the bias voltage. V_{out} is proportional to $\Delta R/R$ according to equation (3.36). The SNR for semiconducting gauge over SNR of metallic gauge can be simply expressed by,

$$\frac{SNR_{JS}}{SNR_{JM}} = \frac{GF_SV_{bS}}{GF_MV_{bM}} = \sqrt{\frac{R_S}{R_M}} \tag{4.14}$$

Indexes S and M are for semiconductor gauge and metallic layer respectively. At constant temperature considering the aforementioned resistances V_{bS} can be 100 times larger than V_{bM} because of the respective fusion temperature of silicon and metals. The
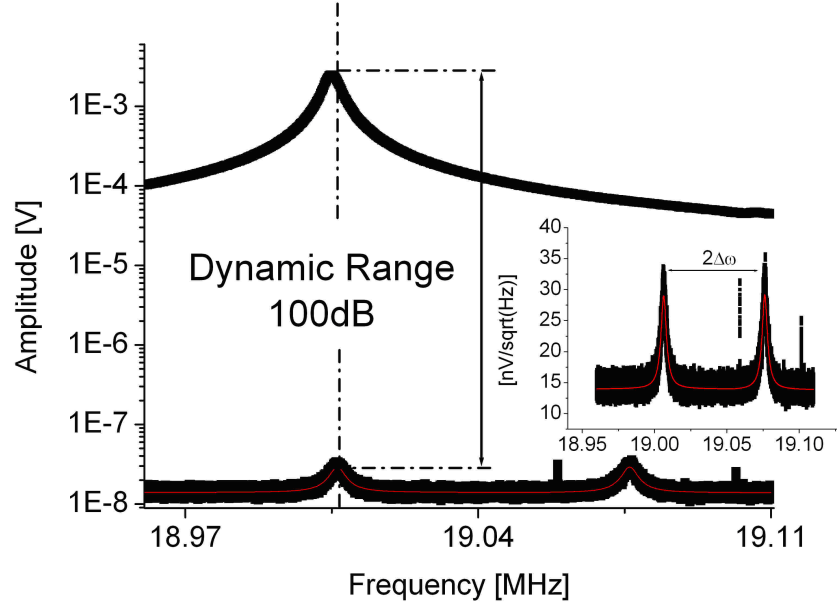
Fig. 4.5: Signal to noise ratio obtained for $V_{drive} = 1.5V$ and $V_{bias} = 1.5V$ - Noise is computed for 1Hz-bandwith - The inset corresponds to the noise density peaks around the resonance frequency.

SNR_{JS} is then 10 times larger than SNR_{JM}. The gauge factor of silicon nanowires are much higher than the metallic layer gauges used as piezoresistive detection scheme for NEMS. The signal improvement is then much higher than the noise enhancement and the Johnson noise impact is limited.

4.5 Evaluation of the piezoresistive factor of nanowire gauges

The thermomechanical noise measurement is an appropriate and accurate way for evaluating the gauge factor of the suspended nanowire gauges. From the equipartition energy relationship $1/2k_{eff} <y_n^2>= 1/2k_b T$ [53, 64] we can estimate the mean square displacement :

$$<y_n^2>= \frac{k_b T}{m\omega_n^2} \tag{4.15}$$

Displacement fluctuations generate strain variations ϵ_{noise} on the gauges and consecutively resistance fluctuations given by :

$$\frac{\Delta R_{noise}}{R} = \Pi \cdot \epsilon_{noise} \tag{4.16}$$

where Π is the piezoresistive factor. We remind that the strain on the gauges is related to the mode amplitude n by :

$$\epsilon_n = \frac{I}{2s} \left[\frac{d^3 U_n}{dx^3} \right]_{l_1-}^{l_1+} y_n \tag{4.17}$$

Then

$$\frac{\Delta R_n}{R} = \left(\frac{\Pi I}{2s} \left[\frac{d^3 U_n}{dx^3} \right]_{l_1-}^{l_1+} \right)^2 \langle y_n^2 \rangle \tag{4.18}$$

Thus

$$\left\langle \left(\frac{\Delta R_{noise}}{R} \right)^2 \right\rangle = \frac{\Pi I}{2s} \left[\frac{d^3 U_n}{dx^3} \right]_{l_1-}^{l_1+} y_n \tag{4.19}$$

The thermomechanical noise is downmixed at a low frequency according to equation (3.49). When applying $V_{b2} = -V_{b1}$ and considering that the resistance variation is similar in both gauges, $(\Delta R_1 = \Delta R_2)$ we obtain :

$$V_0^{(1)} = \frac{V_{b1}(t)\Delta R_1(t)}{R_1 + R_2} \left(\frac{R_2}{R_1} + \frac{R_1}{R_2} + \frac{R_3}{\alpha} \frac{(R_2 - R_1)(R_1^2 - R_2^2)}{R_1^2 R_2^2} \right) \tag{4.20}$$

The measured branch resistances are : $R_1 = 6k\Omega$, $R_2 = 9.65k\Omega$ and $R_3 = 4k\Omega$. The gauge resistances have been evaluated to be, $R_{g1} = R_{g2} = 3.5k\Omega$. By substituting the resistance values in equation (4.20) we obtain the output voltage as function of the resistance variation ΔR and the gauge resistance R_g :

$$V_0^{(1)} = 0.47 \frac{\Delta R_1(t)}{R_{g1}} V_{b1}(t) \tag{4.21}$$

We have now to address the problem of the thermomechanical noise downmixed at low frequency.

$$a(t) = \frac{\Delta R_1(t)}{R_{g1}} V_{b1}(t) \tag{4.22}$$

We introduce $\delta R(t) = \Delta R_1(t)/R_{g1}$ for more simplicity and we explicit the bias voltage $V_{b1}(t) = V_b cos(\nu t)$. We can now calculate the noise spectrum density of the signal at the lock-in input as :

$$S_a(\omega, t) = V_b^2 \int e^{j\omega\tau} \langle \delta R(t + \tau)\delta R(t) \rangle \, cos(\nu(t + \tau)) cos(\nu\tau) d\tau \tag{4.23}$$

The correlation function $\langle \delta R(t+\tau) \delta R(t) \rangle$ is stationary and does not depend on the time t.

$$S_a(\omega, t) = V_b^2 \int e^{j\omega\tau} \langle \delta R(\tau) \delta R(0) \rangle \, cos(\nu(\tau)) cos(\nu(2t+\tau)) d\tau \qquad (4.24)$$

A more accurate calculation would have taken into account the low pass filter which eliminates the high frequency component of the noise density spectrum. Experimentally we are not sensitive to this component.

$$S_a(\omega, t) = V_b^2 \int \langle \delta R(\tau) \delta R(0) \rangle \frac{e^{j(\omega+\nu)\tau} + e^{j(\omega-\nu)\tau}}{4} d\tau \qquad (4.25)$$

Finally we obtain the following spectrum, where peaks at $\nu_0 + \nu$ and $-(\nu_0 + \nu)$ have to be ruled out (ν_0 is the resonance frequency of the resonator).

$$S_a(\omega) = V_b^2 \frac{S_{\delta R}(\omega+\nu) + S_{\delta R}(\omega-\nu)}{4} \qquad (4.26)$$

The lock-in measures the noise projected on X and Y to reference in quadrature filtered by $h(t)$.

$$X = \sqrt{2} \int h(t-\tau) cos(\Delta\omega\tau) a(\tau) d\tau \qquad (4.27)$$

Then

$$\langle X(t)X(0) \rangle = 2 \int h(t-\tau_1)h(-\tau_2) cos(\Delta\omega\tau_1) cos(\Delta\omega\tau_2) \langle a(\tau_1)a(\tau_2) \rangle \, d\tau_1 d\tau_2 \quad (4.28)$$

$$\langle X(t)X(0) \rangle = 2 \int h(t-\tau_1)h(-\tau-\tau_1) cos(\Delta\omega\tau_1) cos(\Delta\omega(\tau_1+\tau)) C_a(t) d\tau_1 d\tau_2 \quad (4.29)$$

where $C_a(t) = \langle a(\tau_1)a(\tau_2) \rangle$. We remind that :

$$h(t) = \int H(\omega) e^{-j\omega t} \frac{d\omega}{2\pi} \qquad (4.30)$$

Thus :

$$\begin{aligned}
\langle X(t)X(0) \rangle = \quad & \tfrac{1}{2} \int d\tau_1 d\tau_2 \tfrac{d\omega_1}{2\pi} \tfrac{d\omega_2}{2\pi} H(\omega_1) H(\omega_2) C_a(\tau) \\
& e^{-j\omega_1 t + j\tau_1(\omega_1+\omega_2) + j\tau(\omega_2+\Delta\omega)} \\
& + e^{-j\omega_1 t + j\tau_1(\omega_1+\omega_2) + j\tau(\omega_2-\Delta\omega)} \\
& + e^{-j\omega_1 t + j\tau_1(\omega_1+\omega_2+2\Delta\omega) + j\tau(\omega_2+\Delta\omega)} \\
& + e^{-j\omega_1 t + j\tau_1(\omega_1+\omega_2-2\Delta\omega) + j\tau(\omega_2-\Delta\omega)}
\end{aligned} \qquad (4.31)$$

$$\langle X(t)X(0)\rangle = \quad \frac{1}{2}\int d\tau \frac{d\omega_1}{2\pi}\frac{d\omega_2}{2\pi}H(\omega_1)H(\omega_2)C_a(\tau)$$
$$2\pi\delta(\omega_1+\omega_2)e^{-j\omega_1 t+j\tau(\omega_2+\Delta\omega)}$$
$$+2\pi\delta(\omega_1+\omega_2)e^{-j\omega_1 t+j\tau(\omega_2-\Delta\omega)}$$
$$+2\pi\delta(\omega_1+\omega_2+2\Delta\omega)e^{-j\omega_1 t+j\tau(\omega_2+\Delta\omega)}$$
$$+2\pi\delta(\omega_1+\omega_2-2\Delta\omega)e^{-j\omega_1 t+j\tau(\omega_2+\Delta\omega)} \tag{4.32}$$

$$\langle X(t)X(0)\rangle = \quad \frac{1}{2}\int d\tau \frac{d\omega_1}{2\pi}C_a(\tau)$$
$$H(\omega_1)H(-\omega_1)e^{-j\omega_1 t+j\tau(-\omega_1+\Delta\omega)}$$
$$+H(\omega_1)H(-\omega_1)e^{-j\omega_1 t+j\tau(-\omega_1-\Delta\omega)}$$
$$+H(\omega_1)H(-\omega_1-2\Delta\omega)e^{-j\omega_1 t+j\tau(-\omega_1+\Delta\omega)}$$
$$+H(\omega_1)H(-\omega_1+2\Delta\omega)e^{-j\omega_1 t+j\tau(-\omega_1-\Delta\omega)} \tag{4.33}$$

$$\langle X(t)X(0)\rangle = \quad \frac{1}{2}\int d\tau \frac{d\omega_1}{2\pi}$$
$$|H(\omega_1)|^2 S_a(-\omega_1+\Delta\omega)e^{-j\omega_1 t}$$
$$+|H(\omega_1)|^2 S_a(-\omega_1-\Delta\omega)e^{-j\omega_1 t}$$
$$+H(\omega_1)H(-\omega_1-2\Delta\omega)S_a(-\omega_1+\Delta\omega)e^{-j\omega_1 t}$$
$$+H(\omega_1)H(-\omega_1+2\Delta\omega)S_a(-\omega_1-\Delta\omega)e^{-j\omega_1 t} \tag{4.34}$$

The last two terms can be neglected because $\Delta\omega$ is much larger than the frequency cut of $H(\omega)$. Then the width of S_a is larger than $H(\omega)$:

$$\langle X(t)X(0)\rangle = \frac{1}{2}(S_a(\Delta\omega)+S_a(-\Delta\omega))\int \frac{d\omega}{2\pi}|H(\omega)|^2 e^{-j\omega_1 t} \tag{4.35}$$

Finally

$$\langle X^2\rangle = (S_a(\Delta\omega)+S_a(-\Delta\omega))B_h \tag{4.36}$$

where

$$2B_h = \int \frac{d\omega}{2\pi}|H(\omega)|^2 \tag{4.37}$$

B_h is the equivalent bandwidth given in the lock-in manual. Noise measurement performed by the lock-in corresponds to $N(\Delta\omega) = \langle X^2\rangle/B_h$, the noise defined only for positive frequencies only. The acquired spectrum can thus be described by :

$$N(\Delta\omega) = V_b^2 \frac{S_{\delta R}(\Delta\omega+\nu)+S_{\delta R}(-\Delta\omega-\nu)+S_{\delta R}(\Delta\omega-\nu)+S_{\delta R}(-\Delta\omega+\nu)}{4}$$
$$\tag{4.38}$$

The first peak we observe in figure 4.3 is described by the first two terms and the second one by the last two. Integrating this spectrum from $\delta\omega = 0$ to $+\infty$ gives :

$$A_a = V_b^2 \left\langle \delta_R^2 \right\rangle /2 \tag{4.39}$$

Both of the peaks have to be included. Experimentally we can estimate :

$$A_{V_0} = 0.47^2 V_b^2 \left\langle \delta_R^2 \right\rangle /2 \tag{4.40}$$

Based on this model we can now evaluate the gauge factor. Experimental parameters used to acquire the noise spectrum were, $V_b = 1.76V$, $A_{V_0} = 2 \times 5.36 \times 10^{-12}V^2$ and the strain $\langle \epsilon \rangle = (2.45 \times 10^{-7})^2$. The piezoresistive gauge factor is equal to :

$$GF = \sqrt{\frac{\langle \delta R^2 \rangle}{\langle \epsilon^2 \rangle}} \tag{4.41}$$

The gauge factor we have obtained is $GF = 22$. Uncertainties on the bias voltage V_b and gauge resistance may vary this parameter by a factor of 2. A gauge factor of $GF = 47$ was observed by Arlett et al. [65] in p-doped and similar values were predicted from Tufte et al [66]. This efficient detection method opens the way to the investigation of piezoresistance in silicon nanowires otherwise complicated.

4.6 Allan deviation

Usually NEMS are embedded in a phase locked loop (PLL) or a self-excited loop in order to monitor time evolution of their resonant frequency. The frequency stability of the overall system (e.g. of the NEMS and the supporting electronics) is characterized by the Allan deviation, defined as [62],

$$\frac{\delta\omega_0}{\omega_0} = \sqrt{\frac{1}{(N-1)} \sum_N^1 \left(\frac{\overline{\omega_{i+1}} - \overline{\omega_i}}{\omega_0} \right)^2} \tag{4.42}$$

where $\overline{\omega_i}$ is the average angular frequency in the ith time interval τ and N is the number of independent frequency measurements, which is assumed to be a sufficiently large number. The mass resolution δm is then $\sqrt{2}M_{eff}\delta\omega_0\omega_0$ for 1s-integration time. The theoretical Allan deviation can be expressed as [67]

$$\left(\frac{\delta\omega_0}{\omega_0} \right)_{th} = \frac{10^{-DR/20}}{\sqrt{2}Q} \tag{4.43}$$

For the experimental dynamic range, (DR) of 100 dB (see Fig. 4.5) the ultimate Allan deviation would be around 1.5×10^{-9} over 1s-integration time. For an effective mass of 140 fg (see TAB. 3.4) and a Q- factor of 5000, this would result in a potential mass resolution of $\delta m = \frac{M_{eff}}{Q} 10^{-DR/20} = 0.3zg$ at room temperature and at relatively low frequency (20 MHz). As mentioned afterward this theoretical mass resolution should be considered as the lower limit.

The experimental Allan deviation was measured in open loop recording the phase variation of the electrical signal at the NEMS output. NEMS was driven at its resonant frequency (20MHz). The Allan deviation was measured in three steps (for short, intermediate and long times). For low time constants (¡0.1s), the integration time of the lock-in and the global acquisition time were $100\mu s$ and $10s$ respectively. For larger time constants, they were set to $100\mu s$ and $4000s$ ($50000s$) respectively. These adjustments remove the effect of the lock-in filtering that would artificially decrease the Allan deviation and ensure at least 100 points for each interval. We can also note that the smallest interval is set by the transient time Q/f (i.e. $250\mu s$ in our case). Typical experimental data are shown in FIG 4.6.
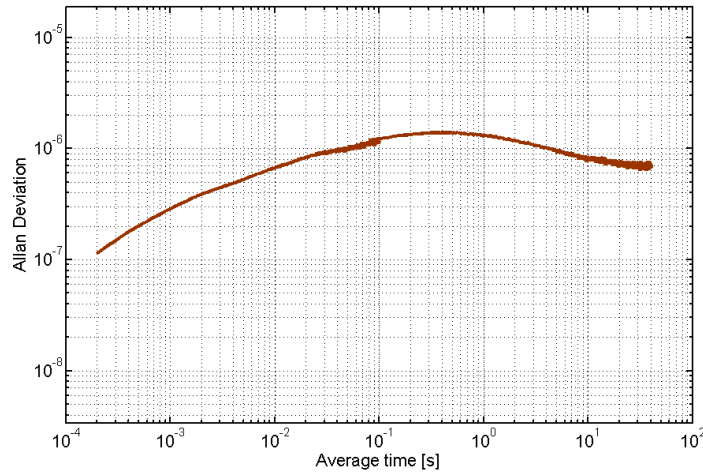
Fig. 4.6: Allan deviation measured in open loop for $V_{drive} = 1.5V$ and $V_{bias} = 1.5V$.

For mass sensing the study has to be focused on short times lower than 1s. Typically, we achieved an Allan deviation of 10^{-6} for $\tau = 1s$ at room temperature. For long time constant, the minimum Allan deviation reaches $6 \cdot 10^{-7}$. This value is quite a classical one reported in many papers (see [60], [68] for example) and might be

considered as the experimental limit.

The large difference of three orders of magnitude between the expected value and the experimental Allan variance has to do with the fact that actuation is not present during thermomechanical noise measurement. The DR measurements therefore do not take into account noise contributions from the actuation voltage and the thermal bath. Considering both a typical silicon NEMS temperature coefficient of 50 ppm/K and an Allan deviation close to 10^{-6}, the related thermal bath temperature fluctuations will be around 10^{-2} K. The effect of temperature fluctuations on cantilever measurements is well explained in Ref [69]. To get better frequency stability we think that the temperature fluctuation should be controlled at least below this value. It is also essential to suppress the background level as much as possible in order to reduce the additional phase noise that results from background fluctuations associated with electronic and temperature instabilities. The discrepancy between the Allan deviation obtained with eqn. (4.43) and the experimental data is an open question that is currently being studied.

Chapitre 5

Carbon nanotube NEMS resonators

Carbon nanotubes (CNT) are structures with nanometric dimensions presenting exceptional electrical and mechanical properties. They show semiconducting or metallic electric behaviors based on the tube chirality and diameter[70, 71]. They posses the highest mechanical strength among known materials with Young's modulus up to the TPa[72, 73, 74, 75]. These attributes make them great candidates for high frequency nano-electromechanical systems. Carbon nanotubes have minuscule masses around $\approx 10^{-18}g$ and resonance frequencies on the GHz range[25, 29]. Quality factors of CNT resonator up to 2500[76, 77] have been measured and lastly quality factors above $Q = 10^5$ were reported [78]. The values are usually higher for free-end suspensions[74, 76, 77] and lower for doubly-clamped ones[17, 26, 29]. Reducing the mass of the resonator while maintaining high resonance frequencies is critical for the achievement of ultrasensitive mass sensors. Carbon nanotubes are ideally suited for this task assuming large SNR and SBR values.

Our objectives are :

1. fabricating CNT NEMS devices operating at high frequencies

2. developping a detection schema able to detect the CNT resonator nanomechanical motion

In this chapter we will focus on the fabrication of CNT-NEMS resonators and the characterization of their low and high frequency properties. First, three different processes were developed for fabricating the CNT based resonators. Second, we implemented

a detection scheme operating at high frequencies able to detect the nanometric CNT resonator displacement.

5.1 Fabrication of CNT resonators

The top-down fabrication process of NEMS devices is hard and complex at the nanoscale. Handling nano structures such as CNT-s and positioning in precise locations for building devices is the main issue. Our objective is to find an efficient fabrication process for fabricating CNT based NEMS for high and low frequency operations. The research is focused in two directions. First to find an easy process and no time consuming for fabricating high frequency CNT-NEMS devices. Second, to precisely control the CNT deposition, in order to fabricate NEMS devices in specific locations. We are going to fabricate devices based only on ex-situ multi-walled carbon nanotubes (MWNT) synthesized via arc-discharge evaporation. MWNT-s have been chosen due to their stronger mechanical properties respect to single walled nanotubes. MWNT-s mechanically support better the suspension process which is achieved via wet-etching and are more resistant to bending. Handling ex-situ MWNT nanotubes in solution it is easer for obaining single separated on the substrate than SWNT-s which are in bundles.

MWNT-s were purified with an $H_2O_2 + H_2SO_4$ process [79] to remove the amorphous carbon the graphitic nanoparticles. The purified CNT-s were diluted and conserved in a dichloroethane (DCE) solution with concentration $30 - 80\mu g/ml$. The fabrication process was started with an SiO_2/Si ($100nm/700\mu m$) non conducting substrate. The carbon nanotubes have been dispersed on the SiO_2 sacrificial surface and will become the vibrating mechanical parts of the NEMS devices. Localizing, contacting and suspending the deposited nanotubes on the substrate with high precision are the main technological challenges.

5.2 Nanotube random deposition followed by lateral gate patterning

This method consists on dispersing the nanotubes randomly on a SiO_2/Si substrate with mark aligners on it. The SiO_2 acts as a sacrificial layer. The nanotubes are located through AFM imaging and contacted further with a lithographic and evaporation process. A third lithography is needed to define the suspension areas and a HF isotropic etching is carried out (figure 5.1). The main fabrication steps are : 1.
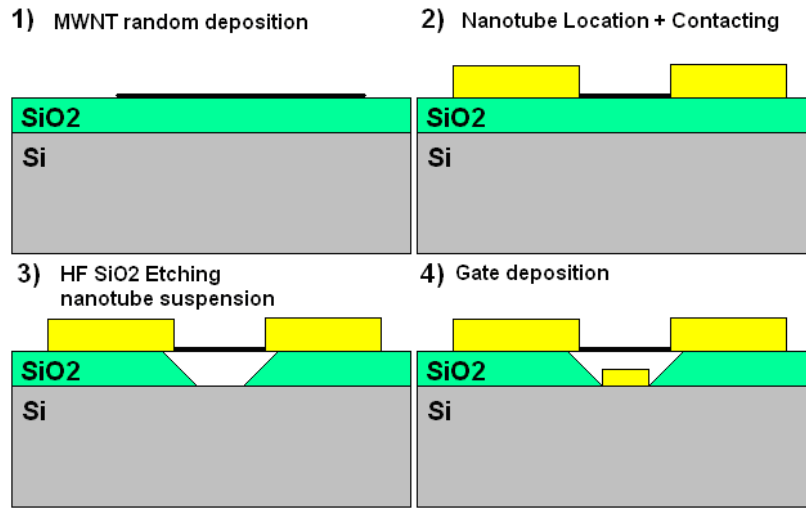
Fig. 5.1: Fabrication steps for the first method with lateral actuation electrodes

alignment mask definition, 2. CNT random deposition 3. CNT location 4. contacting CNT-s and 5. suspension of CNT-s.

5.2.1 Alignment mask

Localizing the nanotubes on the substrate is the first step toward contacting and suspending these structures. How can they be localized ? We have used an alignment mask which has two purposes. First to localize the CNT-s on the substrate and second to be used for the alignment of successive lithographic processes. The mask is composed by alignment and localization marks (crosses, letters and numbers), which indicate the location on the substrate (figure 5.2). The alignment precision achieved with these technique is around $50nm$.
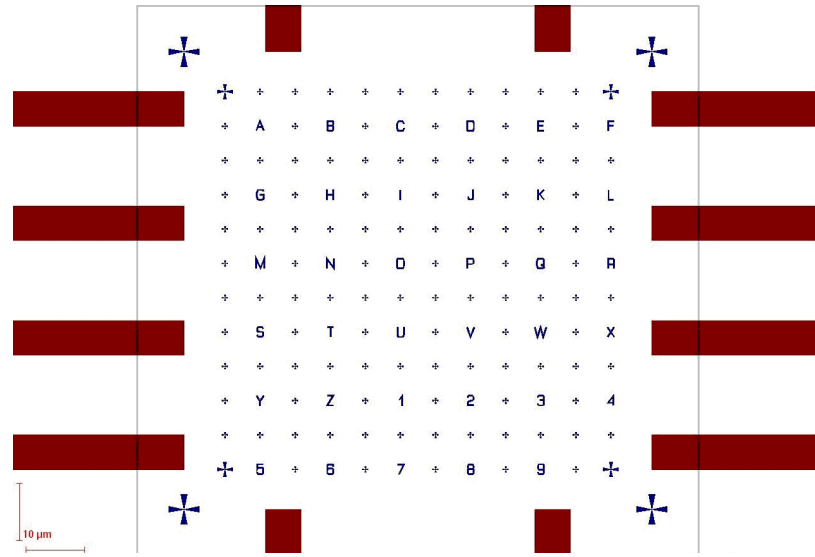
Fig. 5.2: Alignment mask used for CNT localization and lithographic processes alignment

5.2.2   Nanotube deposition and location

For obtaining a homogeneous dispersion of CNT-s, the solution was sonicated at 40% for 6 minutes. Successive droplets of $10\mu l$ from a dicloroethane CNT solution with concentration $50\mu g/ml$ were used to deposit the nanotubes into the $Si0_2$ surface. The solution was left from 40-50s for the nanotubes to precipitate on the substrate surface. The sample was then sprayed with a pressurized nytrogen flow before the solution starts to completely evaporate. It is important not to leave the DCE droplet to dry since during its evporation all the solution impurities will be deposited on the substrate resulting in a very dirty sample surface.

The location of nanotubes is done through AFM imaging. Scanning electron microscopy (SEM) imaging is avoided since it will deposit amorphous carbon on the CNT resulting in a deteriorated and increased contact resistance. The AFM localization is very time consuming but it wont change the electrical properties of the CNT-s. The pre-patterned area with the alignment marks is scanned in order to find the eventual nanotubes deposited during the deposition process. In figure 5.3 it is shown an AFM image of a deposited carbon nanotube. This image is overlapped to the alignment mask in order to draw its location on the mask and to proceed with the contacting lithographic process (figure 5.4). To increase the precision of the CNT location the AFM images are elaborated in order to compensate the rotation and the

horizontal squeezing due to the misalignment and AFM piezoelectric tube drift. This ensures a CNT location with 10nm precision.

Fig. 5.3: Localisation of CNT-s through AFM imaging

5.2.3 Contacting Nanotubes

Based on the location of the CNT-s identified by AFM imaging we designed the e-beam lithography mask which has to be transferred on the sample. For the lithographic process the sample was covered with a 200nm thick A4 950K PMMA (polymethyl methacrylate) resist layer. The resist was spinned on the sample for 60s at a rotation of 4000rpm and a soft baking to ensure its adhesion to the substrate was performed afterward at $170C$ for 15 minutes. The sample was then introduced in the e-beam microscope (Philips S-FEG XL 30 controlled via Elphy Quantum 1.3) for writing the contact electrodes. The exposed resist regions were then developed for 45s in a MYBK :IPA 1 :4 (methyl-isobutyl-ketone/isopropyl-alcohol) mixture. The sample is rinsed for 45s with IPA and dried with pressurized nitrogen flow pistol. The CNT-s are later contacted by thermal evaporation of a Cr/Au 5/50nm layer with the PMMA resist acting as a mask. A thin chrome layer is used for contacting the nanotubes due to its good adhesion and lower contact resistance respect to other metals. Both these metals are resistant to the HF wet-etching process. A lift-of process is performed later

to remove the resist layer.
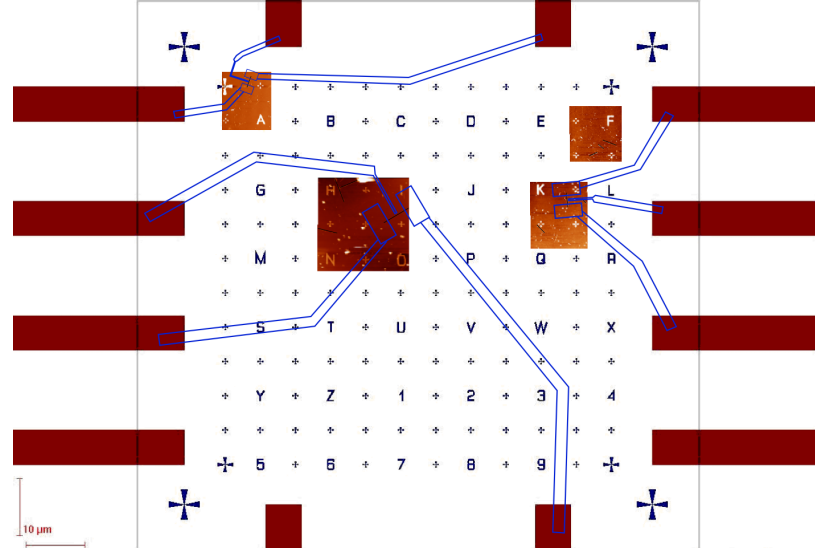
Fig. 5.4: Localisation of the nanotubes in the alignment mask and design of e-beam lithography for contacting nanotubes

5.2.4 Nanotube suspension

For suspending the nanotubes a second lithographic process is performed to define the suspension and gate electrode regions. For the DC actuation of CNT-s there is no need to pattern specific gate electrodes since in this case a highly As doped n++ ($10^{19}cm^{-3}$) conducting substrate was used for this purpose. For etching the silicon dioxide (SiO_2)layer the sample is immersed in a buffered hydrofloric (BHF) solution for about 60s and then rinsed in deionized water solution. Since the etching rate of SiO_2 that we have observed was about 1.8nm/s this time was sufficient to etch the 100nm SiO_2 layer. The wet etching is an isotropic process which means that 100nm will also be removed underneath the resist on the lateral directions resulting in a higher etched area than that defined by the lithographic design. The nanotube suspension through wet etching is a critical process where strong capillary forces tend to stick the nanotubes to the substrate. In our processes this problem has been circumvented by the use of a supercritical point dryer, where the liquid phase is bypassed. In the case of high frequency devices a lateral gate is patterned (figure 5.5b). We have achieved nanotube-gate lateral distances of about 50nm. The isotropic

etching resulted in removed SiO_2 beyond the gate area suspending thus the nanotube situated in the gate vicinity. The CNT suspension length was defined by the gate width + 2 times the lateral etching of 100nm. In the case of the NEMS devices fabricated
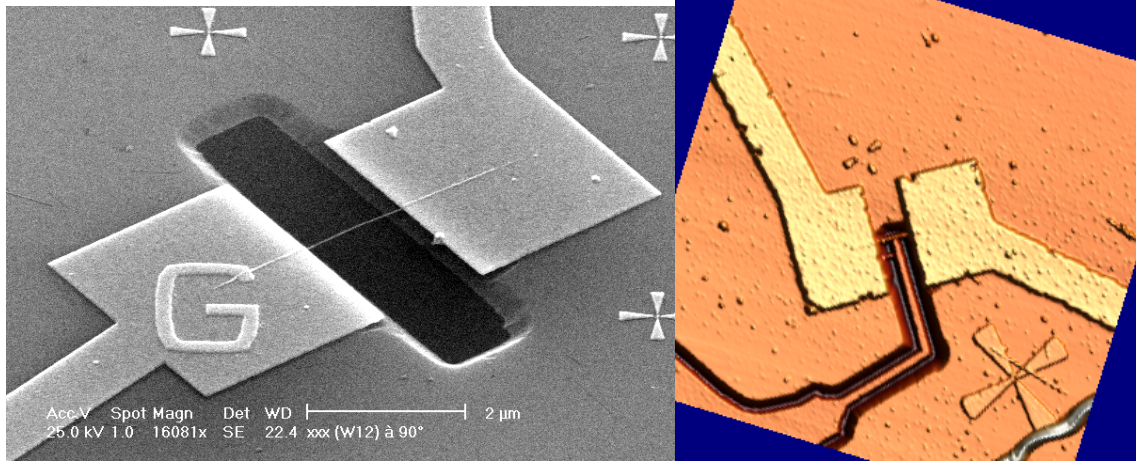
(a) Nanotube suspension through BHF etching. n++ bulk used as backgate for static deflection experiments

(b) Nanotube suspension achieved via lateral isotropic etching. Lateral buried gate for high frequency actuation

Fig. 5.5: Suspension of CNT-NEMS structures

for DC experiments the n++ doped Si substrate is electrically connected and acts as the actuation gate. This has been our classical method for fabricating the CNT-NEMS devices and its advantage is easy of implementation. The main drawback is the lack of control on the position of the deposited CNT-s. For efficient high frequency capacitive actuation it is required a small gap between the nanotube and the lateral gate. The gap in this case is limited by the alignment precision about 50nm in our experiments.

5.3 Fabrication of NEMS devices with buried Au/Cr actuation gates

For efficient capacitive actuation it is necessary to increase the electrostatic coupling between the actuation gate and the suspended nanotube. For maximizing the electrostatic drive force $F = C'V^2/2$ it is required a higher area A between the plates of the capacitor C and smaller distance d between them. In our case the two plates

are represented by the nanotube and the Au/Cr gate electrode. How can we maximize this capacitance? We can maximize the overlapping area between the nanotube and the gate electrode or decrease their gap. The maximal overlapping area is obtained when the gate is situated beneath and crossing the nanotube. The vertical gap in this case can be controlled precisely through the evaporation process (deposition rate 0.1nm/s) of the gates with nanometric precision.

This method consists on evaporating the mask alignment and the Au/Cr actuation gates and then depositing randomly the nanotubes. The nanotubes are deposited randomly on the SiO2/Si surface. AFM imaging is performed for nanotube localization. A second lithography is used to design the contacts and the high frequency lines (figure 5.6). The main process steps are : 1. Au/Cr gate evaporation 2. random nanotube deposition 3. nanotube location via SEM imaging 3. contact + high frequency lines design.
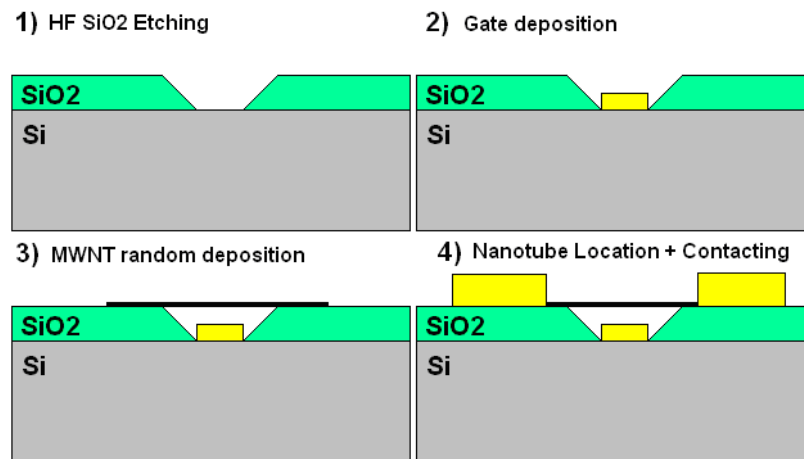
Fig. 5.6: CNT NEMS fabrication process. Gate deposition + randon oriented nanotube deposition.

5.3.1   Buried gate design

This process was started with a sample which had alignment marks already patterned on it. A lithographic process is used to define the gates. Isotropic BHF etching was used to remove the sacrificial 100nm thick SiO_2 oxide layer. The Au/Cr gates were then deposited by thermal evaporation in the patterned regions. The thickness of the Au/Cr metallic layer is the parameter determining the nanotube gate distance.

We have evaporated gates with thickness varying from 50-70nm allowing to achieve a nanotube-gate distance from 30-50nm. A lift-of process was then performed to remove the resist mask layer. A droplet from a solution with the diluted carbon nanotubes was then deposited in the buried gates region. After 45s the droplet is dried with a pressurized nitrogen flow pistol. The flow direction was discovered to have an important effect on the alignment of the nanotubes deposited on the sample. We have applied it perpendicular to the buried gates in order to align the nanotubes in the flow direction. How did we increase the probability of nanotube-gate crossings ? First we increased the number of gates by designing several of them in parallel as shown in figure 5.7, and second we increased the concentration of the deposited nanotubes by repeating the deposition process and applying successive droplets of CNT solution. With these method only a lithographic process is required for contacting the nano-
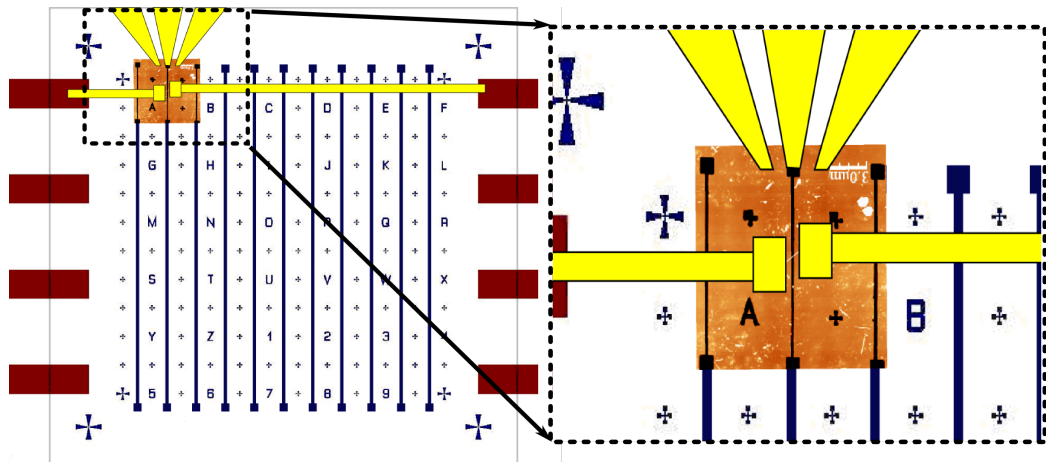
Fig. 5.7: Image of an alignment mask with parallel gates. Inset showing an example of an e-beam lithographic design for contacting the nanotubes

tubes and obtaining the NEMS resonator. The alignment precision in this process is less important since the gap between the nanotube and the gate is determined by the gate thickness. The length of the suspended nanotube depends on the gate width plus two times 100nm added from the lateral isotropic etching,(see figure 5.8). Although this technique relies on serendipity for tube deposition over the gates it is very simple, versatile and time efficient. With this method we have no control over the carbon nanotube deposition and it cannot be used in pre-designed contact structures where the nanotube has to be deposited at a very high precise locations.
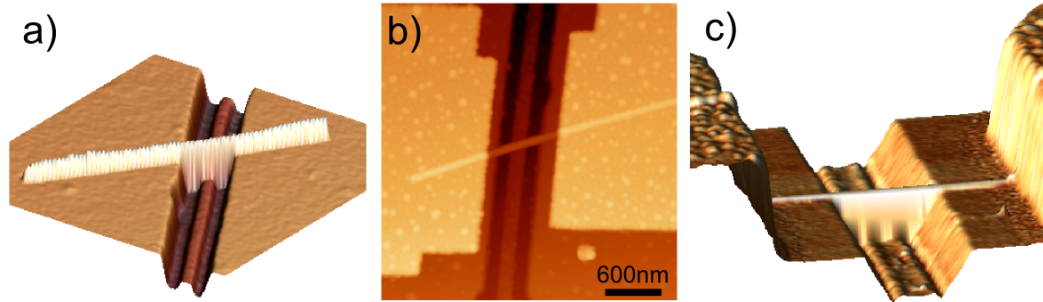
Fig. 5.8: Experimental results of the fabrication process. a) 3D AFM image of a nanotube crossing the gate, b) AFM image of a contacted nanotube, c) 3D AFM image of a doubly clamped suspended CNT resonator

5.4 Fabrication of CNT-NEMS by Dielectropohoresis

Controlling and manipulating structures at the nanoscale remains still a big challenge. In more complex devices it is desired to combine NEMS to CMOS electronics and it will help to minimize the parasitic capacitance effect. How can we fabricate CNT-NEMS devices in a chip with pre-designed contacts and CMOS electronics on it ? A precise control over CNT deposition and reproducible process is required. The goal of this part was to precisely control the location where CNT-s are going to be deposited on the sample. Several strategies can be followed such as in situ synthesis of nanotubes or ex-situ deposition. In the first case metal catalysts can be patterned at the location were the nanotube is desired and the synthesis process (i.e CVD) can be carried out [80, 81]. The main problem of this technique is the high synthesis temperature, the lack of orientation, length and number of grown nanotubes. In the ex-situ deposition process we can proceed via chemical surface functionalization [82] or control the nanotube deposition via electric fields. The surface can be functionalized with molecules having a strong affinity for the nanotubes. The specific locations can be determined and designed via lithographic processes. The problem of these "sticking layers" is that more than one CNT or other kind of carbon molecules would be attracted resulting in a network of CNT than a single one. Another method is that of using an electric field to guide the tube deposition. Handling electric fields is less complicated, especially when the pre-designed contacts can be used as elec-

trodes for applying the electric field and attracting the nanotube. We have explored this method for placing the nanotubes at the prefered locations. The main steps of these fabrication procedure are shown in figure 5.9. The first process of this method
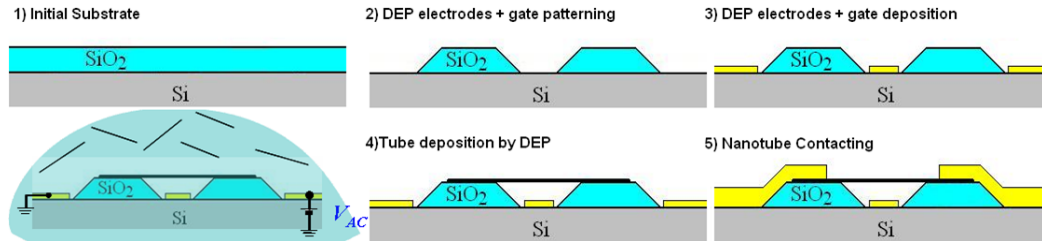
Fig. 5.9: CNT nems fabrication process. Gate deposition + nanotube deposition by DEP

consists in fabricating on the same step the alignment mask, the buried gates and the contact electrodes for the dielectrophoresis deposition of CNT-s (figure 5.10). The nanotubes are deposited through dielectrophoresis. The nanotube location is done through scanning electron microscopy (SEM). After the DEP process the tubes are already electrically contacted (figure **??**c) but in order to reinforce the contact and increase the mechanical stability of the suspended tube a layer of Au/Cr $50/2nm$ has been added.
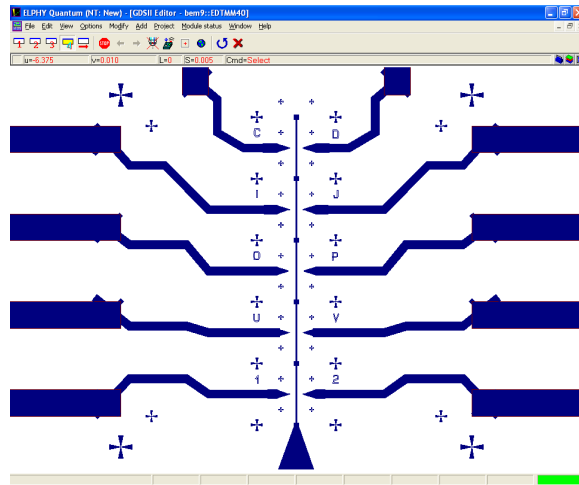
Fig. 5.10: E-beam mask for the dielectrophoresis nanotube deposition

5.4.1   CNT deposition via dielectrophoresis (DEP)

Specific electrodes have been added in order to apply the electric field and attract the nanotubes. The carbon nanotubes were dispersed in N-methyl pyrrolidone (NMP) solution [83]. This solution assures a good dispersion of nanotubes and limits the tube deposition via precipitation. A radio frequency signal at $f = 10MHz$ was applied
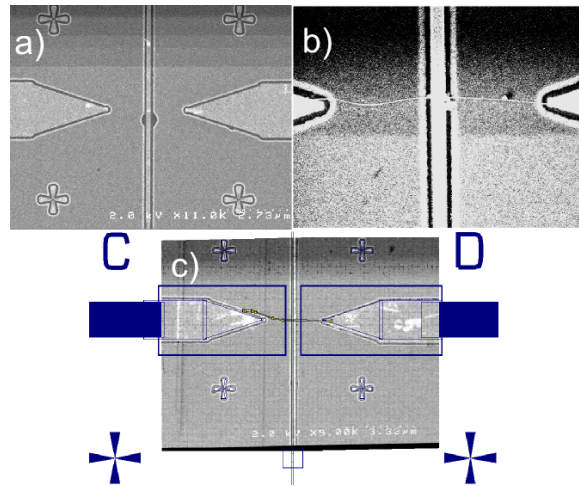
Fig. 5.11: Fabrication of NEMS devices via dielectrophoresis CNT deposition. a) SEM image of a sample prepared for the dielectrophoresis, b) deposition of a single CNT via DPE and c) e-beam contacts design

between the dielectrophoretic electrodes. How can we control the amount of tube's deposited with this technique? The amount of tubes deposited between the electrodes depends on two factors. The magnitude of the electric fields and the time duration it is applied. We have used electrode-electrode distances of $2.5\mu m$ with gate widths of $250nm$. We have applied RF signals with amplitude from 1-4V exploring electric fields ranging from $E = 0.4 - 1.6\frac{MV}{m}$ and deposition times from $1 - 3$ minutes. Attracting only one tube at a time from a solution with millions of nanotubes is quite hard and challenging. This is due to the fact that there are millions of them feeling the same attraction force which tend to move on the same direction. Despite the difficulties we have been able to place with nanometric precision only one nanotube at a time figure 5.11c. The optimal conditions were obtained with a RF of $3V_p$ ($E = 1.2\frac{V}{m}$) and $1min30s$ deposition time. This method can be further sophisticated with external electronics controlling the dielectrophoresis process. The deposition of a nanotube

will create a short circuit between the electrodes allowing the current to flow. The presence of a current between the electrodes can be used to stop automatically the electric field and avoid the attraction of additional nanotubes. With this technique we could deposit nanotubes only between the electrodes and nowhere else. It is efficient when networks of nanotubes are desired to be deposited but extremely difficult and time consuming for depositing a single nanotube.

5.5 DC characterisation of the electromechanical behaviour of CNT based devices

The objective of this work was to estimate experimentally the electromechanical properties (Young's modulus) of our CNT-NEMS devices. The Young's modulus is an essential parameter for characterizing the mechanical properties of materials. It will give us an insight on the effective and practical mechanical strength of carbon nanotubes structures. The data obtained in this step are important for evaluating the high frequency operation of these devices. The experiment consisted in bending the nanotube (clamped-clamped or clamped-free) via electrostatic forces and measuring its deflection with an AFM technique. From this measurements according to the Euler-Bernoulli beam bending theory the Young's modulus of the carbon nanotubes has been extracted.

5.5.1 Electrostatic force

The main bending force causing the nanotube deflection is the electrostatic one which is proportional to $F_{el} = \frac{1}{2}C'_g V_g^2$, where C_g is the nanotube gate capacitance, C'_g the capacitance derivative respect to the displacement y and V_g the electrical potential between them. The nanotube suspended over the conducting silicon substrate is considered as a wire over a ground plane which capacitance is given by[84, 85, 86] :

$$C'_g = \frac{2\pi\varepsilon_0 L}{acosh\left(\frac{2h}{d}\right)} \tag{5.1}$$

where L is the tube length, d is the diameter and h the nanotube gate distance as shown in figure 5.12. If we derive C_g respect to the displacement y we obtain :

111
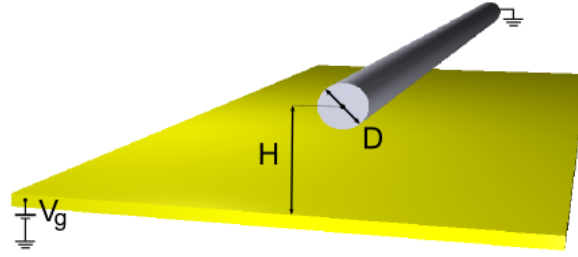
Fig. 5.12: Nanotube gate Capacitance

$$\alpha = \frac{\mathrm{d}C_g}{\mathrm{d}y} = \frac{4\pi\varepsilon_0 L}{d \cdot acosh\left(\frac{2h}{d}\right)^2 \sqrt{\left(\frac{2h}{d}\right)^2 - 1}} \qquad (5.2)$$

The electrostatic force applied to a grounded nanotube of diameter d at a distance h over the conducting plane at a pontential V_g results :

$$F_{el} = \frac{1}{2}C_g' V_g^2 = \frac{2\pi\varepsilon_0 L V_g^2}{d} g(2h/d) \qquad (5.3)$$

where $g(t) = \left[acosh\left(\frac{2h}{d}\right)^2 \sqrt{\left(\frac{2h}{d}\right)^2 - 1}\right]^{-1}$. The function $g(t)$ can be approximated to $\beta t^{-\gamma}$ with $\beta = -0.228$ and $\gamma = 1.258$ within the range $10 < h/d < 50$ achieved experimentally.

5.5.2 Static CNT deflection experiment

The electromechanical DC characterization of our CNT based devices is done by applying different electric voltage to the Si substrate which has been higly dopped n++ to make it conductive. The deflection was then measured through AFM. From this measurements the Young's modulus has been extracted. In figure 5.13 it is shown a schematic of the experimental setup used for measuring the mechanical deflection of the nanotube. The CNT-NEMS device has been placed in an AFM microscope with a conducting tip. For measuring the CNT deflection as a function of the gate voltage V_g the AFM is used in the tapping mode[87] in order to minimize its force effects on the nanotube. In this mode the AFM tip is oscillated at its resonant frequency with constant oscillation amplitude (and thus a constant tip-sample interaction) is maintained during scanning. The feedback loop which controls the piezo crystal with a voltage V_p ensures a constant oscillation amplitude. Both the nanotube and the tip
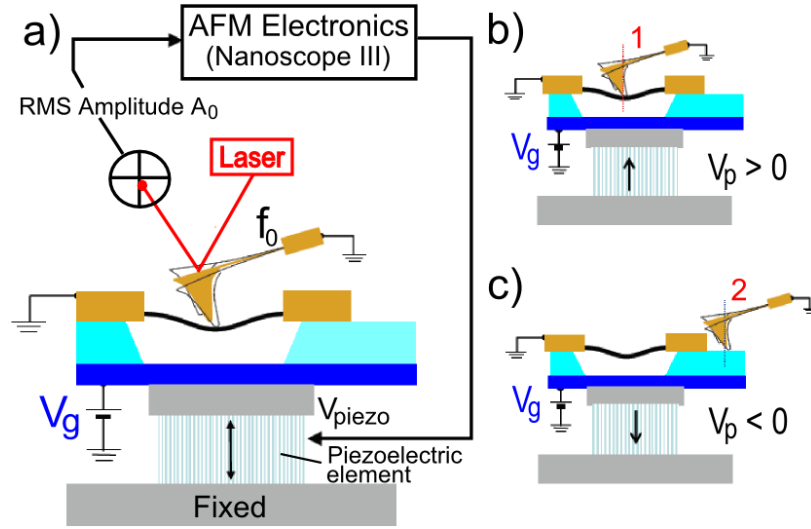
Fig. 5.13: a) AFM experimental setup for measuring the static deflection of the CNT under a DC electrostatic force b) AFM tip placed at the center of the doubly clamped CNT for measuring the maximal displacement c) AFM placed over the SiO_2 position at fixed height for measuring the gate electrostatic effect on the tip

are grounded in order to avoid the electrostatic interaction between them. For measuring the maximal deflection the AFM is placed and stopped at the center of the doubly clamped beam. The AFM is operated several hours after it has been switched on, where the tip position drift becomes negligible. Reproducible and stable measurement are achieved by using an AFM tip with a radius of curvature higher than that of CNT-s. The control voltage V_g applied to the gate attracts the CNT downward via electrostatic interaction. When the CNT bends downward the AFM tip has more room and increases its oscillation amplitude (the near field interaction between the AFM tip and the CNT surface becomes smaller). For keeping a constant oscillation amplitude a positive retro-action signal V_p proportional to the CNT deflection is applied to the piezo crystal moving the stage upward. The retro-action signal V_p proportional to the CNT deflection is registered as a function of the gate voltage V_g (curve nr. 1 figure 5.14). The measured voltage V_p proportional to the CNT deflection scales as V_g^2. The experimental results confirm the nanotube deflection due to the electrostatic force attraction which is proportional to V_g^2 (see equation (5.3)). The electrostatic force interacts the same way with the AFM conducting tip, introducing thus a systematic error on the vertical deflection measurements. How can we estimate
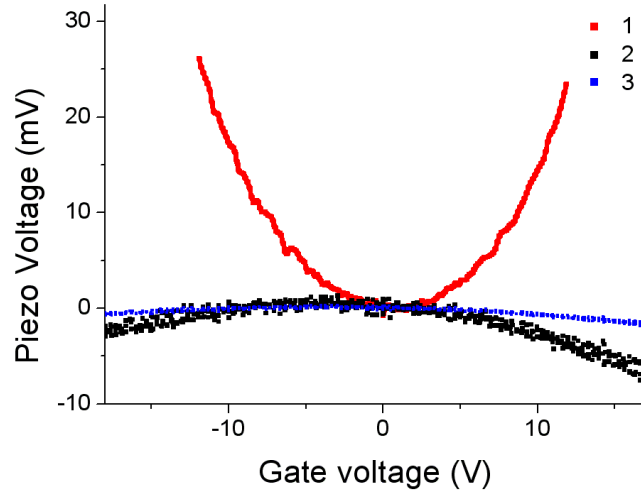
Fig. 5.14: The retro-action signal V_p applied to the AFM piezoelectric tubes as a function of the gate voltage. The curve nr. 1 measured at position 1 in figure 5.13 includes the nanotube deflection plus the AFM-gate electrostatic interaction. The curve nr.2 measured at position 2 in figure 5.13 shows the effect of the electrostatic force on the AFM-conducting tip. The third curve shows the AFM systematic error introduced in the measurements by the AFM. This effect becomes minor respect to the curve measured in 1, at higher deflection amplitudes.

and extract this parasitic effect for obtaining the correct CNT deflection curve? For measuring the electrostatic interaction on the AFM tip, we placed it over the silicon dioxide SiO_2 at the same height as the nanotube. Raising the voltage V_g applied to the substrate increases the electrostatic attraction force between the conducting substrate and the AFM tip. The tip will get closer to the SiO_2 resulting in a lower oscillation amplitude. For keeping a constant oscillation amplitude a negative retro-action signal V_p proportional to the tip approach is applied to the piezo crystal moving the stage downward (curve nr. 2 figure 5.14). Since the dielectric between the AFM tip and the conducting substrate at the center of the nanotube is air the electrostatic force effect would be 3.9 times smaller (SiO_2 dielectric constant). The piezo tube voltage corresponding to the real deflection of the nanotube is obtained by subtracting the curve measured at the center of the CNT with the one measured at the SiO_2 divided by 3.9 (curve nr.3 figure 5.14). For converting the voltage curves $V_p(V_g)$ into displacement ones $y(V_g)$ it is necessary to have the conversion factor (in nm/V) associated

to the piezoelectric tubes. For this purpose we had to proceed with a calibration step for estimating the conversion factor.

5.5.3 AFM calibration for CNT displacement evaluation

The important information we want to get from this step consists on evaluating the amount of piezo voltage corresponding to a given displacement. For this reason a trench of 230nm of SiO_2 and 55nm Au/Cr layer was chosen for the experiment. Profile data extracted from the AFM image, confirm a height of 285nm, figure 5.15. The piezo voltage V_p related to the 285nm step has then been registered. The piezo

(a)   (b)
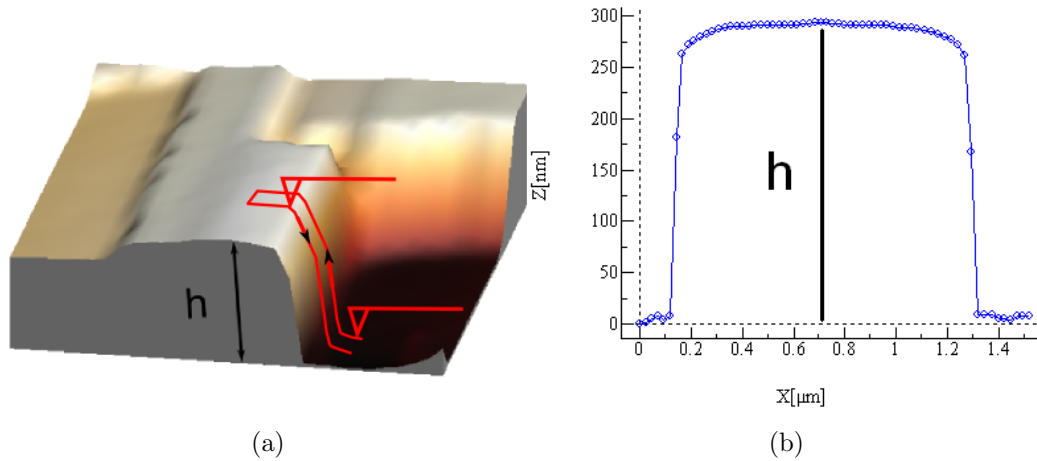
Fig. 5.15: a) 3D AFM image and b) profile data of a 285nm trench

voltage step V_p, figure 5.16 presents an amplitude of $2.03V$ leading to a conversion factor of $140nm/V$. The deflection of the nanotube $y(V_g)$ as a function of the substrate voltage V_g is depicted in figure 5.17.

Various measurements were performed with CNT devices of different length and diameter. From the electrostatic applied force and the experimental defelection measurements the Young modulus has been determined.We have extracted a young modulus of $E = 410 \pm 20GPa$.
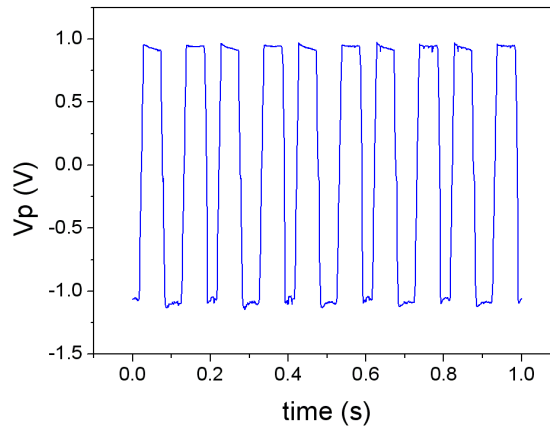
Fig. 5.16: piezo voltage V_p related to the 285nm step, voltage step amplitude $V_p = 2.03V$
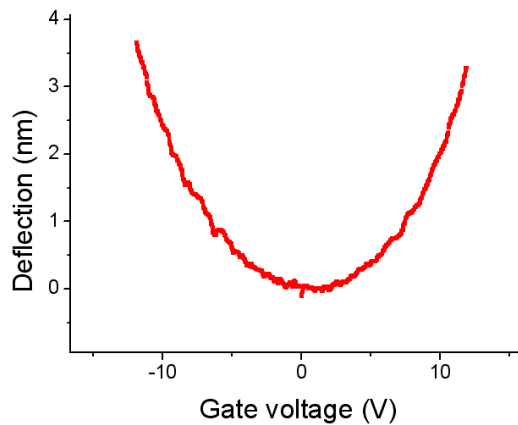
Fig. 5.17: Deflection of the nanotube as a function of the gate voltage V_g

5.6 Development an actuation/detection schema for high frequencies characterization

The objective of this section consist in investigating the high frequency electro-mechanical properties of carbon nanotube resonators, such as resonance frequency, quality factor, and young modulus. In this step the resonance frequency results should meet the predicted ones from the DC young modulus measurements. For characterizing the high frequency NEMS properties it is primordial to develop a nanomechanical

motion detection testbench. Parallel to the exploration of CNT resonator fabrication processes a displacement detection technique[29] for measuring the resonance frequency of the CNT-NEMS has been implemented. For measuring the high frequency CNT displacement we used again the AFM. A normal question arise, how is it possible to measure the high frequency CNT displacement ($\omega_0^{CNT}/(2\pi) \approx 100MHz$) with a low frequency AFM cantilever (($\omega_0^{AFM}/(2\pi) \approx 100KHz$)). The AFM would be able to follow only displacement variations at frequencies lower than its operating one and not higher. For achieving this we have changed the external circuitry and adapted the device conform to the AFM operation. A schematic of the testbench is shown in figure 5.18.

Fig. 5.18: Experimental AFM setup used for detecting the resonance frequency of CNT resonators

There are two constraints to be respected : first the AFM has to detect displacement variations within its operation range and second the CNT has to be actuated around its resonance frequency. In order for the AFM to follow the displacement variations, the CNT vibration amplitude is modulated with a low frequency signal at $60kHz$, while the AFM is operated around $370kHz$. Through synchronous measurements techniques and by introducing a lock-in for the measurements the mechanical vibration and the topography can be measured simultaneously. For modulating the CNT vibration amplitude the RF signal $V^{ac}(\omega_{RF})$ actuating the nanotube is modulated with a signal at low frequency $V^{ac}(\omega_0^{AFM}) = 60kHz$. The low frequency modulation signal has been chosen to correspond to the modal vibration mode of

the AFM which is operated in its first harmonic $\omega_1^{AFM} = 6.23\omega_0^{AFM} \approx 370kHz$. The mechanical vibration of the nanotube has been matched with the modal frequency of the AFM cantilever ω_0^{AFM} in order to excite this mode. The lock-in has then been used to make a synchronous measurement of the AFM photodetector signal for the component at the frequency ω_0^{AFM}. The AFM operated in its first harmonic mode has then been used to measure the topography. Measurement results of resonance frequency and topography are shown in figure 5.19 and 5.20. The diameter and
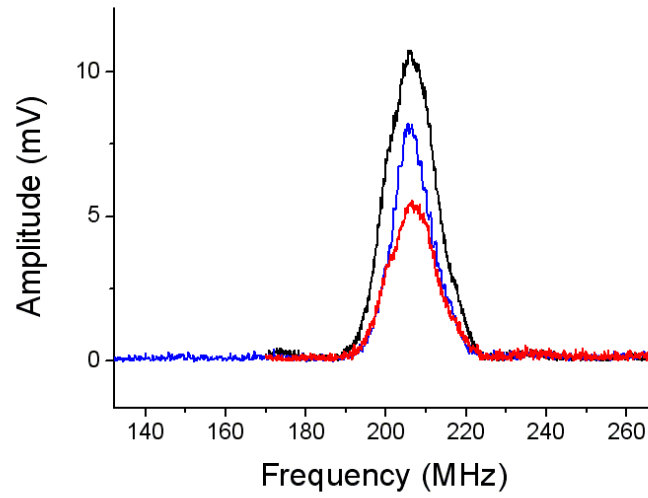
Fig. 5.19: Resonance curve of a doubly clamped CNT resonator, d=6nm, L=600nm, $\omega_0 = 206.2MHz$

the suspension length of the nanotube resonator were measured through the AFM resulting in $d = 6nm$ and $L = 600nm$. Fitting the resonance to a lorentzian curve we obtained a resonance frequency of $206.2MHz$ and a quality factor of $Q = 14$. According to the resonance frequency (equation (2.21),page 13) for a multiwalled nanotube and considering the density $2236kg/m^3$ we have extracted its Young's modulus equal to $E = 431 \pm 10GPa$. This value is coherent and confirms our results obtained with the DC deflection technique. High frequency experiments performed with the same source of MWNT-s resulted in a Young's modulus of $300GPa$[29].

(ß)   (b)
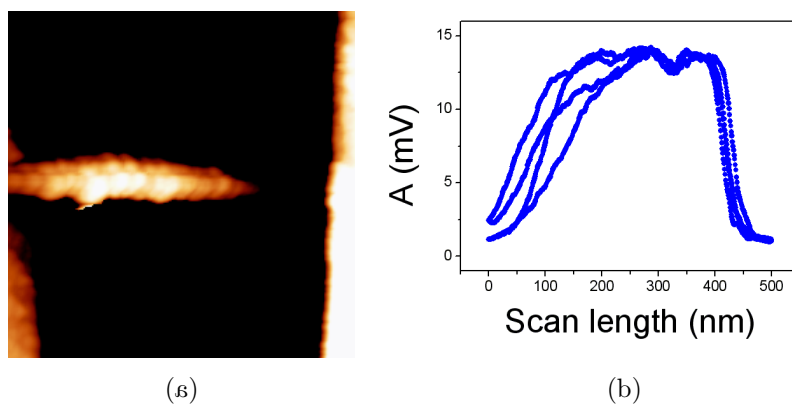
Fig. 5.20: a) Topology image of the fundamental mode of a vibrating doubly clamped CNT resonator. The actuation frequency is fixed at $\omega_0 = 206.2MHz$ and b) the electric signal measured with the lock-in corresponding to the mechanical profile of the fundamental mode of the nanotube

Chapitre 6

Conlusion

We analyzed and compared different actuation/detection techniques applied to nanowire based NEMS in order to choose the technique with the highest transduction gain and compatible with VLSI fabrication techniques. Our choice was the capacitive actuation combined with a balanced bridge piezoresistive detection technique. This technique resulted the most adapted to our nanowire-based NEMS as it offers the highest signal to background ratio and simultaneously compatible for portable applications.

We have successfully implemented a downmixing synchronous testbench for the actuation and detection of piezoresistive NEMS resonators. We have further validated with the implemented testbench the transduction principle based on piezoresistive p++ gauge transducers. The performance of the transduction principle in terms of : signal to background ratio, signal to noise ratio, ultimate mass resolution, ultimate displacement resolution, resonance frequency and quality factor have been evaluated. The measurement have shown remarkable results, the transduction gain obtained with this technique was $114nV/pm$ and the displacement resolution $120.2fm/\sqrt{Hz}$. We have proved that the detection technique employed in our experiments is highly efficient and able to resolve the thermomechanical motion of the nanoresonator. In spite of the downscaling and displacement reduction this is made possible thanks to the high transduction gain. The average resonance frequency measured per wafer is 19.16 MHz with a maximum dispersion of 2% showing the pretty good reproducibility of the VLSI process. The measured quality factors range from 2000-8000. The $SBR = 67$ obtained with this technique is the highest observed in present NEMS

resonators. We have an improvement on the SBR of more than two orders of magnitude respect to the state of the art resonant NEMS. The dynamic range resulted more than $100dB$ giving rise to a theoretical mass resolution of $0.3zg/\sqrt{Hz}$ (lower limit), however the mass resolution evaluated from the frequency fluctuations is higher. We have frequency fluctuations which are 2 orders of magnitude higher than what it is estimated from the dynamic range. This process is not yet understood and is under investigation. We have shown that with highly doped semiconducting piezoresistive gauges it is possible to obtain mass resolution similar or better than metallic gauges. For decreasing further the mass resolution the mass of the device has to be reduced. Very low mass resonators were obtained with CNT NEMS resonators. We have developped 3 fabrication processes for high frequency CNT NEMS. This techniques are not reproducible and have a low fabrication yield. However it allowed us to make a first study on the high frequency properties of these devices. A high frequency AFM displacement detection testbench was implemented for characterizing the mechanical vibrations of the CNT resonator. This method has enabled the detection of the resonance frequencies of CNT resonators but it is extremely complicated and has a destructive effect on the nanotubes. The Young's modulus extracted from the AC experiments agrees with the result obtained form the DC ones, which resulted to be $430 \pm 10GPa$. For CNT NEMS electronic motion detection it would be interseting to exploit their piezoresistive properties. SWNT were shown to posses a gauge factor up to 3000. It would be interesting to make electronic detection of CNT NEMS motion based on the piezoresistive effect.

Publication

In-plane nanoelectromechanical resonators based on silicon nanowire piezoresistive detection, E. Mile, G. Jourdan, I. Bargatin, S. Labarthe, C. Marcoux, P. Andreucci, S. Hentz, C. Kharrat, E. Colinet, L Duraffourg. Journal of Nanotechnology, Volume 21, 165504, Mars 2010

Sensitive in plane motion detection of nanoelectromechanical systems through semiconducting (p+) piezoresistive gauge transducers, Ervin Mile, Guillaume Jourdan, Carine Marcoux, Laurent Duraffourg, Philippe Andreucci, Robert Philippe. IEEE SENSORS 2009 Conference - 25-28 October 2009 - Christchurch NZ

Multiwall carbon nanotube high frequency resonator, Ervin Mile, Miguel Monteverde, M. G. Goffman, and J. P. Bourgoin. NT08, International Conference on the Science and Applications of Nanotubes, June 29th - July 4th Montpellier

CVD synthesis of single-walled carbon nanotubes from gold nanoparticle catalysts. Sreekar Bhaviripudi, Ervin Mile, Stephen A. Steiner, Aurea T. Zare, Mildred S.Dresselhaus, Angela M. Belcher, and Jing Kong. Journal of the American Chemical Society, 129(6) :15161517, 2007.

Design and characterization of carbon nanotube based NEMS, E. Mile, M. Monteverde, R. Lefèvre, V. Derycke, J. P. Bourgoin and M. F. Goffman International workshop on CNT RF NEMS and hybrid CMOS-CNT RF integrated circuits, 15th June 2007, EPFL

Bibliographie

[1] K. Jensen, K. Kim, and A. Zettl. An atomic-resolution nanomechanical mass sensor. *Nature Nanotechnology*, 3 :533 – 537, July 2008.

[2] U. Staufer, T. Akiyama, M.R. Gullo, A. Han, R. Imer, N.F. de Rooij, U. Aebi, M. Stolz N.F. Friederich A. Engel, P.L.T.M. Frederix, and D. Wirz. Micro- and nanosystems for biology and medicine. *Proceedings of the 32nd International Conference on Micro- and Nano-Engineering*, 84(5-8) :1681–1684, 2007.

[3] Mo Li, H. X. Tang, and M. L. Roukes1. Ultra-sensitive nems-based cantilevers for sensing, scanned probe and very high-frequency applications. *Nature Nanotechnology*, 2 :114–120, 2007.

[4] R. Pedrak, Tzv. Ivanov, K. Ivanova, T. Gotszalk, N. Abedinov, I. W. Rangelow, K. Edinger, E. Tomerov, T. Schenkel, and P. Hudek. Micromachined atomic force microscopy sensor with integrated piezoresistive sensor and thermal bimorph actuator for high-speed tapping-mode atomic force microscopy phase-imaging in higher eigenmodes. *Journal of Vacuum Science and Technology B : Microelectronics and Nanometer Structures*, 21(6) :3102–3107, 2003.

[5] T. Kouh, D. Karabacak, D. H. Kim, and K. L. Ekinci. Diffraction effects in optical interferometric displacement detection in nanoelectromechanical systems. *Applied Physics Letters*, 86(1) :013106, 2005.

[6] A. N. Cleland and M. L. Roukes. Fabrication of high frequency nanometer scale mechanical resonators from bulk si crystals. *Applied Physics Letters*, 69(18) :2653–2655, 1996.

[7] P.A. Truitt, J.B. Hertzberg, C.C. Huang, K.L. Ekinci, and K.C. Schwab. Efficient and sensitive capacitive readout of nanomechanical resonator arrays. *Nano Letters*, 7(1) :120–126, 2007.

[8] S. C. Masmanidis, R. B. Karabalin, I. De Vlaminck, G. Borghs, M. R. Freeman, and M. L. Roukes. Multifunctional Nanomechanical Systems via Tunably Coupled Piezoelectric Actuation. *Science*, 317(5839) :780–783, 2007.

[9] J.T.M. van Beek, P.G. Steeneken, B. Giesbers, and R. Philips. A 10mhz piezoresistive mems resonator with high q. *IEEE International Frequency Control Symposium and Exposition*, pages 475–480, 2006.

[10] L. Bilhaut. Actionnement magnétique l'échelle nanométrique. *Thèse de Doctorat de l'Université Joseph Fourier*, 2009.

[11] Y. T. Yang, C. Callegari, X. L. Feng, K. L. Ekinci, , and M. L. Roukes. Zeptogram-scale nanomechanical mass sensing. *Nano Letters*, 6(4) :583586, 2006.

[12] H.Y. Chiu, P. Hung, H. W. Ch. Postma, and M. Bockrath. Atomic-scale mass sensing using carbon nanotube resonators. *Nano Letters*, 8(12) :43424346, 2008.

[13] S. Timoshenko, D. Young, and J. W. Weaver. Vibration problems in engineering. *Wiley, New York*, 1974.

[14] A. H. Nayfeh and D. T. Mook. Nonlinear oscillations. *John Wiley, New York*, 1979.

[15] E. Volterra and E. C. Zachmanoglou. Dynamics of vibrations. *Charles E. MERRILL BOOKS*, 1965.

[16] N. Kacem. Nonlinear dynamics of m&nems resonant sensors : design strategies for performance enhancement. *PhD Thesis, Insa Lyon*, 2010.

[17] V. Sazonova, Y. Yaish, H. Ustunel, D. Roundy, T. A. Arias, and P. L. McEuen. A tunable carbon nanotube electromechanical oscillator. *Nature*, 431(15) :284–287, 2004.

[18] K. Jensen, C. Girit, W. Mickelson, and A. Zettl. Tunable nanoresonators constructed from telescoping nanotubes. *Physical Review Letters*, 96(21) :215503, 2006.

[19] E. Mile, G. Jourdan, C. Marcoux, L. Duraffourg, P. Andreucci, and P. Robert. Sensitive in plane motion detection of nanoelectromechanical systems through semiconducting (p+) piezoresistive gauge transducers. *IEEE SENSORS Conference, 25-28 October, Christchurch NZ*, 2009.

[20] E. Colinet, L. Duraffourg, S. Labarthe, S. Hentz, P. Robert, and P. Andreucci. Self-oscillation conditions of a resonant nanoelectromechanical mass sensor. *Journal of Applied Physics*, 105(12) :124908, 2009.

[21] K.L. Ekinci. Electromechanical transducers at the nanoscale : Actuation and sensing of motion in nanoelectromechanical systems (nems). *Small*, 1(8-9) :786–797, 2005.

[22] S. S. Verbridge, L. M. Bellan, J. M. Parpia, and H. G. Craighead. Optically driven resonance of nanoscale flexural oscillators in liquid. *Nano Letters*, 6(9) :2109–214, 2007.

[23] J. S. Bunch, A. M. van der Zande, S. S. Verbridge, I. W. Frank, D. M. Tanenbaum, J. M. Parpia, H. G. Craighead, and P. L. McEuen. Electromechanical Resonators from Graphene Sheets. *Science*, 315(5811) :490–493, 2007.

[24] H. Huang, X. Ming, C. A. Zorman, M. Mehregany, and M. L. Roukes. Nanoelectromechanical systems : Nanodevice motion at microwave frequencies. *Nature*, 421 :496, January 2003.

[25] H. B. Peng, C. W. Chang, S. Aloni, T. D. Yuzvinsky, and A. Zettl. Microwave electromechanical resonator consisting of clamped carbon nanotubes in an abacus arrangement. *Physical Review B (Condensed Matter and Materials Physics)*, 76(3) :035405, 2007.

[26] B. Witkamp, M. Poot, and H.S.J. van der Zant. Bending-mode vibration of a suspended nanotube resonator. *Nano Letters*, 6(12) :2904–2908, 2006.

[27] I. Bargatin, I. Kozinsky, and M. L. Roukes. Efficient electrothermal actuation of multiple modes of high-frequency nanoelectromechanical resonators. *Applied Physics Letters*, 90(9) :093116, 2007.

[28] L. Jiang, R. Cheung, J. Hedley, M. Hassan, A.J. Harris, J.S. Burdess, M. Mehregany, and C.A. Zorman. Sic cantilever resonators with electrothermal actuation. *Sensors and Actuators A : Physical*, 128(2) :376–386, 2006.

[29] D. Garcia-Sanchez, A. San Paulo, M. J. Esplandiu, F. Perez-Murano, L. Forro, A. Aguasca, and A. Bachtold. Mechanical detection of carbon nanotube resonator vibrations. *Physical Review Letters*, 99(8) :085501, 2007.

[30] L. Sekaric, J. M. Parpia, H. G. Craighead, T. Feygelson, B. H. Houston, and J. E. Butler. Nanomechanical resonant structures in nanocrystalline diamond. *Applied Physics Letters*, 81(23) :4555–4457, 2002.

[31] B. Ketterer, B. Bitnar, B. Haas, T. Neiger, D. Bachle, F. Glaus, and J. Gobrecht. Electromechanical microswitches with thermal actuation. *Proceedings of the International Microprocesses and Nanotechnology Conference*, pages 206–207, 2002.

[32] A. Jain, A. Kopa, P. Yingtian, G.K. Fedder, and X. Huikai. A two-axis electrothermal micromirror for endoscopic optical coherence tomography. *IEEE Journal, Selected Topics in Quantum Electronics*, pages 636–642, 2004.

[33] S.K. Bordatchev, E.V. Nikumb. Microgripper : Design, finite element analysis and laser microfabrication. *Proceedings of the International Conference on MEMS, NANO and Smart Systems*, pages 308–313, 2003.

[34] H.C. Lee, J.H. Park, J.Y. Park, H.J. Nam, and J.K Bu. Design, fabrication and rf performances of two different types of piezoelectrically actuated ohmic mems switches. *J. Micromech. Microeng.*, 15 :20982104, 2005.

[35] R. Mahameed, N. Sinha, M. B Pisani, and G. Piazza. Dual-beam actuation of piezoelectric aln rf mems switches monolithically integrated with aln contourmode resonators. *J. Micromech. Microeng.*, 18 :105011105022, 2008.

[36] F. Xu, S. Trolier-McKinstry, W. Ren, B. Xu, Z.-L. Xie, and K. J. Hemker. Domain wall motion and its contribution to the dielectric and piezoelectric properties of lead zirconate titanate films. *Journal of Applied Physics*, 89(2) :1336–1348, 2001.

[37] K. Saito, T. Kurosawa, T. Akai, T. Oikawa, and H. Funakubo. Structural characterization and 90[degree] domain contribution to ferroelectricity of epitaxial pb(zr[sub 0.35],ti[sub 0.65])o[sub 3] thin films. *Journal of Applied Physics*, 93(1) :545–550, 2003.

[38] X.H. Du, J. Zheng, U. Belegundu, and K. Uchino. Crystal orientation dependence of piezoelectric properties of lead zirconate titanate near the morphotropic phase boundary. *Applied Physics Letters*, 72(19) :2421–2423, 1998.

[39] Crawley E F and Luis J. Use of piezoelectric actuators as elements of intelligent structures. *The American Institute of Aeronautics and Astronautics*, 25(10) :1373–1385, 1987.

[40] Y. Ito, K. Kushida, K. Sugawara, and H. Takeuchi. A 100-mhz ultrasonic transducer array using zno thin films. *IEEE TUFFC*, 42 :316, 1995.

[41] C. Zuo, J. Van der Spiegel, and G. Piazza. 1.05-ghz cmos oscillator based on lateral-field-excited piezoelectric aln contour-mode mems resonators. *IEEE IEEE Transactions on Ultrasonics, Ferroelectrics, and Frequency Control*, 57(1) :82–87, 2010.

[42] R. B. Karabalin, M. H. Matheny, X. L. Feng, E. Defaÿ, G. Le Rhun, C. Marcoux, S. Hentz, P. Andreucci, and M. L. Roukes. Piezoelectric nanoelectromechanical resonators based on aluminum nitride thin films. *Applied Physics Letters*, 95(10) :103111, 2009.

[43] N. Sinha, G. E. Wabiszewski, R. Mahameed, V. V. Felmetsger, Sh. M. Tanner, R. W. Carpick, and G. Piazza. Piezoelectric aluminum nitride nanoelectromechanical actuators. *Applied Physics Letters*, 95(5) :053106, 2009.

[44] Cleland A.N. External control of dissipation in a nanometer-scale radiofrequency mechanical resonator. *Sensors and Actuators A : Physical*, 72 :256–261(6), February 1999.

[45] I. Bargatin, E. B. Myers, J. Arlett, B. Gudlewski, and M. L. Roukes. Sensitive detection of nanomechanical motion using piezoresistive signal downmixing. *Applied Physics Letters*, 86(13) :133109, 2005.

[46] R.R. He, X.L. Feng, M.L. Roukes, and P.D. Yang. Self-transducing silicon nanowire electromechanical systems at room temperature. *Nano Letters*, 8 :1756–1761, 2008.

[47] X.L. Feng, R.R. He, P.D. Yang, and M.L. Roukes. Very high frequency silicon nanowire electromechanical resonators. *Nano Letters*, 7 :1953–1959, 2007.

[48] K. L. Ekinci, Y. T. Yang, X. M. H. Huang, and M. L. Roukes. Balanced electronic detection of displacement in nanoelectromechanical systems. *Applied Physics Letters*, 81(12) :2253–2255, 2002.

[49] X. M. H. Huang, X. L. Feng, C. A. Zorman, M. Mehregany, and M. L. Roukes. Vhf, uhf and microwave frequency nanomechanical resonators. *New Journal of Physics*, 7 :247, 2005.

[50] F. N. Hooge. 1/[latin small letter f with hook] noise is no surface effect. *Physics Letters A*, 29(3) :139 – 140, 1969.

[51] H. W. Ch. Postma, I. Kozinsky, A. Husain, and M. L. Roukes. Dynamic range of nanotube- and nanowire-based electromechanical systems. *Applied Physics Letters*, 86 :223105, 2005.

[52] Alistair C. H. Rowe. Silicon nanowires feel the pinch. *Nature Nanotechnology*, 3 :311 – 312, 2008.

[53] C. V. Heer. Statistical mechanics, kinetic theory, and stochastic processes. *New York, Academic Press*, 1972.

[54] Robins W. P. Phase noise in signal sources. *London, Peter Peregrinus, Ltd.*, 1982.

[55] N. Kacem, B. Reig S. Hentz, D. Pinto, and V. Nguyen. Nonlinear dynamics of nanomechanical beam resonators : improving the performance of nems-based sensors. *Nanotechnology*, 20(27) :275501, 2009.

[56] N. Kacem, J. Arcamone, F. Perez-Murano, and S. Hentz. Dynamic range enhancement of nonlinear nanomechanical resonant cantilevers for highly sensitive nems gas/mass sensor applications. *Journal of Micromechanics and Microengineering*, 20 :045023, 2010.

[57] B. Lassagne, D. Garcia-Sanchez, A. Aguasca, and A. Bachtold. Ultrasensitive mass sensing with a nanotube electromechanical resonator. *Nano Letters*, 8(11) :37353738, 2008.

[58] S. Bhaviripudi, E. Mile, S. A. Steiner, A. T. Zare, M. S. Dresselhaus, A. M. Belcher, and J. Kong. Cvd synthesis of single-walled carbon nanotubes from gold nanoparticle catalysts. *Journal of the American Chemical Society*, 129(6) :1516–1517, 2007.

[59] E. Mile, G. Jourdan, I. Bargatin, S. Labarthe, C. Marcoux, P. Andreucci, S. Hentz, C. Kharrat, E. Colinet, and L. Duraffourg. In-plane nanoelectromechanical resonators based on silicon nanowire piezoresistive detection. *Nanotechnology*, 21 :165504, 2010.

[60] J. Arcamone, M. A. F. van den Boogaart, F. Serra-Graells, J. Fraxedas, J. Brugger, and F. Perez-Murano. Full-wafer fabrication by nanostencil lithography of micro/nanomechanical mass sensors monolithically integrated with cmos. *Nanotechnology*, 19(30) :305302, 2008.

[61] A. K. Huttel, G. A. Steele, B. Witkamp, M. Poot, L. P. Kouwenhoven, and H. S. J. van der Zant. Carbon nanotubes as ultrahigh quality factor mechanical resonators. *Nano Letters*, 9(7) :2547–2552, 2009.

[62] X. L. Feng, C. J. White, A. Hajimiri, and M. L. Roukes. A self-sustaining ultrahigh-frequency nanoelectromechanical oscillator. *Nature Nanotechnology*, 3 :342–346, May 2008.

[63] J. A. Harley and T. W. Kenny. High-sensitivity piezoresistive cantilevers under 1000 thick. *Applied Physics Letters*, 75 :289, 1999.

[64] A. N. Cleland and M. L. Roukes. Noise processes in nanomechanical resonators. *Journal of Applied Physics*, 92(5) :2758, 2002.

[65] J. L. Arlett, J. R. Maloney, B. Gudlewski, M. Muluneh, and M. L. Roukes. Self-sensing micro- and nanocantilevers with attonewton-scale force resolution. *Nano Letters*, 6(5) :1000–1006, 2006.

[66] O. N. Tufte and E. L. Stelzer. Piezoresistive properties of silicon diffused layers. *J. Appl. Phys.*, 34 :313, 1963.

[67] K. L. Ekinci, Y. T. Yang, and M. L. Roukes. Ultimate limits to inertial mass sensing based upon nanoelectromechanical systems. *Journal of Applied Physics*, 95 :2682, 2004.

[68] J. Verd, A. Uranga, G. Abadal, J.L. Teva, F. Torres, J. Lopez, F. Perez-Murano, J. Esteve, and N. Barniol. Monolithic cmos mems oscillator circuit for sensing in the attogram range. *Electron Device Letters, IEEE*, 29 :146–148, 2008.

[69] Franz J. Giessibl. Advances in atomic force microscopy. *Rev. Mod. Phys.*, 75(3) :949–983, Jul 2003.

[70] R. Saito, M. Fujita, G. Dresselhaus, and M. S Dresselhaus. Electronic structure of chiral graphene tubules. *Applied Physics Letters*, 60 :2204–2207, 1992.

[71] R. Saito, M. Fujita, G. Dresselhaus, and M. S. Dresselhaus. Electronic structure of graphene tubules based on *c*60. *Phys. Rev. B*, 46(3) :1804–1811, July 1992.

[72] M. M. J. Treacy, T. W. Ebbesen, and J. M. Gibson. Exceptionally high young's modulus observed for individual carbon nanotubes. *Nature*, 381 :678–680, June 1996.

[73] A. Krishnan, E. Dujardin, T. W. Ebbesen, P. N. Yianilos, and M. M. J. Treacy. Young's modulus of single-walled nanotubes. *Phys. Rev. B*, 58(20) :14013–14019, Nov 1998.

[74] P. Poncharal, Z. L. Wang, D. Ugarte, and W. A. de Heer. Electrostatic Deflections and Electromechanical Resonances of Carbon Nanotubes. *Science*, 283(5407) :1513–1516, 1999.

[75] B. Babic, J. Furer, S. Sahoo, Sh. Farhangfar, and C. Schnenberger*. Intrinsic thermal vibrations of suspended doubly clamped single-wall carbon nanotubes. *Nano Letters*, 3(11) :15771580, 2003.

[76] S. T. Purcell, P. Vincent, C. Journet, and Vu Thien Binh. Tuning of nanotube mechanical resonances by electric field pulling. *Phys. Rev. Lett.*, 89(27) :276103, Dec 2002.

[77] M. Nishio, Sh. Sawaya, S. Akita, and Y. Nakayama. Carbon nanotube oscillators toward zeptogram detection. *Applied Physics Letters*, 86(13) :133111, 2005.

[78] A. K. Httel, G. A. Steele, B. Witkamp, M. Poot, L. P. Kouwenhoven, and H. S. J. van der Zant. Carbon nanotubes as ultrahigh quality factor mechanical resonators. *Nano Letters*, 9(7) :25472552, 2009.

[79] J.M Bonard, T. Stora, J.P. Salvetat, F. Maier, T. Stckli, C. Duschl, L. Forr, W. A. de Heer, and A. Chtelain. Purification and size-selection of carbon nanotubes. *Advanced Materials*, 9 :827–831, 1997.

[80] A. Jungen, L. Durrer, Ch. Stampfer, C. Roman, and Ch. Hierold. Progress in carbon nanotube based nanoelectromechanical systems synthesis. *physica status solidi (b)*, 244 :4323–4326, November 2007.

[81] Ch. Hierold, A. Jungen, Ch. Stampfer, and Th. Helbling. Nano electromechanical sensors based on carbon nanotubes. *Sensors and Actuators A : Physical*, 136(1) :51 – 61, 2007. 25th Anniversary of Sensors and Actuators A : Physical.

[82] E. Dujardin, V. Derycke, M. F. Goffman, R. Lefèvre, and J. P. Bourgoin. Self-assembled switches based on electroactuated multiwalled nanotubes. *Applied Physics Letters*, 87 :193107, 2005.

[83] E. Valentin, S. Auvray, J. Goethals, J. Lewenstein, L. Capes, A. Filoramo, A. Ribayrol, R. Tsui, J.P. Bourgoin, and J.N. Patillon. High-density selective placement methods for carbon nanotubes. *Microelectronic Engineering*, 61-62 :491–496, July 2002.

[84] Peter J. Burke. Ac performance of nanoelectronics : towards a ballistic thz nanotube transistor. *Solid-State Electronics*, 48 :1981–1986, march 2004.

[85] Peter J. Burke. An rf circuit model for carbon nanotubes. *IEEE Transactions on Nanotechnology*, 2(1) :1981–1986, march 2003.

[86] Peter J. Burke. Luttinger liquid theory as a model of the gigahertz electrical properties of carbon nanotubes. *IEEE Transactions on Nanotechnology*, 1(3) :129–144, September 2002.

[87] R. Dianoux. Injection et detection de charges dans des nanostructures semiconductrices par microscopie force atomique. *Thèse de Doctorat de l'Université Joseph Fourier*, 2004.